Quantitative Fluorescence Studies in Living Cells: Extending Fluorescence Fluctuation Spectroscopy to Peripheral Membrane Proteins

A DISSERTATION
SUBMITTED TO THE FACULTY OF THE GRADUATE SCHOOL
OF THE UNIVERSITY OF MINNESOTA
BY

Elizabeth Myhra Smith

IN PARTIAL FULFILLMENT OF THE REQUIREMENTS
FOR THE DEGREE OF
DOCTOR OF PHILOSOPHY

Joachim D. Mueller, Advisor

May 2015

Acknowledgements

My path through graduate school has had many turns, roundabouts, repeats, and times when I was completely lost. During this journey, I have been blessed with a collection of people who have contributed laughter and smiles at the best times and who have help me through the worst times with their love, support, and guidance.

My labmates have been a great resource for scientific knowledge, discussion, and advice. Specifically, I'm thankful for Patrick Macdonald, Jolene Johnson, and Keir Fogarty, my closest peers. I only truly appreciated their collective awesomeness, amazing support, and friendship after they moved on (*almost all at once*). Patrick, Jolene, and Keir challenged me to think critically about scientific problems, let me vent about work and life stresses, and offered creative and humorous solutions to paper writing issues. Their friendship made me a better, saner scientist.

I was lucky to have not just one but two excellent scientific mentors during my time at the University of Minnesota, my advisor Dr. Jochen Mueller and FFS extraordinaire Dr. Yan Chen. After a summer introduction to FFS, I was drawn back to the lab for graduate school because of the energy and dedication that Jochen and Yan bring to their research. From Jochen, I learned the fundamentals of scientific inquiry, including: thoughtful and thorough experimentation, detailed theoretical development, and the importance of proper calibration measurements. From Yan, I learned instrumentation and biology, where it was okay to be a little less precise, and how to look at a project from many different angles. Through their mentorship, guidance, and training I've built a strong scientific foundation that will allow me to successfully tackle whatever challenges come next.

Some of my fondest memories from graduate school are from my first year when I saw my classmates and friends on a daily basis, for many hours at a time. I still smile at the thought of our impressive showing of top-of-the-head "rally" ponytails at 1 AM (final

hours of a problem set) in a room (Tate 216) filled with only 10% women. In particular, my classmates Joe Kinney and Kate Raach have become close friends. Joe's kindness, positivity, and hugs will almost always brightness my day, and his willingness to tutor me before the GWE helped me assuredly clear that hurdle on my path towards a Ph.D. Kate, what can I say, we entered as the two American females in our class and were almost immediately told that statistically one of us wouldn't finish our Ph.D. I'm so glad we stuck it out together, growing as physicists and friends during this seemingly endless exercise in warrior training. Furthermore, in this world of female physicist small number statistics, I am grateful to have not just had another female in my class who 'stuck it out' but one who I can call a best friend.

I have found a plethora of support outside of physics as well. My parents, Faye and Warren Smith, have been MVPs in my Ph.D. journey. They provided me with the foundation and support necessary to pursue my scientific dreams. While my parents were not trained as scientists, they both have creative and technical minds, specifically when it comes to repairs and projects around the home. Thus, I was raised in an environment that developed and rewarded creative problem solving. They also fostered my interest in science from an early age, which included: sending me to Space Camp (twice!) and encouraging me to present my astatically pleasing "space station" at a local science conference even though they knew it was completely unrealistic. Over the last couple of years, I have needed their support more than ever. They have become my emotional rocks and my financial saviors. I am truly blessed to have these two amazing people in my life. My journey towards finishing this degree would have been almost impossible without them.

Last but not least, my support team has included amazing friends: Sarah, Gavin, Melissa, Rebecca, Michelle, Carla, Chrissy, Amanda, Rachel, Zach, Molly and a collection of others who have floated in and out of my life. While they are scattered across the country, I know that they are never more than a phone call away and through a conversation can provide much needed sanity and support. Additionally, I appreciate that Zach and Jolene

went beyond normal friendship bounds by providing me with cooked food and shelter when I needed their help the most. And finally Nick Vandehey, my companion in my early scientific days at Wisconsin, supported my endeavors and encouraged me to be a "science cowboy" by taking risks in experimentation and problem solving. He helped me become a better scientist by showing me that while planning is important, at some point you just have to jump in and have the confidence that you will be able to fix whatever problems may arise.

Many thanks to you all, I couldn't have done it without you.

This work was supported by grants from the National Institutes of Health (R01 GM064589 and GM098550) and the National Science Foundation (PHY-0346782). Additional support was provided by the National Institute of Allergy and Infection Diseases of the NIH, grant No. 5T32A1083196 (Minnesota Training Program in Virology) and the University of Minnesota Graduate School Doctoral Dissertation Fellowship.

Dedication

This work is dedicated to my parents, Faye and Warren Smith. I'm so grateful for your support and that I can share the joy of completion with you.

And also to my Grandfather Lester Smith, you seemed to understand and respect my Ph.D. journey more than anyone else; I wish you could see this.

Abstract

The interactions of peripheral membrane proteins with both membrane lipids and proteins are vital for many cellular processes including membrane trafficking, cellular signaling, and cell growth/regulation. Building accurate biophysical models of these processes requires quantitative characterization of the behavior of peripheral membrane proteins, yet methods to quantify their interactions inside living cells are very limited. Because peripheral membrane proteins usually exist both in membrane-bound and cytoplasmic forms, the separation of these two populations is a key challenge. This thesis aims at addressing this challenge by extending fluorescence fluctuation spectroscopy (FFS) to simultaneously measure the oligomeric state of peripheral membrane proteins in the cytoplasm and at the plasma membrane. We developed a new method based on z-scan FFS that accounts for the fluorescence contributions from cytoplasmic and membrane layers by incorporating a fluorescence intensity z-scan through the cell. H-Ras-EGFP served as a model system to demonstrate the feasibility of the technique. The resolvability and stability of z-scanning was determined as well as the oligomeric state of H-Ras-EGFP at the plasma membrane and in the cytoplasm. Further, we successfully characterized the binding affinity of a variety of proteins to the plasma membrane by quantitative analysis of the z-scan fluorescence intensity profile. This analysis method, which we refer to as z-scan fluorescence profile deconvoution, was further used in combination with dual-color competition studies to determine the lipid specificity of protein binding. Finally, we applied z-scan FFS to provide insight into the early assembly steps of the HTLV-1 retrovirus.

Table of Contents

List of Tables

List of Figures

List of Abbreviations

3DG	three-dimensional Gaussian
ACF	autocorrelation function
APD	avalanche photodiode
BM	bottom membrane
cps	counts per second
DAG	diacylglycerol
EGFP	enhanced green fluorescence protein
$EGFP_2$	dimeric EGFP
Endo	Endophilin A2
ER	endoplasmic reticulum
EYFP	enhanced yellow fluorescence protein
FCA	fluorescence cumulant analysis
FCS	fluorescence correlation spectroscopy
FFS	fluorescence fluctuation spectroscopy
FPD	fluorescence profile deconvolution
FRET	fluorescence resonance energy transfer
GPCR	G-protein coupled receptor
GL	Gaussian-Lorentzian
HIV-1	human immunodeficiency virus type 1
HTLV-1	Human T-cell lymphotropic virus Type 1
IP_3	inositol triphosphate
LUV	large unilamellar vesicles
MA	matrix domain of Gag protein
mCh	mCherry fluorescence protein
mGL	modified Gaussian-Lorentzian
Myo1C	myosin-1C
NE	nuclear envelope

NMR	nuclear magnetic resonance
OPE	one-photon excitation
PBS	phosphate-buffered saline
PCH	photon counting histogram
pdf	probability distribution function
pDNA	plasmid DNA
PH	pleckstrin homology domain
$PI(4,5)P_2$	phosphatidylinositol 4,5-bisphosphate
PLCδ	phospholipase C, delta 1
PS	phosphatidylserine
PSF	point spread function
RARLBD	ligand binding domain of retinoic acid receptor
RIPSF	radially integrated PSF
RXRLBD	ligand binding domain of retinoid x receptor
SA/V	surface area to volume
SNR	signal-to-noise ratio
SPR	Surface plasmon resonance
SS	20 amino acid ER signal sequence
TA	torsin-1A
TA-ΔNTD	TA mutant (n-terminus binding domain deletion)
TIFCA	time-integrated fluorescence cumulant analysis
TIRF	total internal reflection fluorescence
TM	top membrane
TPE	two-photon excitation

1. Introduction

Proteins are fundamental biomolecules of cellular systems. They provide the cell with structure and are central to the execution of every process vital for cell function. More specifically, the association of proteins into complexes is a critical aspect of cell biology and essential for the execution of specific tasks. Since the cell is divided into different compartments, protein complexes are found within each compartment and at the interface between compartments. The plasma membrane is a unique interface that provides a barrier between the intracellular cytosol and extracellular fluid. It consists of a lipid bilayer that incorporates a vast array of membrane proteins. Exchange of cellular signals or materials between the cell and its environment often rely on the actions of protein complexes to pass through the membrane interface.

In cellular signaling, the plasma membrane provides a platform for the initiation of signal cascades. It functions as a signaling switchboard with membrane proteins playing the role of traditional telephone operators. Membrane proteins receive information from the extracellular space and relay that information to the cell through intracellular signal cascades that ultimately modulate cellular function. Additionally, the plasma membrane is important for many vesicle trafficking pathways and plays a role in cell motility though interactions with cytoskeletal proteins. Finally, the plasma membrane is of particular interest for study, because it is the primary gateway for viral infection and is often the site of viral particle assembly.

The quantification of protein-protein interactions directly inside the living cell is a crucial prerequisite to build quantitative models of cellular processes. Fluorescence

fluctuation spectroscopy (FFS) is a method that can be used to study such protein-protein interactions. Our lab and others have used FFS to characterize the interactions of soluble proteins in the nucleus and the cytoplasm of living mammalian cells (1–3). While applications of FFS to membrane systems have been reported (4–7), there has been no quantitative study critically analyzing the influence of the plasma membrane / cytoplasm interface on FFS analysis of protein interactions. In this thesis we investigate this situation and demonstrate that the overlap of the excitation light with the membrane and the cytoplasm introduces confounding effects that are not captured by traditional FFS analysis. Based on this analysis, we developed a new FFS model that accounts for cytoplasmic and membrane contributions to the fluorescence signal by performing an axial scan of the laser excitation beam through the cell. After developing and testing the method we apply it to quantify the oligomeric state of proteins at the plasma membrane and in the cytoplasm.

1.1 Membrane proteins

Membrane proteins can be broken up in to two distinct groups: integral membrane proteins and peripheral membrane proteins.

1.1.1 Integral membrane proteins

Integral membrane proteins are permanent residents of the plasma membrane and often completely span the lipid bilayer either in one single pass or in a series of loops that double back and forth through the bilayer. They have an amphiphilic structure; with

hydrophilic regions that extend into the cytoplasm or the extracellular fluid and hydrophobic regions that pass through the membrane. The function of integral membrane proteins is varied and includes cell adhesion, energy transduction, and the regulation of movement of molecules across the membrane.

1.1.2 Peripheral membrane proteins

Peripheral membrane proteins, the group of proteins primarily studied within this thesis, interact transiently with the plasma membrane and are free to diffuse along the plasma membrane as well as between the membrane and the cytosol. They are primarily hydrophilic proteins but associate with membrane lipids through one or more of the following mechanisms: electrostatic interactions, a covalently attached lipid anchor, a cluster of hydrophobic residues, a modular domain that targets specific membrane phosphoinositides, or a region that interacts non-covalently with membrane proteins (8–10).

Peripheral membrane proteins play a role in signal transduction, membrane trafficking, cytoskeleton-membrane linking, and phospholipid metabolism and catabolism, to name just a few of their many functions (8–10). Such proteins are often recruited to the plasma membrane during cellular processes like cell signaling and membrane trafficking (8). In the case of Ras, a signal transduction peripheral protein, the activation of a receptor at the membrane promotes the post-translational modification (palmitoylation) of Ras and the subsequent translocation of the protein to the membrane (11, 12). For other peripheral membrane proteins, the interaction with the membrane

induces conformation changes in the protein which are necessary for its function (8). The converse is also true, in that changes within the lipid bilayer are often induced by the attachment of a peripheral membrane protein to the membrane. For example, heterotrimeric G-proteins modulate their immediate lipid environment by inducing remodeling of the plasma membrane which can in turn modulate the binding affinity of G-proteins to the membrane (13, 14). Overall, since membrane binding is the mechanism that defines the structure and function of peripheral membrane proteins (as well as the subsequent lipid environment), determining the binding affinity, lipid specificity, and oligomeric state of the protein is a crucial step for developing a biophysical model of its function.

1.1.3 Cellular signaling – G protein coupled receptors

The development of assays and techniques to study peripheral membrane proteins goes beyond the understanding of biological function and extends into deconstruction of disease pathways and development of pharmaceutical treatments. Because of their cellular location and role in signaling, cell-surface receptors are often targets of pharmaceutical agents. The largest family of cell-surface signaling receptors,, G-protein coupled receptors (GPCRs), are the target of ~30% of prescribed drugs on the market (15–18). Fundamental cellular and therapeutic processes start with the binding of a ligand or drug to the GPCR which causes a conformational change of the receptor. This change activates one or more peripheral G-proteins, which initiate signal transduction by interacting with other membrane proteins or by dissociating from the membrane in order

to communicate with nuclear or cytoplasmic targets (13, 14, 16, 19). For the nuclear targets, common G-protein modulated pathways include cell proliferation, differentiation, and development (16, 20). Thus, it should not be a surprise that the overstimulation of specific GPCR pathways often results in tumor growth and cancer (20). For the understanding and development of future GPCR (and other cell surface receptor) drug targets it is important not only to study the binding of ligands and drugs to the receptor but to have a technique that can probe the binding and interactions of G-proteins and their downstream targets within a live cell environment. More recent studies have suggested that the signaling from GPCRs often include G-protein independent pathways (16, 19). This more complex picture of the intricate signaling network further suggests the need for the development and application of live-cell techniques that can probe protein interactions both in the cytoplasm and at the membrane.

1.2 Traditional methods used for studying membrane proteins

The characterization of membrane proteins is challenging because the interplay between the protein and the lipid bilayer is essential for both conformation and function. To deal with this issue, many structural and functional studies rely on in-vitro assays performed on either isolated membranes or model membrane systems. While the plasma membrane is made up mainly of proteins and phospholipids, model membranes have a simplified composition; consisting of one or two types of the phospholipids found at the plasma membrane (21–23). The most common forms of model membranes found in studies are micelles, unilamellar vesicles, multilamellar vesicles, and supported lipid

bilayers (21–23). The advantage of model membranes is their simple composition as this allows for an easily controllable platform for studying lipid-protein interactions. This, however, is also their disadvantage; they do not accurately represent the actual native membrane. Isolated membranes can be used to partially address this issue. Because isolated membranes have been extracted from an actual cell, they offer a more realistic membrane environment for the study of protein-lipid interactions (21–23). However, model membranes are largely preferred by researchers, because isolated membranes are hard to prepare and the integral membrane proteins within the isolated membrane increase the complexity, thereby making the interpretation of experimental results less straightforward. For these reasons, the majority of our knowledge of the affinity and specificity of protein-lipid binding comes from studies using model membrane systems (21, 22).

1.2.1 Structural assays

Structural studies of a protein are helpful in providing clues to binding partners, interactions, conformational changes, and cellular function. X-ray crystallography and nuclear magnetic resonance (NMR) structural studies are two common techniques used to determine protein structure which can shed light on the protein's function. For membrane proteins, these methods take on an extra level of complexity because the protein is often characterized in a micelle solution after first being separated from the native membrane through the use of amphiphilic detergents (24). While this approach yields structural information, it also poses an inherent challenge. The micelle may perturb the protein's

native structure, because the lipids within the micelle have a much higher curvature than typically found at the plasma membrane (24). In general, structural studies need to be supplemented with assays that characterize functional interactions of the protein. This is especially relevant for membrane proteins because of the important role protein-lipid interactions play in protein conformation and function. A brief discussion of some standard functional assays used to probe both protein-lipid and protein-protein interactions at the plasma membrane is given below.

1.2.2 Fractionation assay

Protein-lipid interaction assays can be broken up into biochemical- and optical-based approaches. On the biochemical side, cellular fractionation is arguably the most standard method for determining the relative interaction strength of protein binding to the membrane. Fractionation assays separate and quantify membrane-bound and cytoplasmic components through either sedimentation (high-speed centrifugation) or flotation (density gradient centrifugation) (21, 22). These assays are can be performed on a homogenized cell suspension. However, quantitative fractionation of protein/membrane binding requires model membrane vesicles because the vesicles can be made to a specific size and lack internal membranes. In these studies, large unilamellar vesicles (LUV) of a well-defined size are incubated with varying concentrations of a peripheral membrane protein. Through either sedimentation or flotation, the lipids are separated from the solution into either pellets or a layer. The relative amount of protein in the supernatant versus the pellet is used to determine the binding affinity of the protein (21, 22). The advantage of this

approach is that LUVs are quite easy to produce, the equipment and protocols are well established and there is no need for a label. On the other hand, it is hard to quantify a fractionation assay from a sample of living cell, fractionation is not a time-resolved technique, the measured quantity represents the average from a population of cells, and the sample is destroyed during centrifugation.

1.2.3 Fluorescence-based assays

There is an array of fluorescence techniques for studying protein-lipid interactions. These methods typically use a fluorescent molecule or protein to optically tag the protein of interest. However, intrinsic fluorescent properties of the protein can be exploited as well. A relatively straightforward assay of membrane binding quantifies changes in the intrinsic fluorescence from tryptophan residues. The emission of tryptophan is extremely sensitive to changes in its immediate environment. A tryptophan residue in contact with a hydrophobic environment shifts emission to shorter wavelengths coupled with an increase in fluorescence (21, 22, 25). Thus if a peripheral membrane protein has a tryptophan residue exposed close to the membrane binding region of the protein, the change in fluorescence can be used to characterize the strength of binding to model membranes (21, 22, 25). A variation of this technique adds a fluorescently labeled lipid to the model membrane. Instead of measuring the shift in tryptophan fluorescence the efficiency of fluorescence resonance energy transfer (FRET) between the tryptophan (donor) and the fluorescent lipid (acceptor) is measured (21, 22). FRET is extremely sensitive to distance between the acceptor and donor molecule. Proximity of both

molecules within a few nanometers leads to efficient FRET, while a slightly larger distance abolishes the FRET signal (26). The technique has been used to determine binding affinity as well as binding geometry (21, 22). FRET has an advantage over measuring shifts in tryptophan fluorescence. The tryptophan FRET donor only needs to be in the vicinity (~ a few nm) of the lipid acceptor to produce a signal as opposed to the molecular contact required to observe the shift in tryptophan emission. In addition, a tryptophan or a fluorescent probe can be attached to the protein of interest, if there isn't a tryptophan initially present.

Fluorescence imaging has been applied to study protein-lipid interactions and protein-protein interactions at the plasma membrane. A z-stack of fluorescence confocal images provides information about the spatial distribution of fluorescently labeled proteins within a cell (27, 28). For example, fluorescence z-stack images have been used to track translocation of peripheral membrane proteins from the membrane to the cytosol initiated by an external stimulus by (29–31). The analysis of z-stack images provides a detailed record of the kinetics of the process from the time-resolved changes in the fluorescence intensity, but lacks the ability to determine the protein concentration at the plasma membrane, because a clean separation of the fluorescence signal in membrane-bound and cytoplasmic components is not feasible. However, these studies have the advantage of being performed within living cells rather than on model membranes.

Total internal reflection fluorescence (TIRF) microscopy is another popular technique for studying both the spatial distribution and dynamics of proteins at the plasma membrane. The evanescent field at the glass / solution interface only extends

~100 nm into solution (32, 33), which efficiently penetrates the plasma membrane in contact with the glass coverslip, and offers great contrast for observing membrane proteins, because proteins deeper within the cytoplasm are not excited. TIRF microscopy has been applied to studying cytoskeletal dynamics, focal adhesions, membrane trafficking, intracellular signaling, and many other processes (34). Additionally, when used in combination with Number and Brightness Analysis (35), it is possible to determine the relative oligomeric state of proteins at the plasma membrane compared to a plasma membrane control protein (36–38). One inherent problem with TIRF microscopy is once again linked to quantification. The plasma membrane often is not in contact with the coverglass at all places over the cell surface. This small but variable distance between the membrane and glass leads to fluorescence intensity variations that can complicate quantitative analysis. Furthermore, there is a small but pervasive signal from the cytoplasm (especially for peripheral membrane proteins) that must be accounted for in order to avoid misinterpretations of the data.

Fluorescence correlation spectroscopy (FCS) has been widely used to characterize the dynamics of both lipids and proteins at the plasma membrane (39–42). The implementation of scanning techniques like circular scans (43), line scans (44, 45), and z-scans (46, 47) has allowed FCS to be effectively applied to proteins with characteristically slow diffusion times within the membrane's spatially constrained environment. Brightness measurements at the plasma membrane have also been performed, but these studies only account qualitatively for the influence of neighboring layers on the measurement (4–6). Because the validity of this approach has never been

tested, it is unclear when and where traditional analysis breaks down. Since FFS measurements of brightness have tremendous potential for live-cell applications, it is imperative to develop FFS into a robust technique with a well-defined theory for the quantification of protein association on and off the plasma membrane.

1.2.4 Surface plasmon resonance

Surface plasmon resonance (SPR) is an optical technique that senses index of refraction changes at a metal surface to probe protein-lipid interactions, as well as protein-protein interactions in real time without any label (21, 22, 48, 49). In an SPR set-up, specialized sensor chips, typically consisting of a thin film of metal placed on a glass surface, are covered with immobilized lipids. This chip is placed in a flow cell where surface plasmons are generated by directing incident light towards the surface at a critical angle (21, 22, 48). A solution containing the protein of interest is then applied to the cell; a change in the refractive index occurs if the proteins interact with the lipids. This change in refractive index is measured in real time and determines the amount of protein binding. By varying the concentration of protein in the solution, the binding parameters between the lipid and protein can be determined (21, 22, 48). The advantage of this method is the real time measurement of protein-lipid interactions without any external labels. The disadvantage is that it is almost entirely restricted to model membrane systems because of the specialized sensor chips.

1.3 Overview of thesis

While the techniques briefly mentioned above have contributed enormously to our understanding of protein binding to membranes, they are either restricted to *in-vitro* environments or lack quantitative capabilities when applied to cells. Thus, there is a significant need for the development of quantitative techniques that probe proteins at the plasma membrane / cytoplasm interface of a live cell, in general, and for probing their oligomeric state in particular. Traditional FFS shines when it comes to identifying a protein's oligomeric state in a uniform environment. The presence of the cytoplasm and membrane introduces spatial nonuniformity, which leads to a breakdown of traditional FFS analysis. Addressing this issue is the main focus of this thesis.

Many processes within the cell involve hetero-species protein interactions, such as a peripheral membrane protein interacting with an integral membrane protein. While dual-color FFS characterizes such hetero-interactions, the expression level of the two proteins provides an experimental challenge, because variations in the expression ratio lead to a large cell to cell scatter of the binding data. In chapter 3, we develop and introduce a quantitative model that describes the average as well as the distribution of the protein coexpression ratio from a cell population. We show that the expression ratio is proportional to the molar plasmid ratio and relate the distribution to the finite number of active plasmids in the cell. While the rest of the thesis primarily focuses on homo-interactions (with single-color measurements) the lessons learned in chapter 3 will help construct the competition studies introduced in chapter 6.

As previously mentioned, traditional FFS is not equipped to deal with the spatial nonuniformity introduced by fluorescence emanating from the cytoplasm and the plasma membrane. In chapter 4, we address this issue by developing z-scan FFS, which combines an axial scan through the cell with FFS point measurements. Using z-scan FFS we were able to simultaneously determine the oligomeric state of proteins in the cytoplasm and at the membrane. We applied the technique to study the matrix domain of the Gag polyprotein from Human T-cell lymphotropic virus Type 1 (HTLV-1), which binds to the plasma membrane, to investigate the early steps of the viral assembly process.

Chapter 5 focuses on the z-scan intensity profile described in chapter 4 and the accurate partitioning into its cytoplasmic and membrane-bound fluorescence contributions, a process we refer to as z-scan fluorescence profile deconvolution (FPD). Using the cellular brightness of enhanced green fluorescent protein (EGFP), the fluorescence intensities are converted into concentrations at the membrane and in the cytoplasm. We experimentally validate the technique, characterize both the resolvability and stability of z-scan measurements and apply z-scan FPD in a time-resolved manner to monitor the reversible association of peripheral membrane proteins to the plasma membrane.

In chapter 6, we apply z-scan FPD to quantify the binding curve of proteins to the plasma membrane in living cells. Analysis of the experimental binding curve determines the binding affinity and the saturation concentration of binding sites. We examined the protein-lipid interactions of selected protein binding domains and evaluated the feasibility

of competition binding experiments to identify the specificity of lipid-protein interactions in living cells. Finally, we characterize the membrane binding curve of HTLV-1 matrix and determine its lipid-specificity.

Chapters 3, 4, and 5 are based on work that is already published (50, 51). Chapters 5 and 6 contain results that have been accepted for publication in Analytical Biochemistry (52) and the Biophysical Journal, respectively.

2. Fluorescence Fluctuation Spectroscopy (FFS)

This chapter provides background information on the instrumentation and analysis methods used within this thesis.

2.1 Concept of FFS

The excitation of fluorescent proteins within a sub-micron observation volume created on a microscope gives rise to a fluorescence signal along with fluctuations around its mean value (Figure 2.1A). The passage of individual fluorescent proteins in and out of the small observation volume (Figure 2.1B) creates fluctuations in the measured fluorescence intensity. These fluctuations contain information about molecular brightness (a measure of protein association), concentration, and diffusion time of the protein within the excitation volume, as conceptually illustrated in Figure 2.1C, where each burst in fluorescence corresponds to the transit of a fluorescent protein though the observation volume. The burst frequency corresponds to the protein concentration, the burst duration corresponds to the protein's diffusion time, and the burst amplitude corresponds to the protein brightness. Because the actual fluorescence signal contains many overlapping fluctuations, statistical analysis is needed to extract the brightness, concentration and diffusion information. We generally refer to the measurement and analysis of these fluorescence fluctuations as FFS.

A collection of statistical techniques including FCS, moment analysis, photon counting histogram (PCH) and others can be applied to analyze FFS data (53–55). FCS analyzes the temporal decay of the fluorescence autocorrelation function (ACF) to

determine the diffusion time and concentration of fluorescent molecules (56–59), while PCH determines the brightness and concentration of fluorescence species by analyzing the amplitude distribution of fluctuations (60). Moment analysis, which is based on the first two moments of the fluorescence intensity, offers a straightforward option for efficient on-the-fly analysis of fluctuations (61). Fluorescence cumulant analysis (FCA) extends moment analysis by providing rigorous error analysis of moments (62). Finally, time-integrated fluorescence cumulant analysis (TIFCA) improves the signal to noise ratio of moment analysis significantly by extending FCA to long sampling times (63). The FFS techniques used to analyze the data in this thesis are autocorrelation and moment analysis; they will be discussed in more detail below.

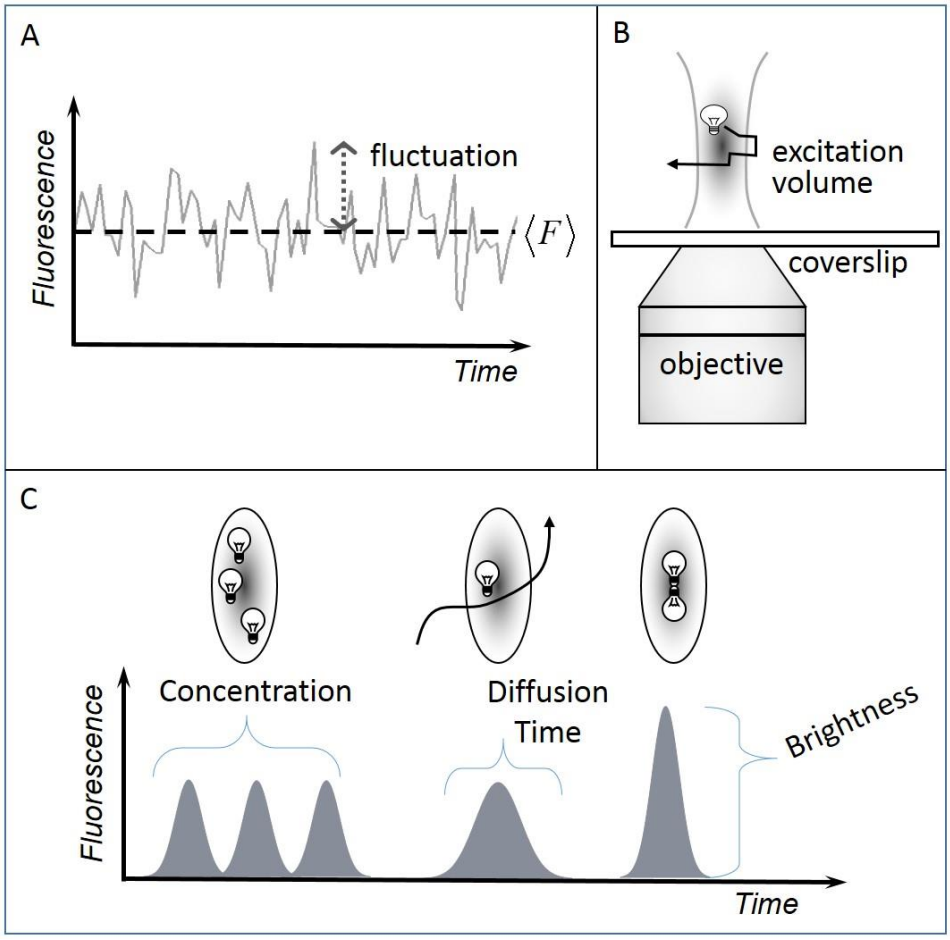

Figure 2.1 Fluorescence fluctuations from diffusing fluorescent proteins.
(*A*) The fluorescence intensity trace illustrates fluctuations around an average value as fluorescent proteins move in and out of the excitation volume. (*B*) The focused laser light creates a submicron excitation volume through which the fluorescent protein diffuses. (*C*) Conceptual illustration of the information content of intensity fluctuations.

2.2 Instrumentation

The small observation volume required for fluorescence fluctuation experiments is achieved through two-photon excitation (TPE), which involves the quasi-simultaneous absorption of two photons that together have enough energy to excite a fluorophore (64). TPE was first introduced to FFS by Berland et al. and has proven to be an excellent method for measuring in cells, because excitation only occurs at the focal point of the objective (65). This results in an inherent optical sectioning along the z-axis and limits photobleaching to the focal volume of the TPE spot. An additional advantage of TPE over one-photon excitation is the built-in color separation between excitation and emission spectra. Excitation occurs at near infrared wavelengths while the fluorescence emission is in the visible range, which greatly facilitates the removal of elastically and inelastically scattered excitation light from the detector by optical filters. The experimental setup of our two-photon microscope is shown in Figure 2.2. A mode-locked Ti:Sapphire laser (Tsumami or Mai Tai, Spectra-Physics, Mountain View, CA) produces ultra-short laser pluses (~100 fs) with a frequency of 80 MHz. The beam enters a Zeiss Axiovert 200 microscope (Zeiss, Gottingen, Germany) and is reflected onto the objective by the dichroic mirror (#740DCSPXR, Chroma, Rockingham, VT). The objective (Plan-Apochromat 63x oil immersion objective, N.A.=1.4, or C-Aprochromat 63x water immersion objective, N.A.=1.2, Zeiss, Gottingen, Germany) focuses the excitation light onto the sample and also collects the fluorescence signal from the TPE. The fluorescence signal passes through a dichroic mirror which transmits wavelengths between 400-750 nm and an additional bandpass filter to remove scattered laser light. For dual-color

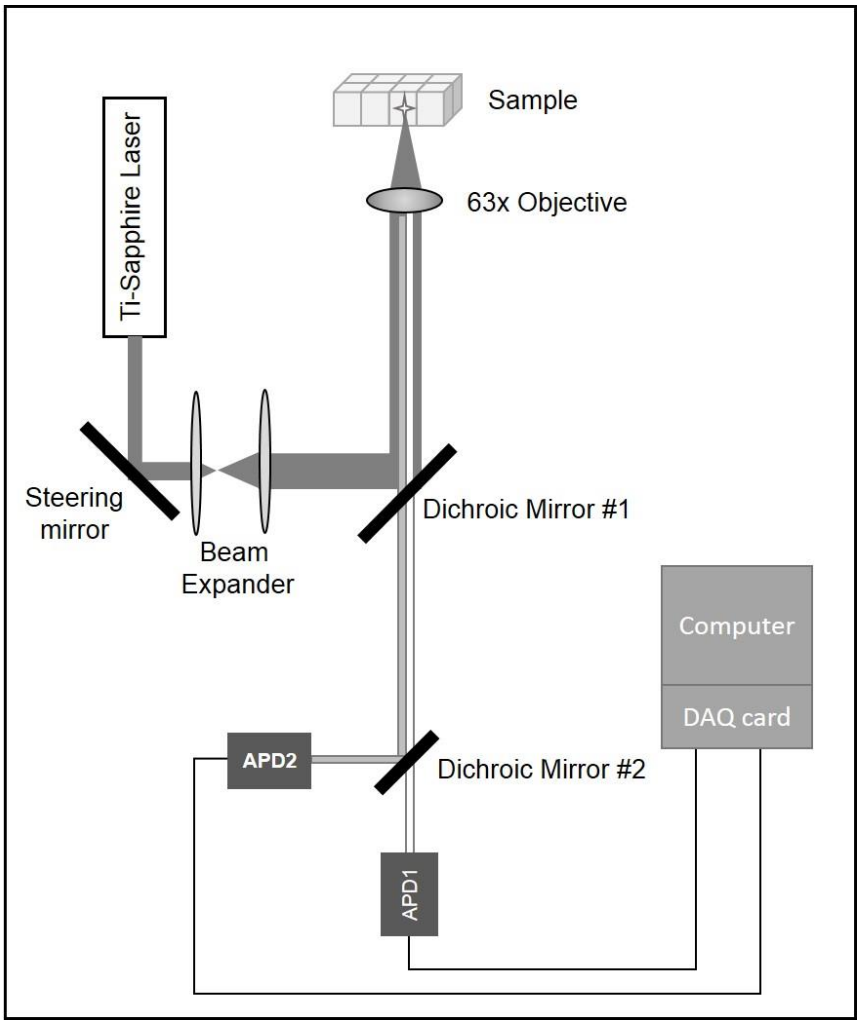

Figure 2.2 Experimental setup of the two-photon microscope.
The pulses produced by the Ti:Sapphire laser are steered through a beam expander onto a dichroic mirror (#1), which reflects the excitation light through the objective onto the sample. The fluorescence emission is collected by the objective and passed through the dichroic mirror (#1) to the detector. A second dichroic mirror (#2) can be placed before the avalanche photo diodes (APDs), to separate the fluorescence light based on color. TTL pulses from the APDs are recorded by a DAQ card and stored on the computer for further analysis.

measurements a second dichroic mirror splits the emission light into two different detection channels based on the emission wavelength. An avalanche photodiode (APD, SPCM-AQ-141, Perkin-Elmer, Dumberry, Québec) detects the signal in each channel and generates TTL pulses that are recorded by a data acquisition card (ISS, Champaign, IL or FLEX02, Correlator.com Bridgewater, NJ). The resulting photon counts are later analyzed using programs writing in IDL version 7.1 or later (Exelis Visual Information Solutions, Boulder, CO).

2.3 Analysis

2.3.1 Molecular brightness

We defined molecular brightness λ as the average number of photons emitted per molecule over a specific time period with units of counts per second (cps). A fluorescent protein like EGFP will have a distinct brightness that depends on the optics, excitation wavelength, excitation power, and detection efficiency (60, 66). The average fluorescent intensity of a protein ensemble is made up of the brightness of the individual protein complexes and the number of complexes.

2.3.2 Excitation point spread function

The spatial intensity distribution of the focused excitation laser beam plays an important factor in FFS theory and is referred to as the instrument's point spread function (PSF). Two different model functions have been widely used to approximate the PSF of

FFS experiments on a two-photon microscope. The first model is the squared Gaussian-Lorentzian (GL) function (65) given by,

$$PSF_{GL}(\rho,\zeta) = \left(\frac{w_0}{w(\zeta)}\right)^4 \exp\left(-\frac{4\rho^2}{w^2(\zeta)}\right) \tag{2.1}$$

with

$$w(\zeta) = w_0\left(1+\frac{\zeta^2}{z_0^2}\right)^{1/2}. \tag{2.2}$$

The variables ζ and ρ represent the axial and radial coordinates measured with respect to the center of the PSF. The radial and axial beam waists of the PSF are given by ω_0 and z_0. The second model function is given by the squared three-dimensional Gaussian (3DG) function,

$$PSF_{3DG}(\rho,\zeta) = \exp\left(-4\left(\frac{\rho^2}{w_0^2}+\frac{\zeta^2}{z_0^2}\right)\right), \tag{2.3}$$

with ω_0 and z_0 representing the radial and axial beam waists of the PSF. The 3DG-PSF was used to fit the autocorrelation data of this thesis.

The PSF is crucial for modeling, because it establishes a link to the experimental observables. For example, the fluorescence intensity at position $\vec{r}$ at time *t* from a solution containing fluorescent proteins with brightness λ is given by,

$$F\left(\vec{r}(t)\right) = \lambda c\left(\vec{r}(t)\right) PSF\left(\vec{r}\right), \tag{2.4}$$

where $c\left(\vec{r}(t)\right)$ is the concentration at that position and time.

Other important parameters frequently needed in FFS experiments include the volume of the PSF and the gamma factor. The volume of the PSF raised to the r-th power is given by:

$$V_{PSF^r} = \int PSF^r(\rho,\zeta)2\pi d\rho d\zeta \quad . \tag{2.5}$$

The variables ζ and ρ represent the axial and radial coordinates measured with respect to the center of the PSF and the integration was performed over all space. The gamma factor is a beam shape factor needed to recover the brightness of a sample; it is given by (67),

$$\gamma_{2,\infty} = \frac{V_{PSF^2}}{V_{PSF}} \tag{2.6}$$

For the PSF models mentioned in section 2.3.1, the γ_2 values are $\gamma_2 = 1/\left(2\sqrt{2}\right)$ for the three-dimensional Gaussian PSF and $\gamma_2 = 0.1875$ for the squared Gaussian-Lorentzian PSF.

2.3.3 Autocorrelation and moment analysis

The autocorrelation function (ACF) is defined by,

$$G(\tau) = \frac{\left\langle \delta F(t)\delta F(t+\tau)\right\rangle}{\left\langle F\right\rangle^2}, \tag{2.7}$$

where *F*(t) is the fluorescence intensity at time *t* and $\delta F(t) = F(t) - \left\langle F\right\rangle$ is the fluctuation about the average fluorescence intensity (67). For fluorescent molecules diffusing through a 3DG-PSF, the autocorrelation function is given by (67),

$$G(\tau) = \frac{G(0)}{\left(1 + \frac{\tau}{\tau_D}\right)\left(1 + \frac{\tau}{s^2 \tau_D}\right)^{1/2}}, \tag{2.8}$$

where $s = z_0 / w_0$ is the beam waist ratio. The diffusion time τ_D of a molecule with diffusion coefficient D is given by $w_0^2 / 8D$ in the case of TPE. The ACF of an EGFP sample is shown in Figure 2.3 together with a fit (line) by Equation 2.8 to determine τ_D and the time-zero value *G(0)*, which is also called the fluctuation amplitude.

The fluctuation amplitude *G(0)* is inversely proportional to the average number of molecules *N* in the excitation volume and also determines the average protein concentration *c*,

$$G(0) = \frac{\gamma_2}{N} = \frac{\gamma_2}{c \cdot V_{PSF}}, \tag{2.9}$$

where V_{PSF} represents the volume of the PSF and γ_2 is its gamma factor.

The G(0) value can also be obtained from moment analysis. The first intensity moment is given by the average fluorescence intensity $\langle F \rangle$, while the second moment is given by the variance in the fluorescent intensity $\langle \Delta F^2 \rangle$,

$$\begin{aligned} \langle F \rangle &= \lambda N \\ \langle \Delta F^2 \rangle &= \gamma_2 \lambda^2 N \end{aligned}. \tag{2.10}$$

N is the number of fluorescent molecules within the PSF volume, λ is the molecular brightness of the molecules, and γ_2 is the PSF shape factor. While fluorescence intensities are in many cases sufficient for modeling data, our experiments

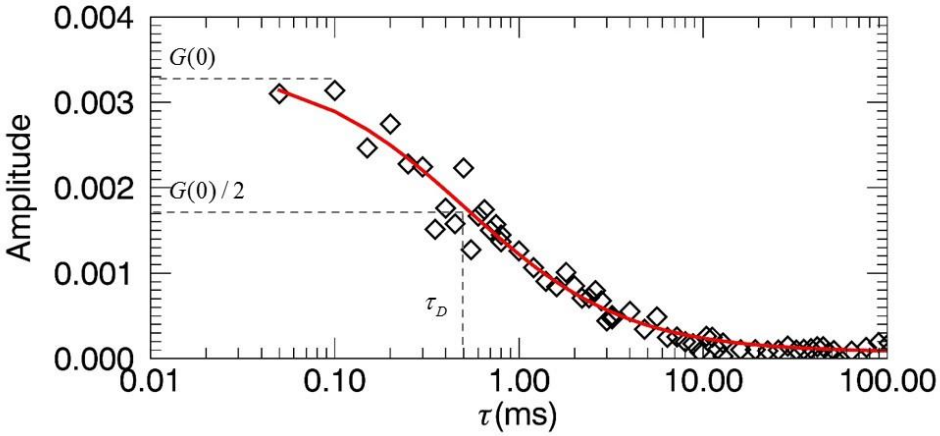

Figure 2.3 Autocorrelation curve for EGFP in a cell.

The autocorrelation curve (*diamonds*) decays as a function of its lag time τ. The fit (*solid line*) of the data to Eq. 2.8 determines $G(0)$ and τ_D. The diffusion time τ_D can also be estimated from the graph by identifying the lag time that corresponds to half the fluctuation amplitude $G(0)$.

do not record fluorescence intensities, but rather photon counts. Because photon counting includes shot noise, we have to use photon count moments to properly analyze FFS data. The first two moments in terms of photon counts *k* per sampling time T are (62),

$$\begin{aligned} \langle k \rangle &= \lambda T N \\ \langle \Delta k^2 \rangle &= \langle k \rangle + \gamma_2 (\lambda T)^2 N \end{aligned} \tag{2.11}$$

where the variance includes and additional term $\langle k \rangle$ to account for the shot noise contribution (68, 69). The above equations are valid in the absence of undersampling (63, 70). Eqs. 2.8 and 2.9 can be used to calculate *G*(0),

$$G(0) = \frac{\langle \Delta F^2 \rangle}{\langle F \rangle^2} = \frac{\langle \Delta k^2 \rangle - \langle k \rangle}{\langle k \rangle^2} \ . \tag{2.12}$$

2.3.4 Mandel's Q-parameter

We calculate Mandel's Q-parameter, which is directly proportional to brightness, by moment analysis (60, 71),

$$Q = \frac{\langle \Delta k^2 \rangle - \langle k \rangle}{\langle k \rangle} = G(0) \langle k \rangle = \gamma_2 \lambda T \tag{2.13}$$

The brightness λ is calculated from Q with the help of the sampling time *T* and the PSF shape factor γ_2. The relation between the Q-parameter and the fluctuation amplitude *G*(0) as can be seen through inspection of Eqs. 2.11 and 2.12.

2.3.5 Stoichiometry

The brightness λ_{EGFP} of EGFP can be used to identify the oliogmeric state or stoichiometry of a protein complex of interest. After measuring the brightness λ of a protein tagged with EGFP, we convert its value into a normalized brightness by dividing λ by the reference brightness λ_{EGFP} of the monomeric label,

$$b = \frac{\lambda}{\lambda_{EGFP}} \tag{2.14}$$

As shown in Figure 2.4, the normalized brightness of a monomeric protein is $b = 1$. A dimeric protein complex has two labels per complex and therefore a normalized brightness of $b = 2$. A trimeric complex with three labels per complex will have $b = 3$, and so on. The brightness λ_{EGFP} of EGFP has proven to be a robust parameter for determining protein stoichiometry in living cells. Chen and colleagues showed that the monomeric brightness of EGFP is stable inside a living cell (1) and that it was possible to measure a dimer brightness for a tandem $EGFP_2$ complex (2). Our lab has more recently demonstrated that brightness analysis can be extended to higher-order complexes (like virus-like particles, VLPs) containing hundreds to thousands of protein copies (72–74).

Quantitative brightness measurements rely on a careful calibration of the experimental brightness on a daily basis. We routinely measure EGFP and $EGFP_2$ expressed in living cells to make sure both brightnesses are stable over an extended concentration range and have a 1:2 brightness ratio, respectively (66, 75). Establishing a robust monomeric and dimeric protein system that serves as a brightness standard is crucial whenever the technique is extended to new sample environments.

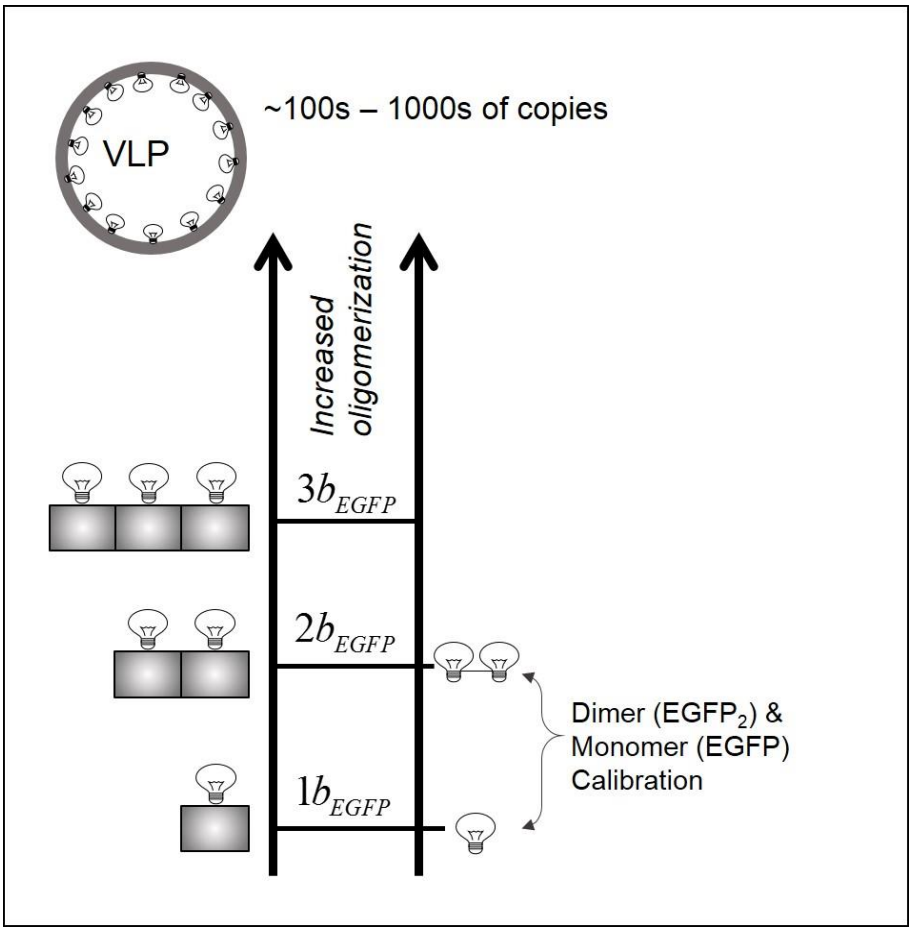

Figure 2.4 Protein brightness and stoichiometry.
The normalized brightness of a protein is used to identify a protein's oligomeric state. Calibration measurements of EGFP and a tandem dimeric $EGFP_2$ are used to determine the monomer and dimer rungs of the brightness ladder depicted above.

2.3.6 Apparent brightness and brightness titration

Inside of the cell, proteins tagged with EGFP typically exist as a mixture of oligomeric states which gives rise to an apparent brightness (2, 66),

$$b_{apparent} = \frac{\sum_{i}^{n} b_i^2 N_i}{\sum_{i}^{n} b_i N_i} \tag{2.15}$$

The apparent brightness corresponds to a weighted average over all the brightness states b_i present in the cell with N_i representing the number of molecules in the excitation volume with brightness b_i. We will continue to report the apparent brightness of a protein throughout to rest of this thesis, but it will simply be noted as *b* rather than $b_{apparent}$.

We explore the concentration dependence of brightness by performing FFS measurements on cells with a wide range of protein expression levels, which we refer to as a brightness titration experiment. A plot of the apparent brightness versus the monomeric protein concentration characterizes the concentration dependence of protein complex formation (2, 75). A purely monomeric protein will remain monomeric while a protein that forms a homo-dimer will show a concentration-dependent transition as illustrated in Figure 2.5.

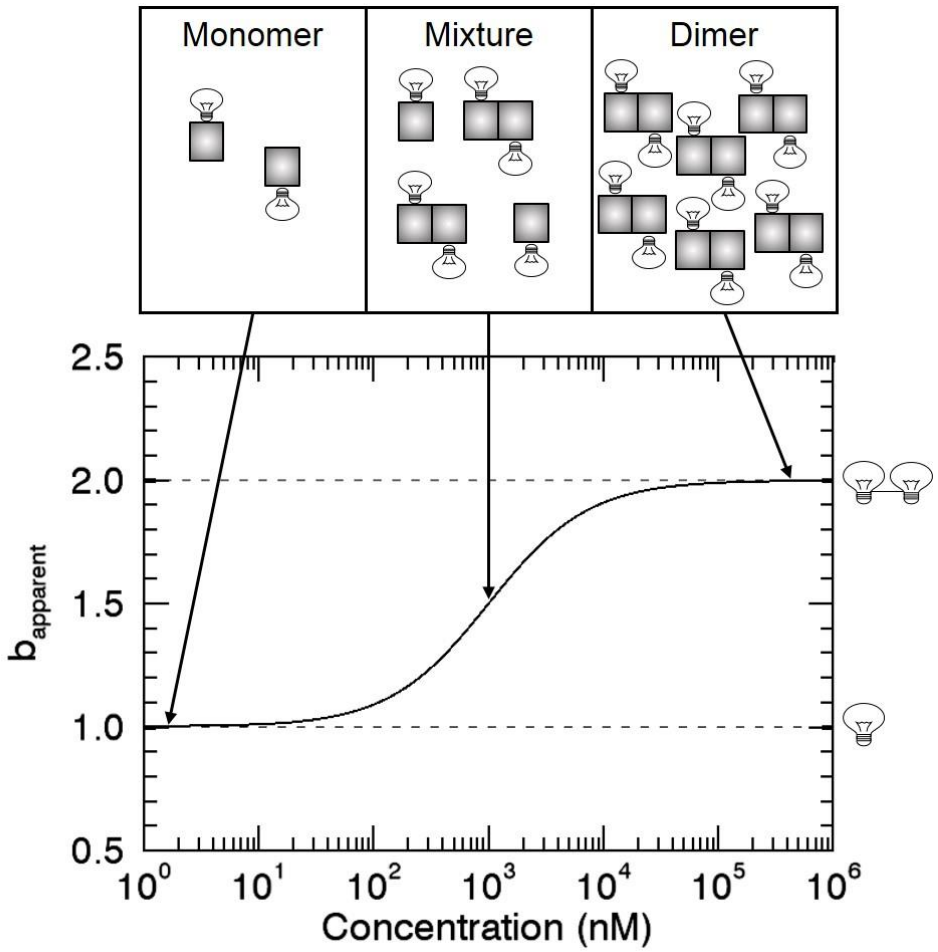

Figure 2.5 Brightness titration experiment.
Conceptual plot of brightness as a function of protein concentration for cells expressing an EGFP-labeled protein with a dissociation coefficient of 1 µM. The normalized brightness increases from 1 to 2 as a function of concentration.

2.4 z-scan FFS

2.4.1 Brightness bias in confined geometries

Conventional brightness measurements have been performed in solution and within thick regions of a cell. These measurments assume that fluorescent molecule diffuses through all areas of the PSF with equal probability. This assumption, however, breaks down at thin cell sections of the cell because the excitation volume extends beyond the sample's thickness. Under such conditions, the fluorescent molecule cannot access all areas of the PSF, which results in an incorrect interpretation of brightness in conventional FFS analysis (76). To address this brightness bias our lab developed z-scan FFS (51, 76).

2.4.2 Fluorescence intensity profile

Consider a thin cell slab that starts at $z = 0$ and ends at $z = h$. We describe this geometry of the cytoplasmic protein in Figure 2.6 with a boxcar shape factor S given by (76),

$$S(z;0,h) = \begin{Bmatrix} 1, & 0 < z < h \\ 0, & otherwise \end{Bmatrix}. \tag{2.16}$$

Additionally, we introduced a z-dependent generalized PSF volume function that accounts for the spatial overlap between the sample and the PSF (76),

$$V_{PSF^r}(z,h) = \int PSF^r(\rho,\zeta) \cdot S(z+\zeta) \cdot 2\pi\rho d\rho d\zeta \ , \tag{2.17}$$

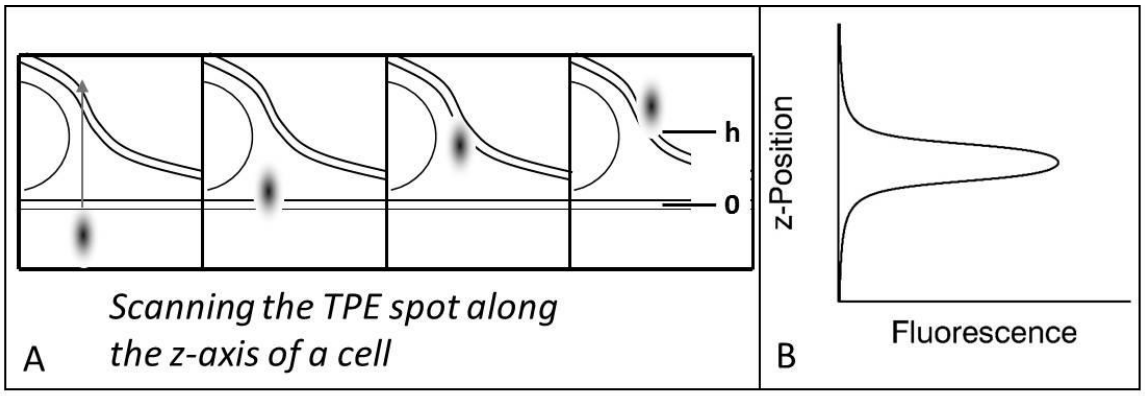

Figure 2.6 Conceptual cartoon of a z-scan experiment.
(*A*) The focused beam is uniformly scanned along the axial direction through a cell expressing a homogenously distributed cytoplasmic protein. (*B*) The resulting z-scan fluorescence intensity profile.

where the variables ζ and ρ represent the axial and radial coordinates measured with respect to the center of the PSF. For a homogeneously distributed cytoplasmic protein the first two moments of the fluorescence intensity are given by (51, 76),

$$\begin{aligned} \left\langle F\left(z\right)\right\rangle &= \lambda c V_{PSF}\left(z;h\right) \\ \left\langle \Delta F^{2}\left(z;h\right)\right\rangle &= \lambda^{2} c V_{PSF^{2}}\left(z;h\right) = \gamma_{2}\left(z;h\right)\lambda^{2} c V_{PSF}\left(z;h\right) \end{aligned} \tag{2.18}$$

A uniform scan of the PSF along the z-axis of a cell (Figure 2.6A) generates a z-dependent fluorescence intensity profile (Figure 2.6B), which is described by $\left\langle F\left(z\right)\right\rangle$.

2.4.3 Brightness bias and gamma factor

All FFS analysis methods rely on the γ_2 shape factor to recover the brightness of the sample. In conventional FFS the shape factor $\gamma_{2,\infty}$ remains constant for a given PSF model. However, when FFS is performed in thin samples, the gamma factor will depend on the z-position and the cell height. To address this issue, we define a z-dependent gamma factor as (76),

$$\gamma_{2}\left(z;h\right) = \frac{V_{PSF^{2}}\left(z;h\right)}{V_{PSF}\left(z;h\right)} \tag{2.19}$$

where $V_{PSF^{2}}(z;h)$ and $V_{PSF}(z;h)$ are determined from Eq. 2.17.

Macdonald et al. demonstrated the need for a proper γ_2 shape factor by performing a series of brightness measurements of EGFP in cells and applying conventional FFS analysis based on $Q_{\infty} = \gamma_{2,\infty} \cdot \lambda$. The analysis recovered a monomeric brightness of b = 1 at the thickest section of the cell, but erroneously identified an

apparent increase to 1.8 at the thinnest layers (76). This artifact was eliminated by accounting for the cell thickness in brightness analysis with the z-dependent gamma factor (76),

$$Q(z;h) = \gamma_2(z;h) \cdot \lambda \ . \tag{2.20}$$

When the PSF volume extends beyond the height of the sample $\gamma_2(z;h)$ must replace $\gamma_{2,\infty}$ in all brightness calculations.

2.4.4 Improved PSF model

Initial z-scan experiments revealed that neither the GL nor the 3DG model are sufficient to approximate the experimental profile of our PSF (76). This issue was resolved by introducing the modified squared Gaussian-Lorentzian function (mGL) (76),

$$PSF_{mGL}(\rho,\zeta) = \left(\frac{z_0^2}{z_0^2 + \zeta^2} \right)^{(1+y)} \exp\left(-\frac{4z_0^2}{w_0^2} \frac{\rho^2}{z_0^2 + \zeta^2} \right), \tag{2.21}$$

where ω_0 and z_0 are the radial and axial beam waist and the *y* parameter adjusts the axial decay of the PSF while maintaining a radial Gaussian profile. This mGL-PSF is the model that will be used for all z-scan experiments described in this thesis.

3. The Statistics of Protein Expression Ratios

In this chapter we explore the statistics of transient cotransfection and subsequent protein coexpression. Fluorescence studies of cellular protein-protein interactions commonly employ transient transfection to express two proteins carrying distinct fluorescent labels. Because transiently transfected cells differ significantly in their expression level, the concentration ratio of the two expressed proteins varies, which in turn influences the measured fluorescence signal. Knowledge of the statistics of protein expression ratios is of considerable interest both from a fundamental point of view and for cellular fluorescence studies. Despite the perceived randomness of transient transfection, we were able to develop a quantitative model that describes the average and distribution of the protein expression ratio from a cell population. We show that the expression ratio is proportional to the molar plasmid ratio and relate the distribution to the finite number of active plasmids in the cell. The process of cationic lipid-mediated transfection is explored in more detail. Specifically, the influence of lipoplexes on the statistics of the expression ratio is examined. We further demonstrate that the transfection model provides a quantitative description of fluorescence fluctuation experiments, where only a fraction of the proteins are labeled.

3.1 Introduction

Transient transfection is an important technique for the transfer of DNA into cultured mammalian cells. Because transient transfection is simple, fast, and permits the convenient transient expression of foreign genes, it has become an essential tool for cell

biological studies. A powerful approach for the study of protein behavior inside a cell is the direct visualization of the protein by tagging it with a EGFP or one of its derivatives (77, 78) . The fluorescent signal from the tagged protein provides important information about localization, mobility, transport, and interactions of the protein (79, 80). Thus, transient transfection of EGFP-tagged 'fusion' proteins is widely utilized in live cell studies.

Experiments that probe protein interactions, such as FRET and FCS often rely on dual-color fluorescence studies, where two proteins tagged with distinct fluorescent proteins are coexpressed in the same cell (81–83). While it's known that transient transfection results in a large cell to cell variability of protein expression, the properties of the expression ratio between two coexpressed proteins is relatively unknown. This ratio is important for cellular fluorescence studies because it affects the measured fluorescence signal and also provides insights into fundamental aspects of transient transfection.

In this chapter, we aim to quantify transient cotransfection through the introduction of a simple model that describes the mean, standard deviation, and distribution of the protein coexpression ratio. We explicitly relate the mean of the expression ratio to the plasmid DNA molar ratio of the transfection solution and extend the model to include the variability of protein expression. The model is compared against experimental data and the simplifying assumptions of the model are discussed. Our study also sheds light on the cationic lipid-mediated transfection process. Although this transfection method was introduced over two decades ago (84), some details are still

unclear, and only limited work has examined the process of quantitative cotransfection (85). Here, we specifically investigate the role of lipoplexes in the transfection process. We demonstrate that only very few lipoplexes contribute successfully to gene expression and discuss the resulting consequences for protein expression ratios. Although our model simplifies many details of the transfection process, it still reproduces the data remarkably well.

Modeling of the relation between the expression ratio and the molar plasmid ratio of the transfection solution is also extremely useful in application. With the model, it is now possible to adjust the expression ratio in a predictive fashion, which is desirable for optimizing protein interactions in fluorescence studies. Our model predicts that this adjustment is limited to a finite range, as is dictated by properties of the transient transfection process. Additionally, being able to statistically describe the cell to cell variability of the protein expression ratio allows us to study its influence on the outcome of specific cellular fluorescence studies.

We introduce and apply our model to a ‘bright and dark’ fluorescence fluctuation experiment, where only a fraction of the proteins carry a fluorescent label. The unlabeled protein is non-fluorescent and cannot be directly observed in FFS experiments. For this reason, we frequently refer to the unlabeled protein as a dark protein and experiments that coexpress a labeled protein together with an unlabeled protein as bright and dark experiments. Because labels potentially interfere with the assembly of protein complexes, it is useful to establish control experiments that detect such an artifact. A bright and dark experiment has the potential to identify label artifacts, but requires knowledge of the

statistics of protein expression ratios because the amount of dark protein directly influences the measured signal. We demonstrate that the transfection model establishes a framework for interpretation of FFS bright and dark experiments.

3.2 Methods and materials

3.2.1 Experimental setup

Experiments were performed with the instrument setup described in chapter 2. All measurements were taken with a 1000 nm excitation wavelength and an average power after the objective of 0.25 mW. For dual-channel measurements, a dichroic mirror with a center wavelength of 525 nm split the fluorescence emission into two detection channels. The fluorescence in each channel was detected by an avalanche photodiode (APD, SPCM-AQ-141, Perkin-Elmer, Dumberry, Quebec). The dichroic mirror was removed during single-channel measurements. The TTL output from each APD is recorded by a PCI data acquisition card (ISS, Champaign, IL). Data was acquired at a frequency of 20 kHz for ~10 seconds for intensity fraction measurements and for ~1 minute for brightness measurements. The photon counts were analyzed with programs written in IDL 7.1 (Research Systems, Boulder, CO).

3.2.2 Sample Preparation

pEGFP-C1 and pEYFP-C1 plasmids were purchased from Clontech (Clontech, Palo Alto, CA). Tandem dimeric EGFP ($EGFP_2$), RXRLBD-EYFP, RXRLBD-EGFP, and RARLBD-EYFP plasmids were constructed as previously described (2, 3). EGFP-

endophilin A2 (Endo-EGFP) plasmids were a gift from Dr. Joseph Albanesi (University of Texas Southwestern Medical Center). All sequences were verified by automatic sequencing.

CV-1 cells were obtained from ATCC (Manassas, VA) and maintained in 10% fetal bovine serum (Hycolone Laboratories, Logan, UT) and DMEM medium. Cells were subcultered in eight-well coverglass chamber slides (Naglenunc International, Rochester, NY) 12 hours before transfection. Transient transfections were carried out using TransFectin (BioRad, Hercules, CA) according the manufacturer's instructions 24 hours prior to measurement. For cotransfections, a standard protocol was followed with the two plasmid types mixed together at a given mole ratio prior to adding TransFectin. In one specific case, a second cotransfection protocol was employed where TransFectin was added to specific plasmids (rather than the plasmid mixture) to form pDNA/lipid complexes which only contained one type of pDNA. The pDNA/lipid complexes containing each type of pDNA were then mixed together at a given mole ratio. In each transfection protocol, ~0.2 μg of total pDNA was added to each well. Immediately before measurement, the growth medium was replaced with Dulbecco's phosphate-buffered saline (PBS) with calcium and magnesium (Biowhittaker, Walkerville, MD). Measurements of EGFP, EYFP, $EGFP_2$, RXRLBD-EYFP, RXRLBD-EGFP, RARLBD-EYFP were carried out in the cell nucleus while measurements of Endo-EGFP and Endo were carried out in the cell cytoplasm.

3.3 Theory

3.3.1 Dual color expression fraction

The average detected fluorescence intensity $\langle F \rangle$ is given by

$$\langle F \rangle = \lambda N \tag{3.1}$$

where the brightness λ is the average photon count rate for a single molecule and *N* is the detected number of molecules (62). In two channel measurements, the emitted fluorescence from a single fluorophore is split by a dichroic filter into two detection channels ("red" and "green"). The average fluorescence intensity in the green channel is $\langle F^{(g)} \rangle = \lambda^{(g)} N$ and that of the red channel is $\langle F^{(r)} \rangle = \lambda^{(r)} N$, where $\lambda^{(g)}$ and $\lambda^{(r)}$ are the brightness values of the green and red channel, respectively. Because both detectors see the same number of molecules, the fluorescence intensity fraction of the red channel,

$$f_I = \frac{F^{(r)}}{F^{(r)} + F^{(g)}} = \frac{\lambda^{(r)}}{\lambda^{(r)} + \lambda^{(g)}} \tag{3.2}$$

equals the brightness fraction. The emitted color of the fluorescent protein together with the dichroic filter determines the intensity fraction.

In a mixture of two non-interacting proteins with distinct labels, the intensity fraction of the red channel is now determined by (3)

$$f_I = \frac{F^{(r)}}{F^{(r)} + F^{(g)}} = \frac{\lambda_G^{(r)} N_G + \lambda_Y^{(r)} N_Y}{\lambda_G^{(g)} N_G + \lambda_Y^{(g)} N_Y + \lambda_G^{(r)} N_G + \lambda_Y^{(r)} N_Y} \tag{3.3}$$

where the subscripts G and Y refer to the fluorescent proteins, EGFP and EYFP. For this study we assume no FRET is occurring between the two proteins. Chen et al. describes

how, if necessary, FRET is taken into account (3). By rewriting Eq. 3.3 we relate the protein expression fraction to experimentally determined parameters,

$$f_N = \frac{N_Y}{N_Y + N_G} = \frac{f_I(\lambda_G^{(g)} + \lambda_G^{(r)}) - \lambda_G^{(r)}}{f_I(\lambda_G^{(g)} + \lambda_G^{(r)} - \lambda_Y^{(g)} - \lambda_Y^{(r)}) - \lambda_G^{(r)} + \lambda_Y^{(r)}}. \quad (3.4)$$

The calibration parameters $(\lambda_G^{(r)}, \lambda_G^{(g)}, \lambda_Y^{(r)}, \lambda_Y^{(g)})$ are the brightness values of the fluorescent proteins (G = EGFP, Y = EYFP) in each detection channel (r = 'red' channel, g = 'green' channel) and are determined from separate FFS measurements of cells expressing EGFP or EYFP alone. For example $\lambda_G^{(r)}$ and $\lambda_G^{(g)}$ are the brightness values for EGFP in the red and green channel respectively. The brightness values for EGFP and EYFP in each channel account for the differences in detected photon count rates; when used in combination with the fluorescent intensity fraction (Eq. 3.3) the protein expression fraction for any cell can be determined.

3.3.2 Model for protein expression ratios

We introduce a simple linear model to describe the molar amount of protein υ_P expressed in a cell,

$$\upsilon_P = x \cdot \eta \cdot N_A \quad (3.5)$$

where N_A presents the number of active plasmids in the cell, η is an efficiency factor, and x takes environmental and cell-specific factors that influence protein expression into account. The amount of expressed protein is expected to be directly proportional to the number of active plasmids N_A presuming that sufficient cellular resources are present. The expression efficiency of individual genes within a plasmid varies. For example,

mRNA translational efficiency is influenced by its sequence (86). These differences are described by the efficiency factor η. More generally, the factor η can be used to account for transcription- and translation-related factors influencing expression efficiency. For example, we expect that changing the promoter affects the value of the efficiency factor. However, this work only considers plasmids with the same promoter. Protein expression depends on many additional environmental and cell-specific factors. For example, the entry of plasmid DNA (pDNA) into the nucleus after transfection is expected to vary from cell to cell, which would lead to a distributed start time of protein production in a cell population. The compound effect of these diverse factors on the amount of expressed protein is symbolically described by the parameter x.

The presence of two types of plasmids ($pDNA_1$ and $pDNA_2$) in a cell leads to the coexpression of two proteins. The ratio of the molar amount of expressed protein, $r_P = \upsilon_1 / \upsilon_2$, is according to Eq. 3.5 directly proportional to the active plasmid number ratio, $r_A = N_{A1} / N_{A2}$,

$$r_P = \frac{x_1}{x_2} y \cdot r_A \approx y \cdot r_A \tag{3.6}$$

with $y = \eta_1 / \eta_2$. It is expected that $x_1 \approx x_2$ in the same cell. This statement assumes that the variance in the ratio of x_1 and x_2 is sufficiently small such that the protein ratio r_P is mainly determined by y and r_A. A summary of the relevant parameters can be found in Table 3.1.

Symbol	Definition
r_P	Protein expression ratio
r_S	Molar ratio of pDNA in solution
r_A	"Active" plasmid ratio
η_i	Factor accounting for protein specific expression efficiency of $pDNA_i$
y	Efficiency ratio = η_1 / η_2
f_P	Protein expression fraction
f_S	Molar fraction of pDNA in solution
f_A	"Active" plasmid fraction
b	Normalized brightness

Table 3.1: Definition of parameters

The relative protein ratio in terms of expressed protein concentration, $r_P = c_1/c_2$, is experimentally measurable. In contrast, neither y nor r_A is directly measurable. The only other experimental quantity under our control is the molar mixing ratio r_S of pDNA in solution. Transfection leads to the uptake of plasmid by the cell. Only a small fraction of the transfected plasmids will ultimately be involved in active gene expression (87, 88). We refer to such plasmids as active. The events that lead to an active plasmid are not yet fully understood, as will be discussed at a later point. Because very few plasmids become active, small number fluctuations become important. Thus, the ratio r_A of active plasmids of $pDNA_1$ and $pDNA_2$ will vary across cells. However, while the ratio r_A varies, the average of the active plasmid ratio equals the molar mixing ratio of pDNA in solution, $\langle r_A \rangle = r_S$. This statement reflects that cells treat the two types of plasmids as equal. Neither uptake nor activation of a plasmid is expected to depend on the particular type of plasmid ($pDNA_1$ or $pDNA_2$), as long as the plasmids are of comparable length. Thus, the average active plasmid ratio must reflect the plasmid ratio in solution. This statement together with Eq. 3.6 predicts that the average protein ratio from a population of cells will be proportional to the molar ratio of pDNA in solution scaled by the relative efficiency factor,

$$\langle r_P \rangle \approx y \cdot \langle r_A \rangle = y \cdot r_S \,. \tag{3.7}$$

This linear relationship can be experimentally tested, because both r_P and r_S can be measured.

Eq. 3.7 describes the average behavior. As mentioned earlier the active plasmid ratio will vary from cell to cell. Thus, according to Eq. 3.6 the expressed protein ratio r_P will reflect these variations in r_A. The probability distribution function (pdf) of both quantities are related by,

$$\mathrm{pdf}_P(r_P)\,dr_p = \mathrm{pdf}_A(r_A)\,dr_A. \tag{3.8}$$

The probability distribution function $\mathrm{pdf}_P(r_P)$ of the expressed protein ratio can be measured, but we require a model for the probability distribution function $\mathrm{pdf}_A(r_A)$ of the active plasmids.

It is advantageous to use fractions instead of ratios for graphing and comparing distributions. Thus, we convert each ratio r into its corresponding fraction $f = r/(1+r)$. By transforming Eq. 3.7 into fractions we get

$$\langle f_P \rangle \approx \frac{y\langle f_A \rangle}{1+\langle f_A \rangle (y-1)} = \frac{y \cdot f_S}{1+ f_S (y-1)} \tag{3.9}$$

for the average protein fraction $f_P = r_P/(1+r_P)$. The equivalent transformation for the probability distribution functions of Eq. 3.8 leads to

$$\mathrm{pdf}_P(f_P)\,df_P = \mathrm{pdf}_A(f_A)\,df_A \tag{3.10}$$

for the pdf of the protein expression fraction. Note that the distributions of f_P and f_A become identical for the special case of $y = 1$,

$$\mathrm{pdf}_P(f_P) = \mathrm{pdf}_A(f_A). \tag{3.11}$$

3.4 Results

3.4.1 Average protein expression fraction

We first examine the relationship between the plasmid mixing fraction f_S and the average protein expression fraction $\langle f_P \rangle$. These experiments provide a first test of the simple linear model postulated in Eq. 3.7. The initial experiments are performed on the fluorescent proteins EGFP and EYFP as they will serve as the fluorescent markers of all subsequent fusion proteins included in this study. The plasmids pEGFP and pEYFP are mixed at specific mole fractions f_S. Each plasmid mixture is subsequently used in the transfection of CV-1 cells. For each population of cells transfected with a specific plasmid mixing fraction the fluorescence intensity of more than 20 cells was recorded in a dual-color setup. The protein expression fraction, $f_p = N_{EYFP} / (N_{EYFP}+N_{EGFP})$, was determined individually for each measured cell. Figure 3.1A shows the average protein expression fraction $\langle f_P \rangle$ versus the plasmid mixing fraction f_S. The data suggest a linear relationship between both fractions. A fit of the data to our proposed model (Eq. 3.9) reproduces the data with an efficiency ratio of $y = 1.04$. An efficiency ratio close to one is expected because each of the two plasmids contains the same promoter region and the genetic sequence and structure of each protein is nearly identical.

We further test our model using fusion proteins. For the initial experiments we chose the ligand binding domain of the retinoid X receptor protein (RXRLBD) and label it with either EGFP or EYFP. The plasmids pEGFP–RXRLBD and pEYFP–RXRLBD, which essentially have identical sequences, are mixed at specific mole fractions, and the average protein expression fractions are calculated from the intensity

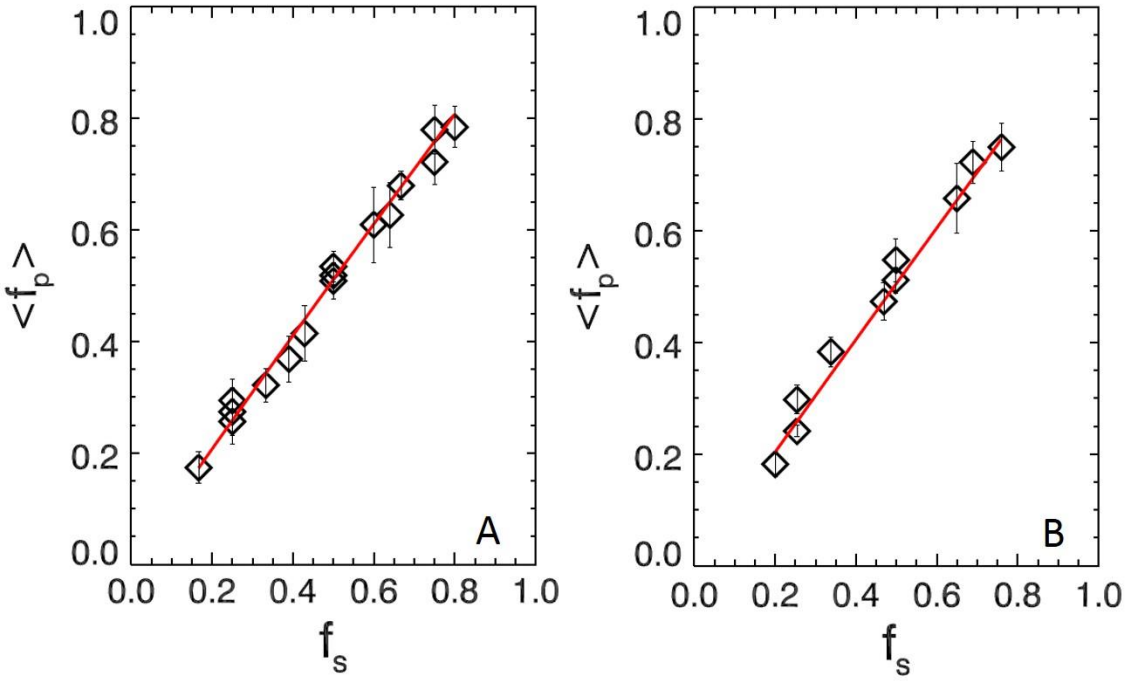

Figure 3.1 Relative protein expression for two similar proteins. Average protein expression fraction $\langle f_P \rangle = N_{P1} / (N_{P1} + N_{P2})$ as a function of the plasmid mole fraction $f_S = \upsilon_{p1} / (\upsilon_{p1} + \upsilon_{p2})$. Each data point represents the average of the expression fraction from 20-40 cells. (*A*) Data from cells expressing EYFP and EGFP with *P1 = EYFP*, *P2 = EGFP*, *p1 = pEYFP*, *p2 = pEGFP*. The fit recovered an efficiency ratio of 1.08. (*B*) Data from cells expressing RXRLBD-EYFP and RXRLBD-EGFP with *P1 = RXRLBD-EYFP*, *P2 = RXRLBD-EGFP*, *p1 = pRXRLBD-EYFP*, *p2 = pRXRLBD-EGFP*. The fit of the model recovered an efficiency ratio of 1.03

fractions of more than 20 cells. Figure 3.1B shows the results for the average protein versus plasmid fraction. The data again suggest a linear relationship and a fit to our model (Eq. 3.9) yields an efficiency fraction of 1.02, which confirms that both proteins have nearly identical expression efficiencies.

We now examine two proteins that differ substantially in their sequence. In this case we still expect the relationship between pDNA mixing and protein expression to be given by Eq. 3.9, but with an efficiency ratio that may be different from one. We experimentally test this hypothesis by expressing the proteins EGFP and RXRLBD-EYFP. As in the previous experiments, plasmids for each protein are mixed at specific mole fractions and the average protein expression fraction is calculated from a sample of more than 20 cells. Figure 3.2A shows the average protein expression fraction versus plasmid mixing fraction for this EGFP and RXRLBD-EYFP protein pair. The expressed protein fraction varies nonlinearly with plasmid fraction, which indicates an efficiency ratio of $y \neq 1$. A fit of the data by Eq. 3.9 determines $y = 0.22$. We repeated the experiment for a second protein pair by expressing EGFP and RARLBD-EYFP (retinoic acid receptor). Again, we observe a nonlinear relationship between the protein and plasmid fraction (Figure 3.2B). Fitting the data to Eq. 3.9 yields $y = 0.19$.

The insets in Figure 2 show protein and plasmid ratios instead of fractions to highlight the underlying linear relationship postulated in Eq. 3.7. The average protein ratio versus the plasmid mixing ratio for each protein pair is given together with a solid line representing Eq. 3.7 with the previously fit y values as the linear scaling factor. From the insets in Figure. 3.2, one can directly see that the slope (y) is less than 1 for the

dissimilar protein pairs; consequently, the relationship between protein and plasmid fractions in the main plot is non-linear. The protein fraction plots of Figures. 3.1 and 3.2 are constrained by the fractional endpoints $f_S = f_P = 0$ and $f_S = f_P = 1$. Only $y = 1$ results in a linear graph with a slope of 1 (Figure 3.1). For $y < 1$, the protein represented in the numerator is less easily expressed compared to the other protein such that large changes in the plasmid mixture are necessary to produce small changes in the expressed protein level. Consequently, this leads to an initial linear region of the data with a slope less than one followed by a region of increasing slope as we approach the endpoint $f_S = f_P = 1$, which results in a positive curvature of the data. In contrast, for $y > 1$, the protein represented in the numerator is more easily expressed compared to the other protein; this introduces a negative curvature in a plot of f_P versus f_S with a slope initially greater than one, which decreases as we approach the endpoint $f_S = f_P = 1$. A fit of the data to Eq. 3.9 determines y by taking these changes in slope and curvature into account.

Additionally, we investigated the influence of label selection on the relationship between the plasmid mixing fraction f_S and the average protein expression fraction $\langle f_P \rangle$ by repeating the measurement of the EGFP / RXRLBD-EYFP pair with switched labels (EYFP / RXRLBD-EGFP). The protein expression fraction, $f_p = N_{RXRLBD\text{-}EGFP} / (N_{EYFP}+N_{RXRLBD\text{-}EGFP})$ was determined individually for each measured cell. Figure 3.2C shows the average protein expression fraction versus plasmid mixing fraction

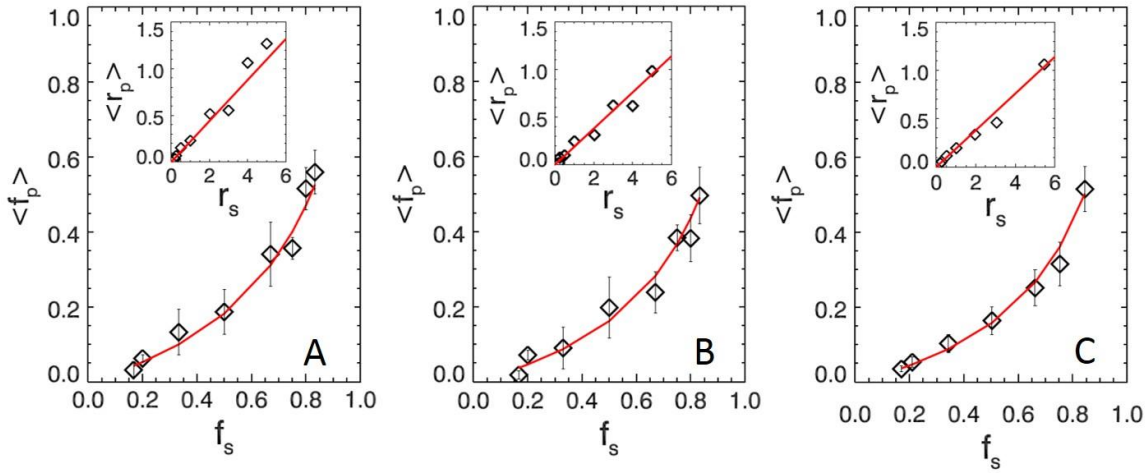

Figure 3.2 Relative protein expression for two dissimilar proteins. Average protein expression fraction $\langle f_P \rangle = N_{P1} / (N_{P1} + N_{P2})$ as a function of the plasmid mole fraction $f_S = \upsilon_{p1} / (\upsilon_{p1} + \upsilon_{p2})$. Each data point represents the average of the expression fraction from 20-40 cells. (*A*) Data from cells expressing RXRLBD-EYFP and EGFP with *P1 = RXRLBD-EYFP*, *P2 = EGFP*, *p1 = pRXRLBD-EYFP*, *p2 = pEGFP*. (*B*) Data from cells expressing RARLBD-EYFP and EGFP with *P1 = RARLBD-EYFP*, *P2 = EGFP*, *p1 = pRARLBD-EYFP*, *p2 = pEGFP*. The fit recovered expression efficiency ratios of $y = 0.22$ and $y = 0.19$ for (*A*) and (*B*) respectively. (*C*) Data from cells expressing RXRLBD-EGFP and EYFP with *P1 = RXRLBD-EGFP*, *P2 = EYFP*, *p1 = pRXRLBD-EGFP*, *p2 = pEYFP* with an expression efficiency ratio of y=0.19. The *insets* show the average protein ratio versus the plasmid mixing ratio for each protein pair with the solid line representing Eq. 3.7 using the fitted efficiency ratio.

for EYFP and RXRLBD-EGFP. A fit of the data by Eq. 3.9 determines an efficiency fraction, y = 0.19. Note, the data are plotted with the x-axis corresponding to a protein fraction $f_p = N_{RXRLBD\text{-}EGFP} / (N_{EYFP}+N_{RXRLBD\text{-}EGFP})$; plots previously shown all have the EYFP labeled protein in the numerator of the expression fraction. The fit of the data determined y = 0.22. The uncertainty in fitting the efficiency ratio y is estimated to be 0.04 for the data of Figures. 3.1 and 3.2. Since the efficiency ratios of both data sets (Figures 3.2A, C) differ by less than 0.04 we determine that swapping the protein labels has no significant effect on the experiment.

These results demonstrate that the simple linear model of Eq. 3.7 relating the average protein expression ratio to the pDNA mixing ratio is very successful in describing actual experiments. Note that the linear relationship between protein and plasmid ratios leads to a nonlinear relationship for the fractions (Eq. 3.9), if the efficiency ratio $y \neq 1$.

3.4.2 Variation in protein expression fractions

So far we have focused on the average behavior over a whole cell population. We now take a closer look at the variability from cell to cell. The distribution of the protein expression fractions from a population of cells is best represented by a histogram. Figure 3.3 shows the histograms of protein expression fractions f_p for cells transfected by a 1:1 pEYFP to pEGFP plasmid ratio. The histogram contains protein expression fraction from 120 cells with a bin resolution of 0.05. The y-axis represents the experimental probability $p(f_p)$ of observing the expression fraction f_p and is

normalized by dividing the number of cells $N\left(f_p\right)$ with protein expression fraction f_p by the total number of cells sampled. Thus, the histogram directly reflects the experimentally determined probability distribution function (pdf) of the protein expression fraction $\mathrm{pdf}_P\left(f_p\right)$. The data are plotted such that a protein fraction of 0 represents a cell expressing only EGFP and a value of 1 represents a cell expressing only EYFP. The experimentally measured distribution (*solid line*) of Figure 3.3 is approximately symmetric with respect to its peak at $f_p = 0.5$. These properties of the distribution agree with the expectations for a 50% / 50% plasmid ratio with an efficiency ratio of $y = 1$.

As pointed out in Eq. 3.10, the probability distribution of the protein fraction $\mathrm{pdf}_P(f_P)$ is related to the probability distribution function of the active plasmid fraction $\mathrm{pdf}_A(f_A)$ inside the cell. For the special case of $y = 1$, the relationship simplifies to $\mathrm{pdf}_A(f_A) = \mathrm{pdf}_P(f_P)$. In other words, the histogram of Figure 3.3 also represents the probability distribution of the active plasmid fraction. Because uptake and activation of a plasmid does not depend on whether it is an EGFP or EYFP plasmid, the probability p_y that a given active plasmid encodes EYFP is expected to be the same as the fraction f_S of EYFP-encoding plasmid in solution, $p_y \approx f_S$.

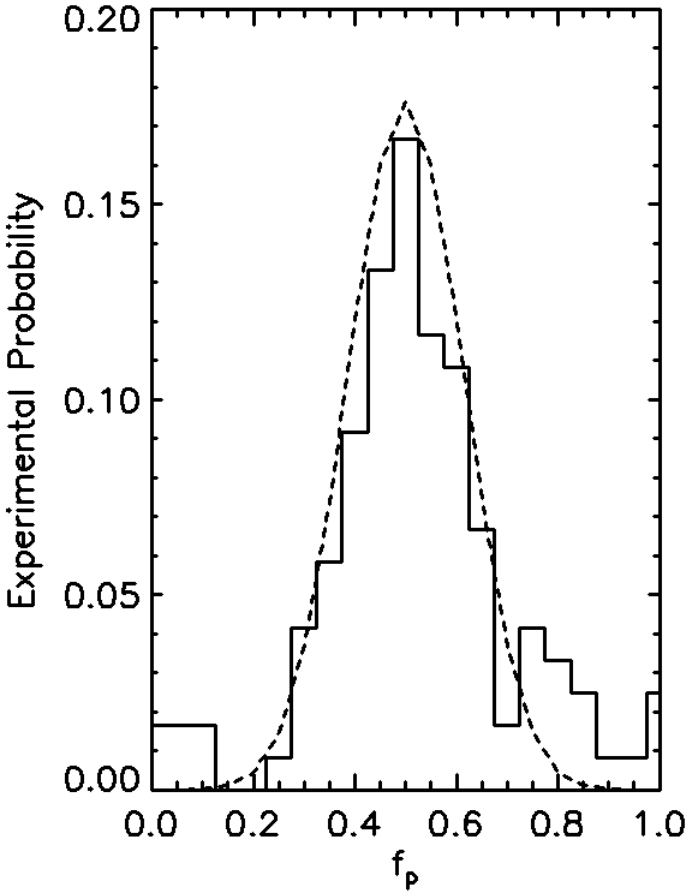

Figure 3.3 Protein fraction distribution for a 1:1 mixture.

Histogram of protein fractions (*solid line*) for EGFP and EYFP transfected by a 1:1 pEGFP / pEYFP mixture. The y-axis represents the number of cells with a protein expression fraction f_P normalized by the number of cells sampled. A protein fraction of 0 indicates a cell expressing only EGFP and a value of 1 represents a cell expressing only EYFP. The distribution is peaked at a protein expression fraction of 0.5 as expected for a 1:1 plasmid ratio. Binomial probability distribution (*dashed curve*) is for M = 20 active plasmids and $p_y = 0.5$.

We now introduce a basic statistical model to describe the distribution of active plasmids. Consider a cell with a total of *M* active plasmids. The probability that M_y of the *M* active plasmids are EYFP plasmids is described by a binomial distribution,

$$P_B\left(M_y, M, p_y\right) = \binom{M}{M_y} p_y^{M_y}\left(1 - p_y\right)^{M - M_y} \tag{3.12}$$

Let us assume that all cells of the population have *M* active plasmids. The active plasmid fraction f_A of a given cell is given by $f_A = M_y / M$. Rewriting of Eq. 3.12 results in a distribution describing the probability distribution of the active plasmid fraction,

$$\mathrm{pdf}_A\left(f_A, M, p_y\right) = P_B\left(M \cdot f_A, M, p_y\right). \tag{3.13}$$

Our model predicts that the probability distribution of the active plasmid fraction follows a binomial distribution. The dashed curve in Figure 3.3 represents a binomial distribution with *M* = 20 and $p_y = 0.5$. The distribution accurately represents the central peak of the data assuming 20 active plasmids per cell with a 50% probability p_y of a given plasmid being pEYFP. This probability matches well with the EYFP plasmid fraction in solution, $f_S = 0.5$. Although the binomial distribution fails to reproduce the tails of the experimental distribution, which are more strongly populated than expected by our model, the binomial distribution provides a reasonable model to estimate the variability of the protein expression ratios, since the population of the tails is sparse. For example, the standard deviation of the experimental protein expression fraction of Figure 3.3 is 0.12, while the binomial distribution leads to a standard deviation of 0.11.

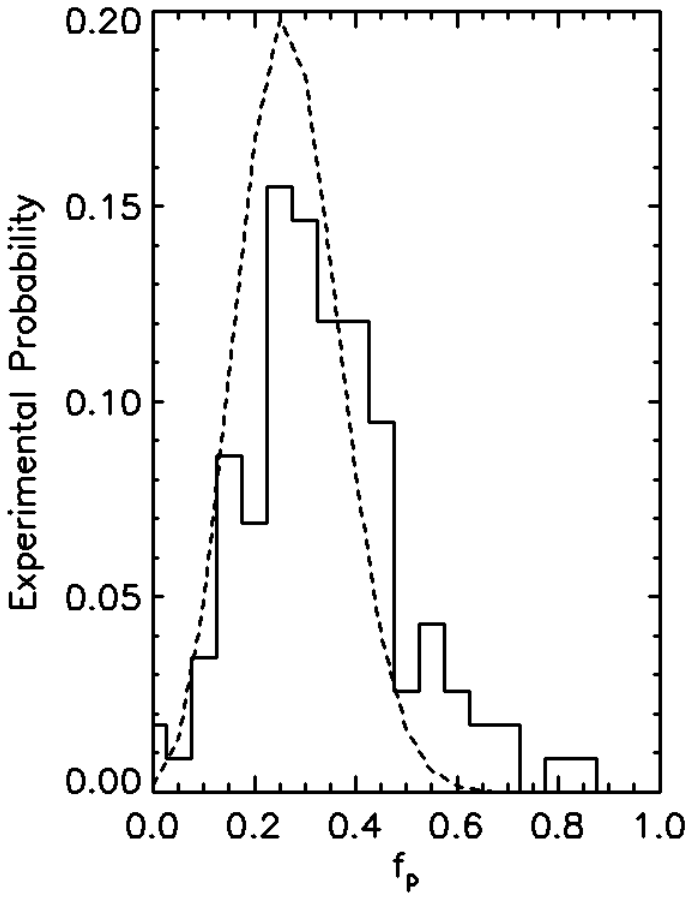

Figure 3.4 Protein fraction distribution for a 3:1 mixture.

Histogram of protein fractions (*solid line*) for EGFP and EYFP transfected by a 3:1 pEGFP / pEYFP mixture. The y-axis represents the number of cells with a protein expression fraction f_P normalized by the number of cells sampled. A protein fraction of 0 represents a cell expressing only EGFP and a value of 1 represents a cell expressing only EYFP. The binomial probability distribution (*dashed curve*) is for M = 20 active plasmids with p_y=0.27.

We now investigate the distribution function for a plasmid mixing ratio that differs from the symmetric 1:1 ratio used above. Cells were transfected with a 1:3 pEYFP to pEGFP plasmid ratio and the protein expression fraction was determined from 115 cells. The pdf of the protein expression fractions f_p is shown in Figure 3.4. The distribution is asymmetric with a peak shifted to $f_p = 0.25$. The dashed curve in Figure 3.4 represents a binomial distribution $P_B\left(f_p, M, p_y\right)$ with $M = 20$ and $p_y = 0.27$. Again, the binomial distribution approximately describes the central peak of the distribution, but fails to reproduce the tail of the distribution. The probability for an EYFP-plasmid $p_y = 0.27$ is in good agreement with the 1:3 pEYFP to pEGFP plasmid ratio ($p_S = 0.25$). Our modeling assumed that the number of active plasmids per cell is a constant ($M = 20$), which is unrealistic. The number of active plasmids is expected to be distributed, which needs to be accounted for in a refined model. We will return to this point later in the discussion section.

3.4.3 Application of model to FFS bright and dark experiment

The above experiments relied on two distinctly colored fluorescent proteins to develop a model describing the statistics of the protein expression fraction from a population of transfected cells. We now apply this model to an FFS study where two proteins are expressed, but only one of the two protein species is labeled. This bright and dark experiment provides a promising approach for identifying the presence of adverse label effects. To illustrate, let us consider the ideal case where the fluorescent label has no influence on protein assembly. In this case, we expect a specific reduction in the

measured brightness, because the dark protein is not visible, but competes with labeled protein in the formation of complexes. For example, an *n*-meric protein complex with a fraction f_P of labeled proteins and a corresponding fraction $f_{PD} = (1 - f_P)$ of unlabeled proteins leads to a normalized brightness of (89)

$$b = n - f_{PD}(n-1). \tag{3.14}$$

The normalized brightness, $b = \lambda / \lambda_{EGFP}$, as defined in Cchapter 2, is the ratio between the measured brightness λ of the complex and the brightness λ_{EGFP} of the label EGFP, and reflects the oligomerization state of a homo-protein complex (3). This property yields a normalized brightness of *n* for an *n*-meric complex if all proteins are labeled. Introducing dark proteins reduces the brightness to a value that depends only on the fraction of unlabeled protein. Although the exact value of the unlabeled protein fraction f_{PD} is unknown to us, the model of protein coexpression fractions introduced earlier allows us to predict the distribution and average normalized brightness from a bright and dark experiment. For example, we expect according to Eq. 3.14 an average normalized brightness of

$$\langle b \rangle = n - \langle f_{PD} \rangle (n-1). \tag{3.15}$$

The coexpression model (Eq. 3.9) relates the average protein fraction $\langle f_{PD} \rangle$ to the fraction of plasmids encoding the dark protein f_S .We test this relationship by conducting an FFS bright and dark experiment on the homo-dimeric protein Endophilin A2.

First, we conduct FFS measurements in the cytoplasm of cells expressing EGFP and the tandem-dimer $EGFP_2$ as a control experiment to confirm brightness doubling

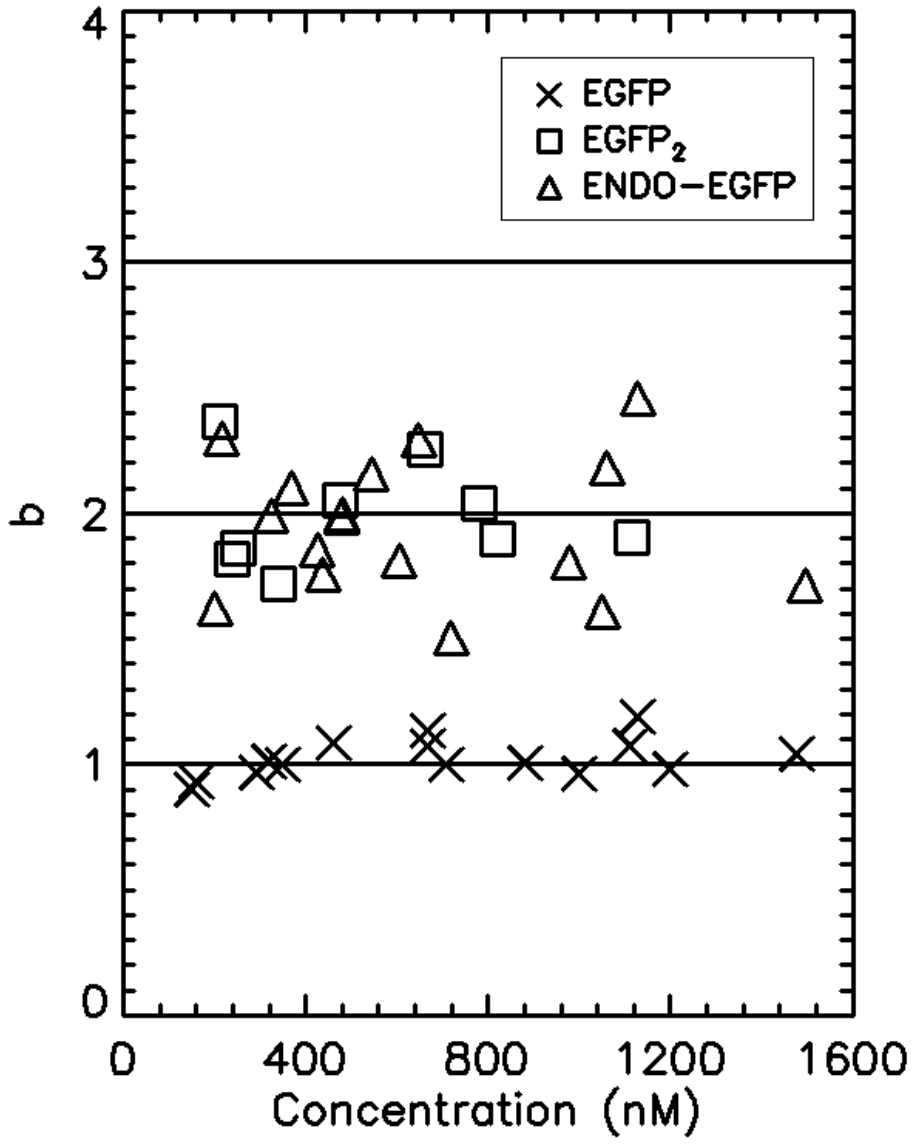

Figure 3.5 Normalized brightness of Endo-EGFP.

The normalized brightness of Endo-EGFP is nearly identical to $EGFP_2$ which suggests that Endo-EGFP forms a tight dimer over the concentration range studied. The average normalized brightness for $EGFP_2$ is 1.99±0.03 and the average normalized brightness for Endo-EGFP is 1.95±0.04.

(1, 2). The normalized brightness as a function of protein concentration shown in Figure 3.5 yields an average normalized brightness of 1.99±0.03 for $EGFP_2$ (2). In addition, we measured the brightness of EGFP labeled Endophilin A2 (Endo-EGFP) as a function of protein concentration (Figure 3.5). Our data with an average normalized brightness of 1.95±0.04 confirm the dimeric state of cellular Endophilin A2 as recently shown by Ross et al. (90). After establishing the dimeric nature of Endophilin A2, a bright and dark experiment with a 50% / 50% mole ratio of unlabeled (pEndo) and labeled (pEndo-EGFP) protein is performed. The normalized brightness values from 120 cells were measured and are plotted in Figure 3.6 as a histogram with a bin resolution of 0.1. The average normalized brightness of the population of cells measurement is $\langle b \rangle = 1.51$. This drop in brightness indicates according to Eq. 3.15 an average fraction for the expressed dark protein of $\langle f_{PD} \rangle = 0.5$, which is identical to the fraction of plasmids encoding the dark protein, $f_S = \langle f_{PD} \rangle = 0.5$. This result further implies that the expression efficiency ratio *y* is one according to Eq. 3.9. Thus, our data demonstrate that quantitative interpretation of the average brightness from bright and dark experiments provides a measure of the efficiency ratio *y*. Extending this study to other values of the dark protein-encoding plasmid fraction would provide independent measurements of the efficiency ratio *y*. A systematic inconsistency in the recovered *y* values would be indicative of interference by the label.

We now turn to the distribution of the measured brightness values. According to Eq. 3.11 the brightness is determined by, $b = n - f_{AD}(n-1)$, where f_{AD} is the active plasmid fraction encoding dark protein. For a dimer this reduces to $b = 1 + f_A$, where f_A,

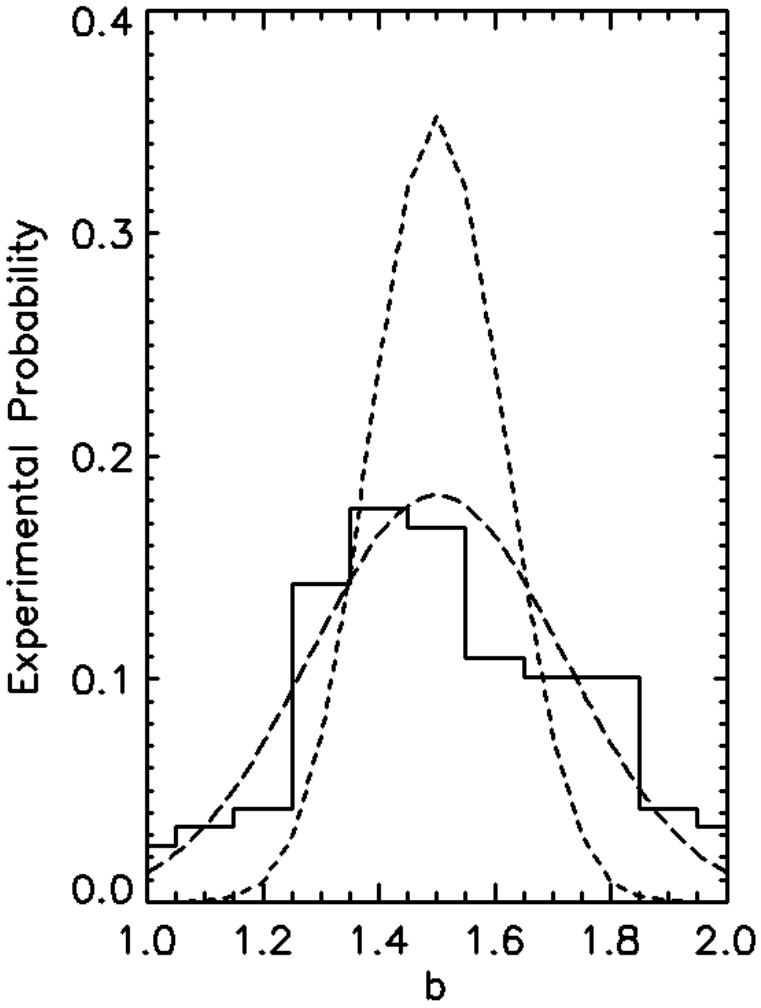

Figure 3.6 Bright and dark brightness distribution.

Histogram of the normalized brightness from cells transfected with a 1:1 pEndo-EGFP / pEndo mixture. The histogram (*solid line*) contains the normalized brightness from 120 cells with a bin resolution of 0.1. (*short dashed line*) A binomial distribution for $M = 20$ active plasmids. (*long dashed line*) The convolution of a binomial distribution for $M = 20$ active plasmids with a Gaussian distribution with a standard deviation of 0.19. .

the labeled active plasmid fraction, is related to f_{AD} by $f_A = (1 - f_{AD})$. This relationship relates the brightness to the active plasmid distributions, $\mathrm{pdf}(b) = \mathrm{pdf}_A(b-1)$. Straightforward application of our binomial model (Eq. 3.13) with M = 20 active plasmids and $p_{PD} = f_S$ = 0.5 fails to reproduce the measured brightness distribution (short dashed line in Figure 3.6). We need to account for the inherent uncertainty of measuring a brightness value inside cells. The standard deviation in brightness calculated from the data in Figure 3.5 is 10% for EGFP and $EGFP_2$ and 13% for Endo-EGFP. Thus, we convolute the binomial distribution with a Gaussian distribution representing a relative uncertainty of 13% with respect to the mean brightness of 1.5. The convoluted distribution (*long dashed line* in Figure 3.6) provides a good approximation of the experimental brightness distribution. Thus, dark experiments contain two significant sources of noise, the inherent uncertainty of the brightness measurement and the variations in the dark protein fraction. Both noise sources are independent and their standard deviations add up as $\sigma = \sqrt{\sigma_1^2 + \sigma_2^2}$. A 13% uncertainty in the brightness measurement ($\sigma_1 = 0.19$) and the uncertainty due to the active plasmid fraction ($\sigma_2 = 0.11$) leads to σ = 0.22, which is in good agreement with the standard deviation of 0.25 of the experimental data.

3.5 Discussion

It is well known that the protein expression level from transient transfection varies widely from cell to cell. Despite this seemingly random behavior of the absolute

expression level, the protein expression ratio of two simultaneously transfected proteins is surprisingly well-behaved. We developed a simple model for the average protein expression ratio, its variance, and distribution function. The core of the model is based on the assumption that the vast majority of cellular factors influencing gene expression affect both plasmids in the same way. Thus, these common factors cancel in the ratio of the protein expression, and the only two factors remaining are the expression efficiency ratio y and the active plasmid ratio r_A. Neither of these factors are known a priori, but over a whole cell population, the mean of r_A equals the ratio r_S of plasmids in the transfection solution, $\langle r_A \rangle = r_S$. This statement provides a testable hypothesis in the form of Eqs. 3.7 and 3.9, because it relates the average protein expression ratio $\langle r_P \rangle$ to the plasmid ratio r_S with y as the only unknown. We tested this relation by experiment and found that the data agree with the hypothesis. Fitting of the data provides the efficiency ratio y. Further, we describe the cell to cell variation in the expression fraction f_P through the introduction of a distribution model of the active plasmid fraction. This was based on a binomial distribution with a total of M active plasmids from both sources, $pDNA_1$ and $pDNA_2$. Clearly, assuming that each cell has a fixed number M of active plasmids is unrealistic. This number is expected to be distributed. In this sense, the value of $M = 20$ used in this study represents an approximation for the mean number of active plasmids.

Despite the simple nature of the model, it very closely approximates the experimental data. This descriptive power of the model should be useful for predicting the feasibility and outcome of many coexpression fluorescence experiments. Our data

demonstrate that the mean protein expression ratio can be adjusted in a controlled and predictable fashion by changing the plasmid ratio. This degree of control is useful for selecting conditions that optimize the detection of protein-protein interactions. For example, if one protein expresses much less than the other, this imbalance can be corrected for by adjusting the molar plasmid ratio accordingly. This control over protein coexpression is limited by the finite number of active plasmids present in each cell. The binomial distribution model with M = 20 plasmids describes the spread in the experimental data which corresponds to ~10 active copies for each type of plasmid in a 1:1 transfection mixture. In trials where pEGFP and pEYFP are mixed at ratios of 1:13 and 1:27, the expressed protein distribution is skewed to be almost entirely EYFP (data not shown). Thus, once protein expression ratios need to be modified by a factor of more than 10, adjusting the pDNA ratio will not produce the desired outcome. This effect was encountered in a study where the large difference in expression efficiency prevented the use of the full-length coactivator SRC-1 (91). The binomial distribution model should be tested for each specific cell line and transfection method used in a study to establish the number of active plasmids, because its value determines the accessible range of expression ratios.

The binomial distribution model is further useful for fluorescence experiments, because it imposes limits on the cell to cell variations in brightness values and FRET efficiencies due to different expression ratios. This model predicts the spread in the experimental data and provides a quantitative estimate of the standard deviation of the measured signal. Our experimental data show that a few cells do deviate significantly

from the binomial distribution model (Figure 3.3). Thus, it is expected that fluorescence experiments on cells will produce a few measurement values that differ substantially from the bulk of the values. However, because the majority of the cells follow the binomial distribution model, the experimental standard deviation is not significantly affected by the few outliers.

We applied the cotransfection model to a bright and dark experiment on endophilin A2. The cotransfection model provides a quantitative explanation for the drop in the average brightness. The model further explains the increased scatter in brightness due to variations in the expression ratio. These results demonstrate that quantitative interpretation of FFS bright and dark experiment is feasible once the statistics of coexpression is known. A previous study employed the concept of the bright and dark experiment to check for a labeling effect in the Gag copy number of HIV virus-like particles (72). Brightness measurements of virus-like particles containing labeled and unlabeled Gag demonstrated that the fluorescent label did not interfere with the particle assembly process. However, the analysis was based on the assumption that the plasmid ratio is proportional to the expression ratio of labeled and unlabeled Gag. The work presented here justifies this assumption and provides a solid foundation for future bright and dark experiments.

It is remarkable that the outcome of a complicated process like transient cotransfection is captured by a model that omits the details of the transfection process. In the following we examine the details of cationic lipid mediated transfection and their influence on the data. Cationic lipids interact with pDNA to form spontaneous complexes

called lipoplexes through electrostatic interactions. The overall positive charge of the lipoplex aids in the endocytotic uptake by the cell (92–95). In order for transcription to occur the lipoplex must escape the endosome and the pDNA must disassociate from the lipid en route to or inside the nucleus. The number of lipoplexes involved in the dissociation process, the nature of the dissociation process, and the entry into the nucleus are not yet understood. For example, although there is evidence that pDNA fully dissociates from the cationic lipid upon exiting the endosome, there are also conflicting observations (92, 96–99). We are able to use the statistics of expression fractions to contribute to the understanding of some of these details.

Kriess et al. reported that a single lipoplex contains ~37.5 kbase of pDNA (100). Since the EGFP and EYFP plasmids are 4.5 kbase in length, we estimate that in our study a single lipoplex contains ~8 plasmids. Using this as the average number of plasmids per lipoplex, the complete uncoating of two to three lipoplexes is sufficient to provide ~20 active plasmids as currently required by our model. Thus, we predict that the number of lipoplexes contributing to protein expression is very small. Since both the number of plasmids per lipoplex and the number of uncoating events are likely distributed, some cells will only experience the uncoating of a single lipoplex. If this lipoplex contains a small number of plasmids, then the probability that they all encode the same protein is much higher than for the bulk of $M = 20$ active plasmids. This scenario provides a plausible explanation for the highly populated tails of the distribution in Figure 3.3.

We now test this hypothesis by altering the transfection protocol. So far, our studies involved lipoplexes carrying a statistical mix of two plasmids, but now we switch

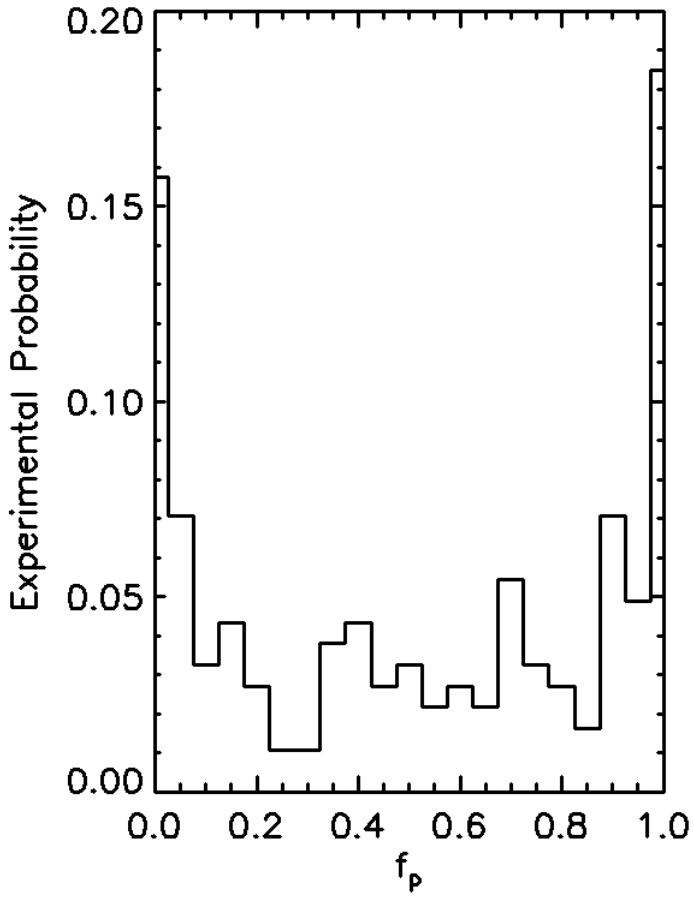

Figure 3.7 Distribution of protein fractions from a binary transfection.

Histogram of protein fractions for EGFP and EYFP transfected by a 1:1 lipoplex (pEGFP) / lipoplex (pEYFP) mixture. The histogram representing the probability distribution contains protein expression fraction from 140 cells with a bin resolution of 0.05. The y-axis represents the number of cells with a protein expression fraction f_P normalized by the number of cells sampled. A protein fraction of 0 represents a cell expressing only EGFP and a value of 1 represents a cell expressing only EYFP.

to a mix of two types of lipoplexes where each type carries the same plasmid. Lipoplexes that carry pEGFP are denoted as pEGFP-lipolexes, while lipoplexes carrying pEYFP are labeled as pEYFP-lipoplexes. In this binary transfection method, we transfected cells with a solution containing a 1:1 molar ratio of pEGFP-lipoplexes to pEYFP-lipoplexes. The distribution of protein expression fractions of this experiment (Figure 3.7) is distinctly different from Figure 3.3. If many lipoplexes are uncoated, the chance that all active plasmids are of the same type is vanishingly small. Such events contribute exclusively to the center of the distribution, which is not representative of the experimental data. On the other hand, the uncoating of a single lipoplex leads to cells expressing only EGFP or EYFP which populate the tails of the distribution ($f_P = 0$ and $f_P = 1$). While this model reproduces the tails of the experimental data, we also need to include the uncoating of two to a few lipoplexes in order to account for the middle of the distribution representing the expression of both proteins. Thus, our experiment convincingly demonstrates that very few lipoplexes contribute to protein expression. This discussion provides some additional insight. First, because although the total amount of pDNA (active and inactive forms) present in a transfected cell is very high (87, 88, 101), the dissociation of active plasmid from the complex is a very rare event. Second, our cotransfection model, although it does not account for the existence of lipoplexes, is adequate provided plasmids are mixed together before adding the lipid reagent.

Our model provides a novel quantitative characterization of the average and standard deviation of protein coexpression ratios within living cells. With such a model, it is now possible to predict and control relative protein expression through manipulation

of pDNA ratios prior to transfection, which is of interest for fluorescence studies of protein-protein interactions and for FFS bright and dark experiments. The distribution model also provides a prediction for variations in the fluorescence signal due to different expression ratios. Additional studies using different cell lines and other transfection protocols will be needed to test the robustness and generality of our findings. It is worthwhile to again point out that all the plasmids of this study use the same promoter. It would be interesting to repeat the study for plasmids with different promoters and check if the model still applies by using a modified expression efficiency ratio. Nevertheless, the model of expression fractions established in this chapter provides insight into the cationic lipid mediated transfection process and should serve as a quantitative platform for future studies of protein coexpression and fluorescence applications in cells.

4. Quantifying Protein-Protein Interactions of Peripheral Membrane Proteins with z-scan FFS

In this chapter we apply z-scan FFS to quantify the brightness of peripherial membrane proteins in the cytoplasm and at the plasma membrane. Fluorescently labeled proteins that are found both in the cytoplasm and at the plasma membrane, such as peripheral membrane proteins, create stratified fluorescent layers that present a challenging environment for brightness studies with FFS. The geometry of each layer along with fluorescence and brightness contributions from adjacent layers generates a convoluted raw brightness that conceals the underlying brightness of each individual layer. Because the brightness at a layer establishes the oligomeric state of the fluorescently labeled protein at said layer, we developed a method that connects the experimental raw brightness with the physical brightness at each layered compartment. The technique determines the oligomerization in each compartment from an axial intensity scan through the sample, followed by an FFS measurement at each layer. We experimentally verify the technique with H-Ras-EGFP as a model system and determine its oligomeric state at both the plasma membrane and in the cytoplasm. Furthermore, we study the oligomerization of the Gag matrix domain of Human T-lymphotropic virus Type 1. The matrix domain targets the Gag polyprotein to the plasma membrane where subsequently viral assembly occurs. We determine the oligomerization of matrix in the cytoplasm and observe the onset of protein-protein interactions at the membrane. These observations shed light on the early assembly steps of the retrovirus.

4.1 Introduction

Peripheral or extrinsic membrane proteins associate temporarily with the membrane to perform a variety of cellular processes including signal transduction, cytoskeletal membrane interactions, membrane trafficking and enzymatic activities like phospholipid metabolism and catabolism. Membrane association and dissociation of peripheral membrane proteins provide a mechanism for triggered conformational changes that serve to regulate protein-protein interactions and biological activity (8–10, 102, 103). This work introduces a method based on FFS to study the oligomeric state of peripheral membrane proteins that reside in the cytoplasm and at the plasma membrane. FFS techniques like FCS (56, 57, 104) and brightness analysis of fluctuations (60–62) have been successfully used to study protein behavior both at the membrane and in the cytoplasm of living cells (1–3, 43, 44, 47, 65, 105). Here, we focus on the use of brightness analysis for studying the interactions of peripheral membrane proteins that reside concurrently in the cytoplasm and at the plasma membrane.

Because peripheral membrane proteins associate reversibly with the membrane, they often exist in two pools: a membrane-bound form and a free soluble form in the cytoplasm. This leads to three distinct layers in a cell adherent to a coverslip (see Figure 4.1A). The first layer consists of the basal or bottom plasma membrane in contact with the glass. The second layer is the cytoplasmic compartment, followed by the apical or top membrane as the last layer. The axial extent of the optical excitation is much larger than the thickness of the membrane which ensures coexcitation of proteins in the membrane-bound and cytoplasmic pools. The fluorescence fluctuation contributions from both

sources need to be disentangled to reliably identify the brightness and oligomeric state of proteins at the membrane and in the cytoplasm.

Z-scan FFS provides a method for untangling the fluorescence contributions of a multi-layered protein system, and allows the brightness of the sample at each layer to be established. The technique was previously introduced to properly account for fluorescence fluctuations in thin cytoplasmic sections (76) and is based off earlier work on z-scan FCS by Hof and coworkers (46). This study extends the theory of z-scan FFS to multiple strata, converts the theoretical concepts into a measurement strategy, and applies z-scan FFS to peripheral membrane proteins. We investigate the protein H-Ras as a model system and determine its oligomeric state at the plasma membrane and in the cytosol.

The Gag polyprotein plays a pivotal role in the assembly and release of retroviruses (106). Recent studies indicated fundamental differences between the early assembly events of two retroviruses, human T-cell leukemia virus type 1 (HTLV-1) and human immunodeficiency virus type 1 (HIV-1) (107, 108). While HIV-1 Gag requires the onset of cytoplasmic Gag-Gag interactions to promote translocation to the inner leaflet of the plasma membrane (109–111), HTLV-1 Gag appears to engage the plasma membrane as a monomer (108). Since the matrix (MA) domain of Gag is the primary driver of Gag association with the inner leaflet of the plasma membrane (112–116), this study investigates the peripheral membrane protein MA by z-scan FFS to shed light on the ability of HTLV-1 Gag to bind to the membrane as a monomer and to identify its oligomeric state at the membrane.

4.2 Material and methods

4.2.1 Experimental setup

Experiments were performed on a modified two-photon microscope, described in chapter 2. Measurements were taken with a Zeiss 63x C-Apochromat water immersion objective (N.A.=1.2) at an excitation wavelength of 1000 nm and an average power, after the objective, of 0.3 mW. The data was acquired at a frequency of 20 kHz for a duration of ~60 seconds. Photon counts were detected by an avalanche photodiode (APD, SPCM-AQ-141, Perkin-Elmer, Dumberry, Quebec), recorded by a Flex02-01D card (correlator.com, Bridgewater, NJ), and analyzed with programs written in IDL 8.2 (Research Systems, Boulder, CO). For dual-channel measurements, a dichroic mirror with a center wavelength of 580 nm split the fluorescence emission into two detection channels. The green channel had an additional 84-nm-wide bandpass filter centered at 510 nm (Semrock, Rochester, NY) to eliminate the reflected fluorescence of mCherry.

Z-scans were performed by using an arbitrary waveform generator (Model No. 33250A, Agilent Technologies, Santa Clara, CA) to move a PZ2000 piezo stage (ASI, Eugene, OR) along the z-axis. A triangular function with a peak-to-peak amplitude of 2.4 V and a period of 10 seconds was used for the z-scan experiments. This waveform corresponded to 24.1 μm of axial travel in 5 s with the cells occupying roughly 3-4 μm in the center of each pass. Data was acquired at a frequency of 20 kHz for either a few seconds for a single z-scan or over several minutes for sequential z-scans.

4.2.2 Sample preparation and plasmid construction

The pEGFP-C1 and pEGFP-N1 plasmids were purchased from Clontech (Clontech, Mountainview,CA). The mCherry-C1 plasmid was cloned from the mCherry pRSET B plasmid which was a kind gift from Dr. R. Y. Tsien (University of California, San Diego). mCherry was amplified by PCR with a 5' primer that encodes an NheI restriction site and a 3'primer that encodes an XhoI site. The PCR fragment of mCherry was then ligated into the backbone of pEGFP-C1 (Clontech, Mountainview,CA). The EGFP-H-Ras plasmids were a kind gift from Dr. Mark Phillips (New York University School of Medicine). The MA domain of both HIV-1 Gag and HTLV-1 Gag were cloned from their full Gag sequence and amplified by PCR with a 5' primer that encodes an *XhoI* restriction site and a 3' primer that encodes an *EcoRI* site. The HIV-1 MA and HTLV-1 MA cDNAs were then ligated into the pEGFP-N1 plasmid. All sequences were verified by automatic sequencing.

All studies were performed using transiently transfected U2OS cells that were obtained from ATCC (Manassas, VA) and maintained in 10% fetal bovine serum (Hycolone Laboratories, Logan, UT) and DMEM medium. Cells were subcultered in eight-well coverglass chamber slides (Nalge Nunc International, Rochester, NY) 12 hours before transfection. Transient transfections were carried out using TransFectin (BioRad, Hercules, CA), according the manufacturer's instructions, 24 hours prior to measurement. Immediately before measurement, the growth medium was replaced with Dulbecco's phosphate-buffered saline (PBS) with calcium and magnesium (Biowhittaker, Walkerville, MD).

4.2.3 Brightness calibration

The brightness from the FFS data was computed as detailed in section 2.3.3 (70, 117). In addition, calibration measurements of the brightness of EGFP were performed in the thick section of 10-20 cells expressing EGFP. The average brightness λ_{EGFP} from this calibration experiment served as the normalization factor to convert an experimentally measured brightness λ into a normalized brightness $b = \lambda / \lambda_{EGFP}$.

4.2.4 Z-scan calibration

A z-scan calibration procedure was carried out to determine specific parameters of the mGL-PSF as described by Macdonald et (76). A series of eight z-scans were performed on a cell expressing EGFP starting at the nucleus and moving to thinner sections of the cell. A collective fit of the z-scan intensity profiles using the PSF defined by Eq. 4.9 resulted in z_0 = 0.95 ± 0.1 μm and y = 1.95 ± 0.14 for a radial beam waist of w_0=0.47μm. These values are consistent with previously reported parameters (76) and will remain fixed for the remainder of the experiment.

4.2.5 Z-scan FFS procedure

In a three-layer protein system, an intensity trace is measured along the z-axis of the cell. A fit of the z-dependent intensity data provides the location for the point FFS measurements: the bottom membrane layer z_{BM}, the top membrane layer z_{TM}, and the midpoint of the cytoplasmic layer $z_{mid} = (z_{BM} + z_{TM})/2$. Point FFS measurements are

then performed by focusing the excitation PSF at z_{BM}, z_{TM} and z_{mid}. Movement of the cell or focus drift during the FFS measurements would compromise the result. We performed an intensity z-scan directly before and after the FFS measurement as a control. Changes in the intensity profile between the first and second z-scan indicate the presence of motion. We only accepted FFS data for brightness analysis when the intensity profiles agreed.

4.2.6 Z-scan data analysis

For all the z-scan experiments described within this thesis, the photon counts sampled at 20 kHz were rebinned by a factor of 80 by software, which corresponds to a z-scan sampling time of $T_z = 4$ ms. The z-scan speed $v_z = 4.82$ μm/s resulted in a step size $\Delta z = v_z T_z = 19.3$ nm between binned photon counts k_z. Fluorescence intensity was determined by $F(z) = k_z / T_z$. The experimental z-scan intensity profile $F(z)$ was analyzed in IDL 8.3 by least-squares fitting to a model intensity profile with a Levenberg–Marquardt algorithm, where the PSF parameters z_R and *y* were fixed to the calibrated values, and the standard deviation σ_{binned} of the binned photon counts was estimated from the standard deviation σ_k of the unbinned counts by $\sigma_{binned} = \sigma_k \sqrt{N_B}$, with $N_B = 80$ representing the number of samples in a single bin. The fit of the data to the delta-slab-delta model (Eq. 4.6) determined the position of the bottom and top

membrane (z_{BM} , z_{TM}) as well as the maximum fluorescence intensities of the bottom membrane, the top membrane, and the cytoplasm ($F_{BM,\max}$, $F_{TM,\max}$, $F_{Cyto,\max}$).

4.3 Results

4.3.1 Z-scan FFS of a single layer

Scanning the two-photon excitation spot uniformly along the z-axis of a cell (Figure 4.1B) results in a z-dependence of the fluorescence signal (Figure 4.1C). For a cell expressing a homogeneously distributed cytoplasmic protein like EGFP, the first two moments of the fluorescence intensity have been described previously in chapter 2 (Eq. 2.18) and by Macdonald et al. (76),

$$\begin{aligned} \left\langle F(z) \right\rangle &= \lambda \cdot \left\langle c \right\rangle \cdot V_1(z) \\ \left\langle \Delta F^2(z) \right\rangle &= \lambda^2 \left\langle c \right\rangle V_2(z) \end{aligned} \quad . \tag{4.1}$$

The fluorescence intensity $\left\langle F(z) \right\rangle$ and variance $\left\langle \Delta F^2(z) \right\rangle$ of the fluorescence depend on the cytoplasmic brightness λ and concentration $\left\langle c \right\rangle$ of the fluorescently labeled protein. The z-dependence is introduced by the generalized volume function $V_r(z) = \int PSF^r(\rho,\zeta) \cdot S(z+\zeta) \cdot 2\pi\rho \, d\rho \, d\zeta$, which depends on the point spread function (PSF) raised to the rth power and the sample shape factor *S*(*z*). The shape factor for a cytoplasmic protein is given by a slab geometry starting at the bottom plasma membrane (BM) and ending at the top plasma membrane (TM). If we mark the location of both membranes by z_{BM} and z_{TM} (Figure 4.1B), the shape factor of the cytoplasmic protein is described by a Boxcar function starting at z_{BM} and ending at z_{TM} ,

$$S_{Cyto}\left(z; z_{BM}, z_{TM}\right) = \begin{cases} 1, & z_{BM} < z < z_{TM} \\ 0, & \text{otherwise} \end{cases} . \qquad (4.2)$$

The fluorescence intensity profile $\langle F(z) \rangle$ for the slab geometry is depicted by the solid line in Figure 4.1C and reaches its peak at mid-height ($z_{mid} = (z_{BM} + z_{TM})/2$) of the slab, because the volume overlap between the point spread function and the sample is maximized.

The fluorescence brightness λ is determined from Mandel's Q-parameter (70, 71),

$$Q(z) = \frac{\langle \Delta F^2(z) \rangle}{\langle F(z) \rangle} . \qquad (4.3)$$

By inserting Eq. 4.1 we show that Q is the product of the brightness and a z-dependent gamma factor $\gamma_2(z) = V_2(z)/V_1(z)$ as described previously, $Q(z) = \gamma_2(z) \cdot \lambda$ (76). The z-dependent Q-parameter for the slab geometry is illustrated by the solid line in Figure 4.1D. This is an extension of conventional FFS, where the sample volume is considered to be infinite. Conventional FFS is characterized by a z-independent Q-parameter, $Q = \gamma_{2,\infty} \cdot \lambda$, where $\gamma_{2,\infty}$ specifies the conventional gamma-factor.

4.3.2 Z-scan FFS of multiple layers

The above equations have been successfully applied to a single geometric layer to determine the brightness of proteins in thin cytoplasmic sections and to identify their stoichiometry (76). In this chapter, we expand z-scan FFS to describe geometries comprised of several layers. A simple example of such a system is realized by a protein that resides both in the cytoplasm and at the plasma membrane. We expect that the

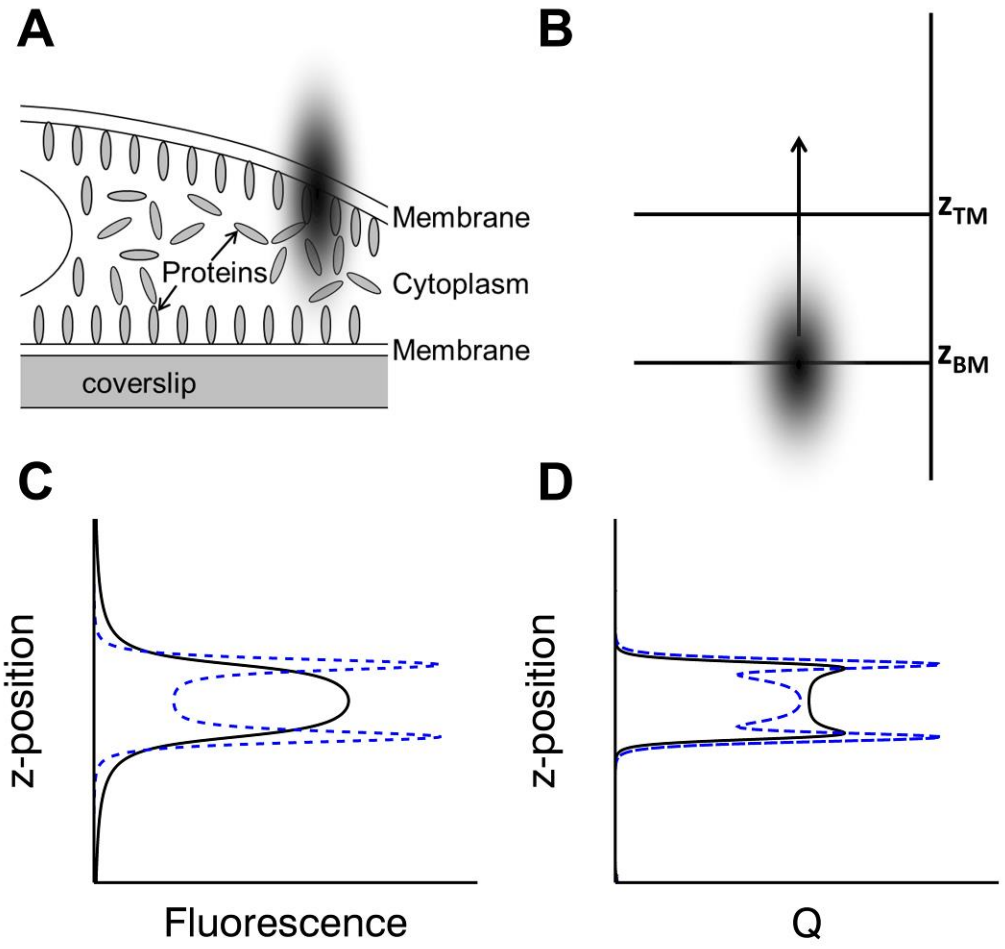

FIGURE 4.1 Concept of z-scan FFS.

(*A*) Three distinct cell layers: the bottom membrane, cytoplasm, and top membrane. The axial length of optical excitation (*solid oval*) leads to coexcitation of layers. (*B*) The slab model defines the geometry by specifying the location of the bottom and top membrane by z_{BM} and z_{TM}, respectively. The cytoplasmic layer extends from z_{BM} to z_{TM}. The two-photon excitation spot is scanned along the z axis. (*C*) Sketch of the average intensity for a cell expressing cytoplasmic EGFP (*solid line*) and a membrane bound-EGFP fusion protein (*dotted line*). (*D*) Q-parameter versus z position for the same parameters as panel C.

presence of the protein at the plasma membrane gives rise to two additional peaks in the intensity profile (*dotted line*, Figure 4.1C) and the Q-parameter profile (*dotted line*, Figure 4.1D), reflecting the contributions from fluorescent proteins at the bottom and top plasma membrane.

To treat membrane-bound proteins and other complex layered geometries requires a generalization of the theory beyond that given in the previous section. Since the first and second moment of the fluorescence intensity from multiple independent sources are additive, for a multi-layered sample the contributions from each layer are added up to give the total average fluorescence intensity and its variance as

$$\begin{aligned} \left\langle F(z) \right\rangle &= \sum_i \left\langle F_i(z) \right\rangle = \sum_i \lambda_i \cdot \left\langle c_i \right\rangle \cdot V_{1,i}(z) \\ \left\langle \Delta F^2(z) \right\rangle &= \sum_i \left\langle \Delta F_i^2(z) \right\rangle = \sum_i \lambda_i^2 \cdot \left\langle c_i \right\rangle \cdot V_{2,i}(z) \end{aligned} . \tag{4.4}$$

The *i*-th layer is described by its brightness λ_i, concentration $\left\langle c_i \right\rangle$ and shape factor $S_i(z)$, which make up the fluorescence intensity $\left\langle F_i(z) \right\rangle$ and variance $\left\langle \Delta F_i^2(z) \right\rangle$ of the layer as described in Eq. 4.1.

We are specifically interested in modeling proteins found concurrently at the plasma membrane and in the cytoplasm. This situation is best described by a three-layer system, which we refer to as a delta-slab-delta model, consisting of a bottom membrane (BM) located at z_{BM}, a cytoplasmic layer (Cyto), and a top membrane (TM) located at z_{TM}. Because a membrane is much thinner than the linear dimension of the PSF, its geometric shape factor is well approximated by a delta function. We refer to membranes

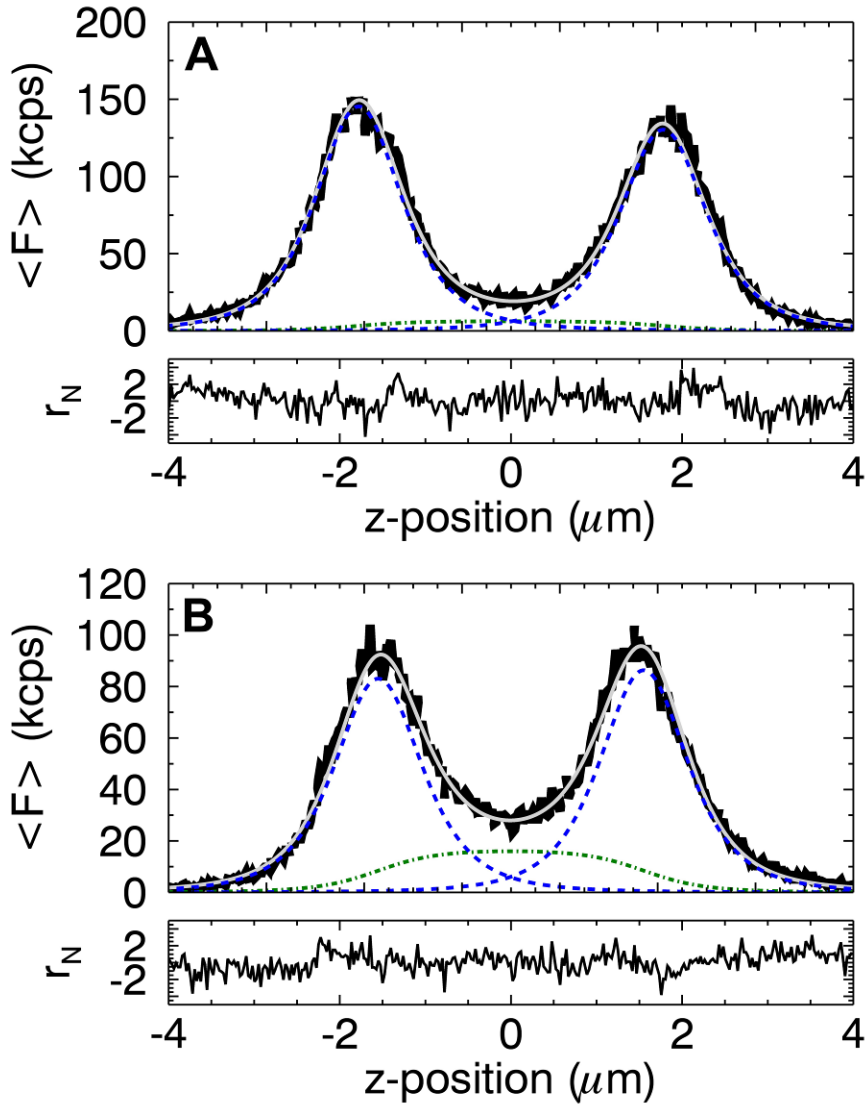

FIGURE 4.2 Z-dependent fluorescent intensity profile in kilo counts/s.

(*A*) The profile (*solid line*) from EGFP-H-Ras and its fit (*shaded line*) to Eq. 4.6 (reduced χ^2=1.4). (Dotted-dashed line) Contribution from the cytoplasmic (*slab*) layer; (*dotted lines*) contribution from the membrane (delta) layers. (*B*) The intensity profile (*solid line*) from the combined fluorescence of EGFP-H-Ras and mCherry and its fit (*shaded line*) to Eq. 4.6 (reduced χ^2=1.3). The increase in the cytoplasmic intensity (*dotted-dashed line*) stems from the addition of the mCherry signal.

as delta layers to contrast their geometry with that of the slab model used for the cytoplasm. Thus, the geometry is described by $S_{BM}(z) = \delta(z - z_{BM})$ for the bottom membrane layer, $S_{TM}(z) = \delta(z - z_{TM})$ for the top membrane layer, and $S_{Cyto}(z; z_{BM}, z_{TM})$ for the cytoplasmic layer.

The fluorescence intensity and fluctuations of a delta layer are still described by Eq. 4.1, but with a reinterpretation of some parameters. The volume concentration $\langle c \rangle$ is replaced by the surface concentration $\langle \sigma \rangle$ at the membrane and the generalized volume function $V_r(z)$ now represents an area function (76). These changes are a consequence of the delta-function and provide a rigorous interpretation of z-scan intensity parameters.

The z-dependence of the fluorescence intensity of the three-layer system is given by

$$\langle F(z) \rangle = \langle F_{BM}(z) \rangle + \langle F_{Cyto}(z) \rangle + \langle F_{TM}(z) \rangle . \tag{4.5}$$

For fitting purposes it is more convenient to express Eq. 4.5 as

$$\langle F(z) \rangle = F_{BM,\max} \tilde{v}_{BM}(z) + F_{Cyto,\max} \tilde{v}_{Cyto}(z) + F_{TM,\max} \tilde{v}_{TM}(z), \tag{4.6}$$

where $F_{i,\max}$ represents the peak amplitude of the fluorescence profile $\langle F_i(z) \rangle$ from the *i*-th layer and $\tilde{v}_i(z)$ is the scaled volume function $\tilde{v}_i(z) = V_i(z) / \max(V_i(z))$. The Q-parameter for the three-layer model is directly computed from Eq. 4.4 by inserting the appropriate shape factor into the generalized volume function $V_{r,i}(z)$,

$$\begin{aligned} Q(z) = {} & \gamma_{2,BM}(z) \lambda_{BM} f_{BM}(z) + \gamma_{2,Cyto}(z) \lambda_{Cyto} f_{Cyto}(z) \\ & + \gamma_{2,TM}(z) \lambda_{TM} f_{TM}(z) \end{aligned} . \tag{4.7}$$

Each layer is specified by its Q-factor, $Q_i(z) = \gamma_{2,i}(z) \cdot \lambda_i$, and fractional intensity, $f_i(z) = \langle F_i(z) \rangle / \langle F(z) \rangle$. The total Q-factor is given by summing the Q-factor of each layer weighted by its fractional intensity $f_i(z)$.

It is convenient to report the brightness of each layer λ_i as a normalized value by comparing it to the brightness λ_{EGFP} of EGFP, $b_i = \lambda_i / \lambda_{EGFP}$. A normalized brightness $b_i = 1$ indicates a monomeric protein, while $b_i = 2$ indicates a dimer in the *i*-th layer. For measurements of stoichiometry, it is helpful to convert the Q-factor into a z-dependent normalized brightness $\hat{b}(z)$ by dividing $Q(z)$ by the brightness of EGFP and the conventional gamma factor $\gamma_{2,\infty}$,

$$\begin{aligned} \hat{b}(z) = {} & \mu_{BM}(z) f_{BM}(z) b_{BM} + \mu_{Cyto}(z) f_{Cyto}(z) b_{Cyto} \\ & + \mu_{TM}(z) f_{TM}(z) b_{TM} \end{aligned} \tag{4.8}$$

where we introduced the gamma factor ratio $\mu_i = \gamma_{2,i} / \gamma_{2,\infty}$. We stress that b_{BM}, b_{TM}, and b_{Cyto} are the proper brightness values of the three layers. However, these values are not directly experimentally accessible. The experimental brightness $\hat{b}(z)$ at each z-position is a complex composite containing the brightness from each layer. Because $\hat{b}(z)$ requires further processing to extract the oligomeric state of proteins at each layer, we refer to it as raw brightness throughout the rest of the chapter.

4.3.3 Experimental intensity profiles of multiple layers

Applying the above theory to experimental data requires one more crucial ingredient, the PSF, because it connects the shape factor with the generalized volume function $V_r(z)$. The experimental PSF is commonly approximated by either the 3DG function, or the squared GL function. However, neither of these functions sufficiently approximates the axial profile of our PSF. As noted in chapter 2, we chose to model experimental z-scan data with the mGL function (76)

$$PSF_{mGL}(\rho,\zeta) = \left(\frac{z_0^2}{z_0^2+\zeta^2}\right)^{(1+y)} \exp\left(-\frac{4z_0^2}{w_0^2}\frac{\rho^2}{z_0^2+\zeta^2}\right). \tag{4.9}$$

The radial and axial beam waist are characterized by w_0 and z_0, while *y* adjusts the axial decay of the PSF. The z_0 and *y* parameters of the PSF were determined experimentally as described in section 4.2.4.

The plasma membrane protein EGFP-H-Ras expressed in U2OS cells served as a multi-layer test system. The z-dependent intensity trace shows a distinct double peak (see Figure 4.2A, black line) suggesting that the protein is predominately located at the cell membrane. We initially fit the experimental intensity profile with a two-layer model by setting $\langle F_{Cyto}(z)\rangle$ in Eq. 4.5 to zero. The result of this fitting was unsatisfactory, because systematic deviations between data and model were observed (reduced χ-squared of 2.8). We suspected that the misfit was caused by the presence of cytoplasmic EGFP-H-Ras. We removed the constraint $\langle F_{Cyto}(z)\rangle = 0$ and successfully refit the EGFP-H-Ras intensity profile with the general three-layer model. The fit (Figure 4.2A, solid grey line)

shows no systematic deviations and has a reduced χ-squared of 1.4. In fitting the data, information was obtained about the z-dependent intensity for the cytoplasmic component (dotted-dashed line), the z-dependent intensities from the membrane components (dotted lines), and cell height $h = z_{TM} - z_{BM}$. Since the cytoplasmic contribution to the signal was small, EGFP-H-Ras is a useful model system for a predominantly membrane-bound protein distribution.

Finally, we varied the ratio of cytoplasmic to membrane-bound protein by coexpressing mCherry and EGFP-H-Ras in U2OS cells. The mCherry protein populated the cytoplasmic pool, while EGFP-H-Ras contributed mainly to the membrane-bound component. Expressing two differently colored fluorescent proteins provided a convenient method to quickly select transfected cells expressing each protein at the desired intensity ratio. Although the fluorescence was split into a green and red detection channel, we combined the photon counts of both channels in software to mimic the fluorescence signal of a single-colored fluorescent protein found in the cytoplasm and at the membrane. The z-scan intensity profile (*solid line*) of the combined signal from a coexpressing cell is shown in Figure 4.2B together with a successful fit (*shaded line*) of the data by Eq. 4.6 with a reduced χ-squared of 1.3. While the additional presence of mCherry made the cytoplasmic intensity more prominent than in Figure 4.2A, each membrane layer along with the cytoplasmic layer was still cleanly resolved by the fit. Thus, the three-layer model successfully described the z-dependent intensity profiles for proteins with membrane-bound and cytoplasmic populations.

4.3.4 Brightness measurements in multi-layer protein geometries

Before taking brightness measurements it is illustrative to consider the influence of the three-layer geometry on the raw brightness by studying the z-dependence of Eq. 4.8 for a few select cases. For a purely cytoplasmic monomeric protein, such as EGFP, Eq. 4.8 reduces to

$$\hat{b}(z) = \mu_{Cyto}(z) \cdot b_{Cyto}$$

with $b_{Cyto} = 1$. The corresponding raw brightness curve (see Figure 4.3A, *shaded line*) for a thick (5μm) cytoplasmic layer approaches one as the focus of the beam reaches the center of the sample where $\mu_{cyto} = 1$, because the entire PSF is embedded in the sample. These are the conditions where conventional FFS, which ignores sample geometry, is valid.

Next, consider a monomeric protein only found at the bottom plasma membrane, which simplifies Eq. 4.8 to

$$\hat{b}(z) = \mu_{BM}(z) \cdot b_{BM}$$

with $b_{BM} = 1$. The brightness curve (Figure 4.3A, *solid line*) has a single peak with a maximum at the position of the bottom membrane. We notice that the raw brightness at the bottom membrane exceeds one. This increase is caused by the sample geometry, which is reflected in the gamma factor ratio $\mu_{BM}(z_{BM}) = \gamma_{2,BM}(z_{BM}) / \gamma_{2,\infty}$. In fact, one may think of the gamma factor ratio $\mu_i(z)$ as the bias factor in brightness due to sample geometry. The bias factor of a delta layer is $\mu_{BM}(z_{BM}) \approx 1.8$ for our PSF. Thus, conventional FFS analysis of a protein at the membrane overestimates brightness by ~1.8

due to the thin geometry. The raw brightness curve for a monomeric protein at the top membrane (Figure 4.3A, dashed black line) is identical to that of the bottom membrane except for a shift in the z-position, reflecting the different location of the membrane.

The general case involves proteins occupying the cytoplasm and the membranes. The resulting raw brightness curve is, according to Eq. 4.8, the superposition of the raw brightness curve from each layer (Figure 4.3A) weighted by its fractional intensity $f_i(z)$. The dependence of the raw brightness $\hat{b}(z)$ on the fractional intensity, the geometric bias factor, and the brightness of each layer, leads to a convoluted signal that is not straightforward to interpret. We illustrate this point in Figure 4.3B by plotting Eq. 4.8 for a slab with a thickness of 3 µm with monomeric EGFP $(b_{BM} = b_{Cyto} = b_{TM} = 1)$ distributed between the bottom membrane, the cytoplasm and the top membrane with an intensity ratio $F_{BM,\max} : F_{Cyto,\max} : F_{TM,\max}$ of 3:1:3. We see that the raw brightness peaks at the membranes are reduced as compared to the value of 1.8 expected for a monomeric protein at the membrane as discussed earlier. The raw brightness at the center of the cytoplasmic slab is less than the expected value of 1. Thus, quantitative analysis of the raw brightness curve is essential to link $\hat{b}(z)$ to the actual brightness of each layer.

Measuring the complete raw brightness curve $\hat{b}(z)$ and fitting it to Eq. 4.8 is very time consuming, because an FFS measurement at a single z-position takes tens of seconds. A closer look at Eq. 4.8 reveals that measuring $\hat{b}(z)$ at three different locations (z_{BM}, z_{TM}, z_{mid}) is sufficient to calculate the brightness of each layer (b_{BM}, b_{Cyto}, b_{TM}). The additional information needed for Eq. 4.8 is obtained by a fit of the intensity profile

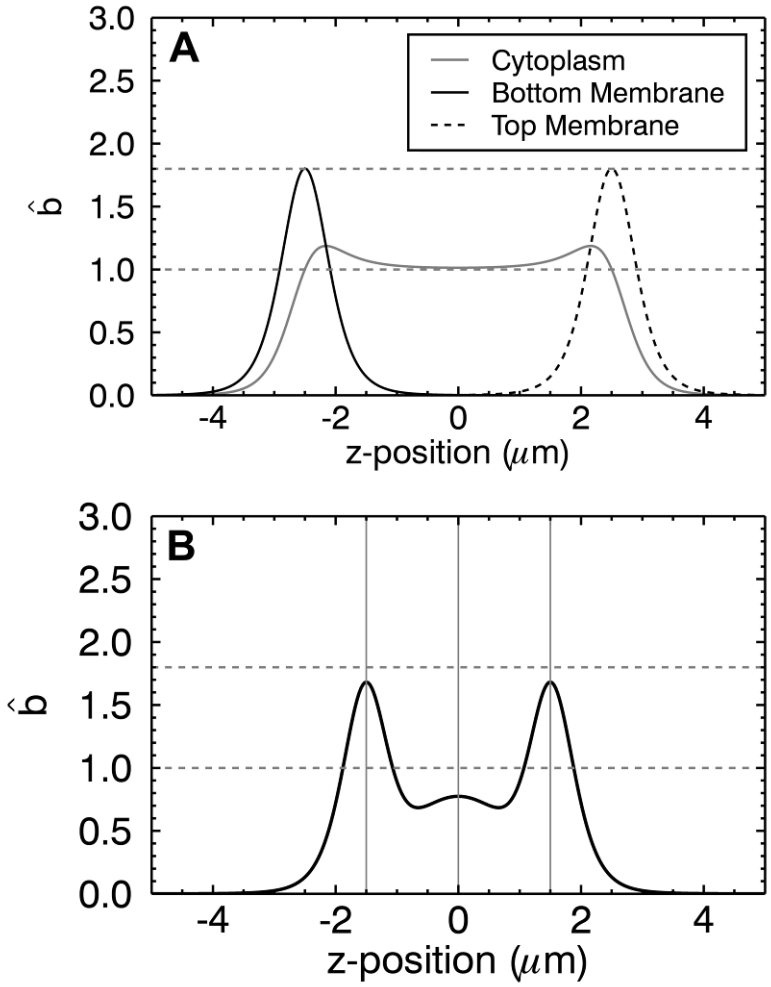

Figure 4.3 Modeling of raw brightness as a function of z-position.

(*A*) The raw brightness is calculated assuming a cell with a height of 5 μm. *(Shaded line)* Raw brightness $\hat{b}(z)$ for EGFP in a cell. *(Solid and dashed lines)* Raw brightness $\hat{b}(z)$ for a monomeric membrane protein labeled with EGFP located at either the bottom or top plasma membrane. (*B*) The raw brightness $\hat{b}(z)$ is calculated assuming a cell with a height of 3 μm and a monomeric protein distributed between the cytoplasm and the plasma membrane with an intensity ratio of $F_{BM,max} : F_{Cyto,max} : F_{TM,max}$ of 3:1:3. The raw brightness in the cytoplasm and also at the plasma membrane is suppressed as compared to (*A*) due to the coexcitation of fluorescent proteins across adjacent sample layers.

$\langle F(z)\rangle$, which provides the fluorescence signal $\langle F_i(z)\rangle$ from each layer as well as the location (z_{BM}, z_{TM}) of the membrane layers. This information serves to calculate the gamma factor ratios and fractional intensities that appear in Eq. 4.8. For the three raw brightness values $\hat{b}(z)$ we chose to measure at the bottom membrane, at the top membrane, and at mid-height in the cytoplasm. The experimental values $\hat{b}(z_{BM})$, $\hat{b}(z_{TM})$, and $\hat{b}(z_{mid})$ together with the fit of the intensity profile $\langle F(z)\rangle$ and Eq. 4.8 supply three equations

$$\begin{pmatrix} \hat{b}(z_{BM}) \\ \hat{b}(z_{mid}) \\ \hat{b}(z_{TM}) \end{pmatrix} = \begin{pmatrix} \alpha_{BM}(z_{BM}) & \alpha_{Cyto}(z_{BM}) & \alpha_{TM}(z_{BM}) \\ \alpha_{BM}(z_{mid}) & \alpha_{Cyto}(z_{mid}) & \alpha_{TM}(z_{mid}) \\ \alpha_{BM}(z_{TM}) & \alpha_{Cyto}(z_{TM}) & \alpha_{TM}(z_{TM}) \end{pmatrix} \times \begin{pmatrix} b_{BM} \\ b_{Cyto} \\ b_{TM} \end{pmatrix}, \tag{4.10}$$

where the matrix elements are given by $\alpha_i(z) = \mu_i(z)\, f_i(z)$. Inverting the above equation determines the parameters b_{BM}, b_{Cyto}, and b_{TM}.

To test multi-layer brightness analysis at the plasma membrane, cells expressing the membrane protein EGFP-H-Ras were used as an experimental trial system. An intensity z-scan was followed by point FFS measurements at the top plasma membrane (z_{TM}), the bottom plasma membrane (z_{BM}), and in the cytoplasm (z_{mid}). The brightness values measured at the top and bottom membrane exceeded 1, brightness measured in the cytoplasm scattered between 0.3 and 1 (see Figure 4.4A). By analyzing the raw brightness $\hat{b}(z)$ as described above we identify the brightness from each layer (Figure 4.4B). The analysis reveals that in U2OS cells, EGFP-H-Ras is monomeric both at the membrane and in the cytoplasm for all measurements.

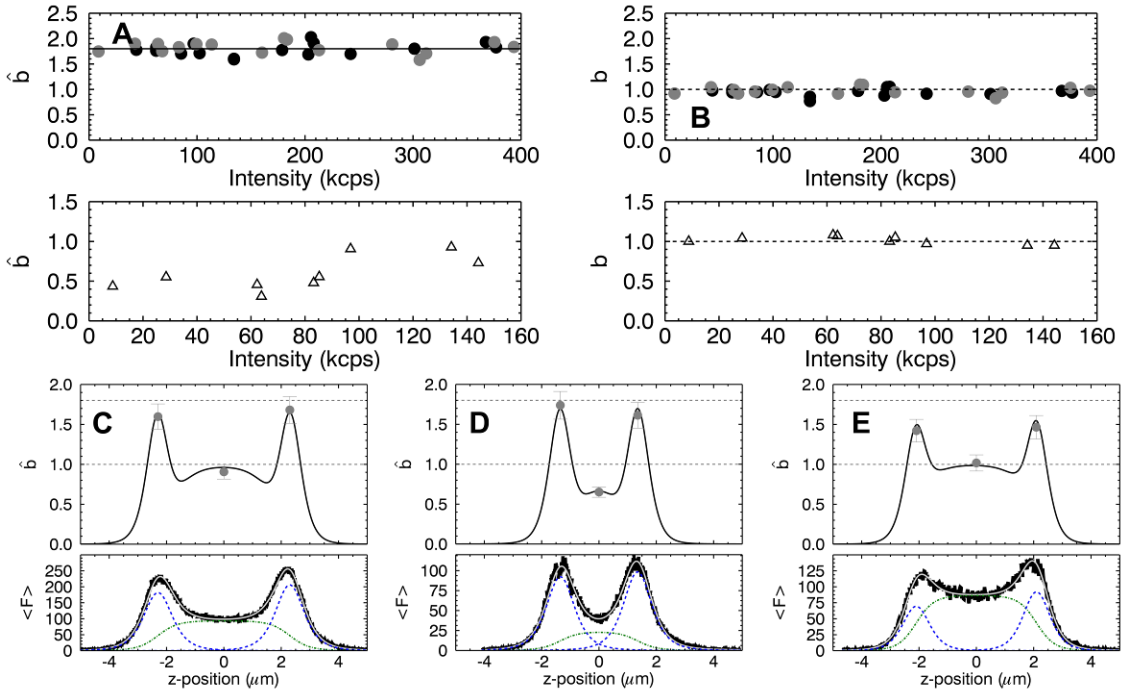

FIGURE 4.4. Z-scan brightness analysis of EGFP-H-Ras.

(*A*) *(Top Panel)* Raw brightness $\hat{b}(z_{membrane})$ measured at the top *(shaded circles)* and bottom *(solid circles)* membrane versus the fluorescence intensity (mean and standard deviation (SD) of 1.72 ± 0.13). *(Bottom Panel)* Raw brightness $\hat{b}(z_{mid})$ from the mid-point in the cytoplasm *(open triangles)* (mean and SD of 0.59 ± 0.22). (*B*) *(Top panel)* True EGFP-H-Ras brightness $b_{membrane}$ at the top *(shaded circles)* and bottom *(solid circles)* membrane (mean and SD of 1.00 ± 0.06); *(bottom panel)* true brightness b_{cyto} *(open triangles)* in the cytoplasm (mean and SD of 1.01 ± 0.06). (*C* and *D*) EGFP-H-Ras z-scan plots for two cells with different thicknesses. *(Bottom panels)* Intensity traces in kilo counts/s *(solid line)* and fit *(shaded line)* along with the fitted profiles from each layer. *(Top panels)* Measured raw brightness *(shaded circles)* at z_{BM}, z_{mid}, and z_{TM}. The raw brightness curves *(solid line)* are generated for the lower-panel intensity curves assuming monomeric proteins at both membranes and in the cytoplasm. (*E*) Z-scan FFS experiment of a cell expressing EGFP-H-Ras and EGFP. The graphs and labeling are identical to (C).

We provide a detailed analysis of two separate z-scan FFS experiments performed on cells expressing EGFP-H-Ras to illustrate the dependence of $\hat{b}(z)$ on geometry. The bottom panel of Figure 4.4C shows the intensity profile of a cell with a wider separation of the membranes than the cell in Figure 4.4D. After fitting the intensity profile of both cells, the raw brightness curves $\hat{b}(z)$ were calculated assuming a brightness of 1 at the membrane and in the cytoplasm. Thus, the raw brightness curves shown in the top panels of Figure 4.4C and 4.4D represent the case of monomeric EGFP-H-Ras, and the measured brightness values $\hat{b}$ (*shaded dots*) at the membranes and in the center of the cytoplasmic slab are in good agreement with the raw brightness curve. The raw brightness $\hat{b}$ at the membrane in Figs. 4.4C and 4.4D is close to the value of 1.8. The slight reduction in brightness reflects the coexcitation of cytoplasmic protein that leads to a drop in the fractional intensity at the membrane. Because the intensity contributions from the cytoplasm are small, the decrease in the fractional intensity at the membrane is minor and the raw brightness $\hat{b}$ predominantly reflects the brightness of a purely membrane-bound protein enhanced by the geometric bias factor of 1.8 (see Figure 4.3A).

The raw brightness $\hat{b}(z_{mid})$ in the cytoplasm, on the other hand, is significantly affected by the thickness of the cell at the position of the z-scan. While a thick slab (Figure 4.4C) leads to very little suppression of $\hat{b}$ due to contributions of the membrane signal, a thinner slab (Figure 4.4D) leads to a significant reduction in $\hat{b}$. This coexcitation dependence on brightness is largely responsible for the scatter in the measured raw brightness values of Figure 4.4A.

The coexcitation dependence also affects the brightness at the membrane when a large relative pool of protein exists in the cytoplasm. Since cytoplasmic protein levels for EGFP-H-Ras alone were relatively low, we demonstrated this effect by increasing the pool of cytoplasmic fluorescent proteins through coexpression of EGFP and EGFP-H-Ras. Figure 4.4E shows the z-scan FFS analysis of a cell expressing both proteins in which the fluorescence of the cytoplasmic pool (Figure 4.4E, *bottom panel*) is much larger than for EGFP-H-Ras alone. This leads to a significant reduction of the raw brightness at the membrane position from the value of 1.8 (Figure 4.4E, *top panel*), because the larger cytoplasmic fluorescence introduces a pronounced drop in the fractional intensity of the membrane signal.

4.3.5 Matrix domain of HTLV-1 Gag

While assembly of the retrovirus requires the full-length Gag protein, the process is complex and involves hundreds to thousands of Gag copies that pack together into individual Gag puncta. We chose to simplify the problem by investigating the MA domain of Gag, because MA is the primary driver of Gag association with the inner leaflet of the plasma membrane, but it lacks the ability to multimerize into large complexes (114, 116). We first assessed the potential of MA-EGFP to bind to the plasma membrane. Z-scans were performed on U2OS cells transiently expressing either HTLV-1 MA-EGFP or HIV-1 MA-EGFP. Visual inspection of the z-scan intensity trace from each protein (see Figure 4.5A) identified distinct differences in behavior. HIV-1 MA-EGFP (*shaded line*) appears to be a cytoplasmic protein, while HTLV-1 MA-EGFP (*solid line*)

has a significant membrane-bound component as indicated by the double peak in the intensity profile.

A fit of the data to the three-layer model confirmed that the HIV-1 MA-EGFP trace has no detectable protein component at the membrane, while HTLV-1 MA-EGFP has the majority of its intensity coming from the membrane, suggesting a strong plasma membrane component. Repeating z-scan measurements on cells expressing the protein at various concentrations confirmed these observations (data not shown). HIV-1 MA-EGFP is only found in the cytoplasm, while HTLV-1 MA-EGFP has a significant membrane-bound component. While we often observed differences in the intensity peaks at the top and bottom membrane, there was no systematic trend favoring one membrane over the other. The differential binding of MA to the plasma membrane for these two retroviruses agrees with a previous study (108).

Raw brightness measurements were taken for HIV-1 MA-EGFP in the cytoplasm and z-scan FFS analysis, as previously described for a single layer, and were used to determine the cytoplasmic brightness (76). HIV-1 MA-EGFP displayed monomeric brightness at all concentrations (data not shown). This is consistent with the literature which suggests that the HIV-1 MA protein does not exhibit appreciable homo-interactions at physiological concentrations (118, 119). For HTLV-1 MA-EGFP we measured raw brightness $\hat{b}$ values at both plasma membranes and at the mid-section in the cytoplasm (Figure 4.5B). The top panel of Figure 4.5B shows the raw brightness $\hat{b}$ (*shaded dots*) as well as a theoretical raw brightness curve determined from the z-

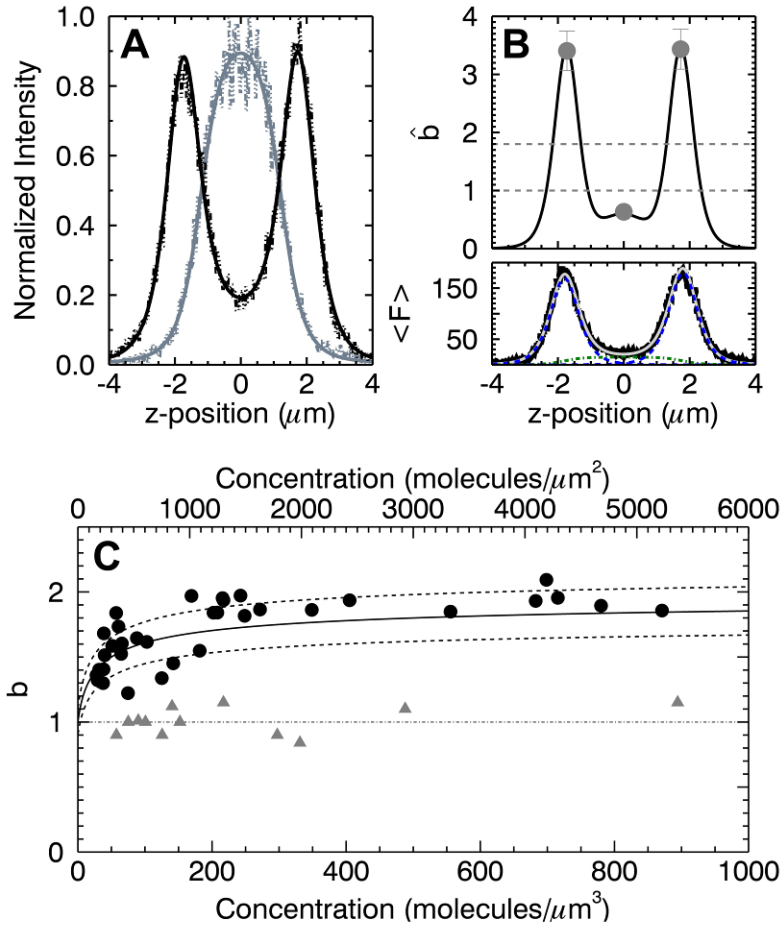

Figure 4.5 z-scan brightness analysis of MA domain of Gag proteins.

(*A*) Normalized intensity of HIV-1 MA-EGFP (*light dotted line*) and fit (*shaded line*) to cytoplasmic slab model and of HTLV-1 MA-EGFP (*dark dotted line*) and fit (*solid line*) to Eq. 4.6. (*B*) Brightness and intensity data from a cell expressing HTLV-1 MA-EGFP. The raw brightness (*shaded circles*) taken at the bottom membrane, cytoplasm, and top membrane (*top panel*) together with a modeled brightness curve generated for the intensity trace (*bottom panel*) assuming a monomeric protein in the cytoplasm and a dimeric protein at the plasma membrane. (*C*) Brightness from a population of cells expressing HTLV-1 MA-EGFP. The brightness at the membrane (*solid circles*) as a function of the areal protein density (μm^{-2}) shows a concentration-dependent monomer to dimer transition. Dimer binding curve (*solid line*) with a dissociation coefficient of ~300 μm^{-2} and ± 10% error bounds (*dotted lines*) for brightness at the membrane. The brightness in the cytoplasm (*shaded triangles*) as a function of the volume protein density (μm^{-3}) is monomeric at all measured concentrations.

intensity trace (*bottom panel*). We note that $\hat{b}$ at the membrane exceeds 1, while $\hat{b}$ in the cytoplasm is typically less than 1 which reflects the multi-layer nature of the sample. For this specific HTLV-1 MA-EGFP measurement, the raw membrane brightness $\hat{b}$ exceeded 3 which suggested the presence of protein-protein interaction at the membrane. After applying Eq. 4.10 to the raw brightness values we determined that the true brightness values are $b_{BM} = 1.97 \pm 0.21$, $b_{TM} = 1.97 \pm 0.21$, and $b_{cyto} = 1.06 \pm 0.12$.

To further study the behavior of HTLV-1 MA-EGFP at the plasma membrane we performed z-scan FFS measurements on a population of cells with varying HTLV-1 MA-EGFP concentrations. We applied the matrix analysis of Eq. 4.10 to the experimental $\hat{b}$ data to isolate the membrane brightness (b_{BM}, b_{TM}) and cytoplasmic brightness (b_{Cyto}) of the tagged HTLV-1 MA protein (Figure 4.5C). The cytoplasmic brightness b_{Cyto} is concentration independent, $b_{cyto} = 1.01 \pm 0.12$. The brightness of HTLV-1 MA-EGFP at the plasma membrane, on the other hand, exhibits a concentration dependent increase from approximately one at low concentration to a value of two at high concentration. Thus, the data reveal that HTLV-1 MA-EGFP undergoes a monomer to dimer transition with the solid line representing a binding curve with a dimerization dissociation coefficient of ~300 molecules/μm^2

4.4 Discussion

Our results demonstrate that properly identifying the brightness of fluorescently-labeled proteins found both at the plasma membrane and in the cytoplasm is challenging.

A few earlier studies have noted that fluorescence from neighboring layers qualitatively affects the measured brightness (4–6). In addition, brightness bias at the membrane due to delta-layer geometry was mentioned, but could not be experimentally identified (7). This study demonstrates that there are primarily three factors that confound quantitative interpretation of brightness measurements: the geometry of the layer, the intensity contribution from adjacent layers, and the brightness of adjacent layers. We briefly discuss each of these factors.

The first factor is the geometric effect, which for a stratified layer boils down to the thickness of each layer. When applying conventional FFS, a layer that is thinner than the axial length of the excitation PSF will lead to an increase in the raw brightness as originally reported by Macdonald et al (76). In the extreme case of a delta layer, as is used to describe the plasma membrane, the raw brightness is increased by ~1.8 for our excitation PSF.

The second factor accounts for the presence of background fluorescence from neighboring layers. The fluorescence signal of a layer is diluted by this background signal, which lowers the fractional intensity and thereby the raw brightness.

The third factor accounts for differences in brightness at neighboring layers. To illustrate its effect, we used Eq. 4.8 to calculate the raw brightness $\hat{b}(z_{BM})$ at the bottom membrane as a function of the fractional intensity $f_{BM}(z_{BM})$ for a cell with both membrane-bound and free cytoplasmic protein populations (see Figure 4.1A). In Figure 4.6, we systematically changed the actual brightness at the membrane from a monomer to a trimer, while keeping the cytoplasmic protein a monomer in all cases. The raw

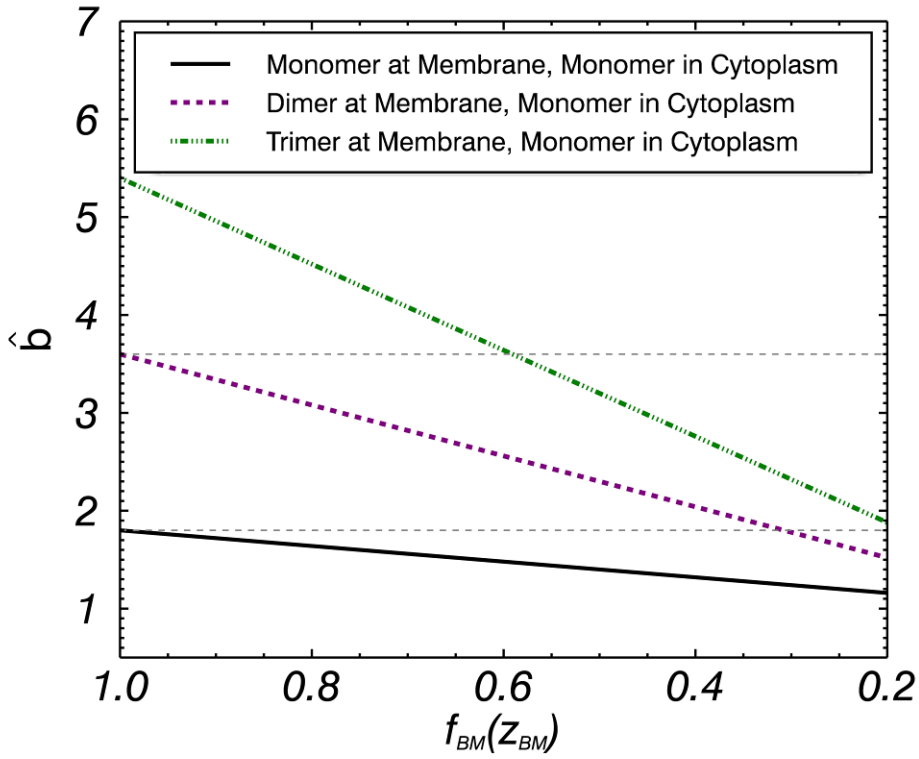

Figure 4.6 Modeled raw brightness.

The modeled raw brightnenss $\hat{b}(z_{BM})$ at the bottom membrane is given as a function of the fractional intensity $f_{BM}(z_{BM})$ for a cell with both membrane-bound and cytoplasmic protein populations. $\hat{b}(z_{BM})$ was modeled for monomeric, dimeric, and trimeric protein at the membrane while keeping the cytoplasmic protein a monomer in all cases. The raw brightness $\hat{b}(z_{BM})$ decreases as a function of fractional intensity in all cases but decreases more rapidly as the brightness difference between the cytoplasm and membrane increases.

brightness $\hat{b}$ decreases as a function of fractional intensity for all cases, but the slope differs significantly. In general, a larger brightness difference between the cytoplasmic and membrane-bound protein leads to a steeper drop in raw brightness with fractional intensity. This issue is significant because membrane binding frequently promotes oligomerization of the protein at the membrane while the cytoplasmic fraction remains in monomer form. Thus, the fluorescence background from the cytoplasm and the brightness difference between the membrane-bound and cytoplasmic fractions lead to a reduced measured brightness at the membrane, which hampers the proper identification of the oligomeric state.

Although this work used a mGL-PSF model for fitting the data, it is important to emphasize that the z-scan method is not tied to any particular PSF model. The only requirement is an accurate parameterization of the experimental PSF. Extension of the z-scan method to one-photon excitation only requires a proper parameterization of the one-photon PSF. To be more precise, one-photon excitation uses the observation volume $O(\rho,\zeta)$ instead of the PSF to account for the effect of the pinhole on the collected fluorescence emission. This observation volume can be modeled by multiplying the excitation PSF by a collection profile function (120). Once a proper parameterization of $O(\rho,\zeta)$ has been obtained, z-scan analysis with one-photon excitation can be performed by replacing the PSF of Eq. 4.9 with $O(\rho,\zeta)$.

If a protein resides exclusively at the plasma membrane, then the problem reduces to a single layer, provided the top and bottom membrane are sufficiently far apart to avoid coexcitation. In this case the brightness of a protein at the plasma membrane can be

measured directly (5, 6, 121). Relating the measured brightness with the oligomeric state of the protein relies on a calibration experiment with a monomeric membrane protein to identify the monomeric brightness value. H-Ras appears to be an acceptable monomeric brightness standard for U2OS cells. In Appendix A we added a tandem dimeric EGFP label to H-Ras ($EGFP_2$-H-Ras) and measured its brightness at the plasma membrane. The data show that labeled H-Ras provides a suitable brightness standard in U2OS cells. However, in MDCK cells, we observed both monomeric and higher brightness states for EGFP-H-Ras (data not shown). It was recently reported that H-Ras was found in both monomeric and cluster form at a ratio of 70/30 for each respective species (122) in BHK cells. Thus, identifying a brightness standard for membrane measurements appears challenging, because the cell line and cell environment can potentially alter the oligomerization and clustering of the protein.

To avoid these potential complications we suggest a straightforward alternative to establish the monomeric brightness at the membrane. A routine measurement of the fluorescent protein in the cytoplasm or nucleoplasm determines the true monomeric brightness $\lambda_{monomer}$. We account for the delta layer geometry of the membrane by multiplying $\lambda_{monomer}$ by the geometric bias factor $\mu_M(z_M)$ for a membrane, which is calculated as described earlier. The product

$$\hat{\lambda}_{monomer} = \mu_M(z_M)\lambda_{monomer}$$

represents the calibration brightness for a monomer at the membrane. This calibration procedure works as long as the brightness near the membrane and in the cytoplasm are the same. A constant brightness is an essential property of any fluorescent protein suited

for quantitative brightness experiments and needs to be established independently for each new fluorescent label (75). For example, EGFP has a stable brightness that remains unchanged when tagged to another protein, as well as, when measured in the nucleus, cytoplasm and in vitro (1, 75). As expected and shown by our data, the brightness of EGFP at the plasma membrane and in the cytosol is the same as long as geometry is accounted for. Thus, the above calibration procedure should prove useful for any fluorescent protein suited for quantitative brightness experiments.

Fluorescence from neighboring layers also affects the raw brightness in the cytoplasm, although this issue has not received much attention yet. A recent study observed unphysically low brightness values in the cytoplasm when studying HIV-1 and HTLV-1 Gag interactions in cytoplasm (107), which were traced back to the presence of fluorescence from a membrane-bound fraction of labeled Gag proteins. Here we observed the same phenomenon for H-Ras (Figure 4.4A) and HTLV-1 MA (Figure 4.5B). However, unlike the earlier study we used quantitative z-scan FFS to identify the correct brightness in the cytoplasm and at the membrane. Studying the MA domains of both HIV-1 Gag and HTLV-1 Gag revealed a purely cytosolic distribution of HIV-1 MA-EGFP, while HTLV-1 MA-EGFP was distributed between the cytoplasm and the plasma membrane, which agrees with recent observations (108) and implies fundamental differences between the early steps in HIV-1 and HTLV-1 assembly.

Our study further provides evidence that cytoplasmic HTLV-1 MA-EGFP binds the plasma membrane as a monomer, since HTLV-1 MA-EGFP was entirely monomeric in the cytoplasm and only exhibited a concentration-dependent monomer to dimer

transition at the plasma membrane. This observation is supported by immunoprecipitation and immunoblotting studies which identified the presence of stable MA dimers at the plasma membrane (123). Because we measure both cytoplasmic and membrane-bound pools of HTLV-1 MA-EGFP, our brightness data provide evidence that links the monomeric MA in the cytoplasm with the observed dimers at the membrane through the presence of MA-MA interactions that occur in the membrane-bound form. Of course, dimerization is only the first step towards assembly of the complete viral-like particle. Observing additional steps requires future experiments with the full-length Gag protein to account for the additional interactions outside the MA domain that play a role in the formation of high-order Gag complexes (124). The advances in brightness experiments presented here not only provide the foundation for future work with the full-length HTLV-1 Gag protein, but also should prove useful for studies of any protein that is distributed across stratified layers within the cell.

5. z-scan FPD of Cytosolic and Membrane-associated Protein Populations

This chapter introduces a technique that characterizes the spatial distribution of peripheral membrane proteins that associate reversibly with the plasma membrane. An axial scan through the cell generates a z-scan intensity profile of a fluorescently labeled peripheral membrane protein. This profile is analytically separated into membrane and cytoplasmic components by accounting for both the cell geometry and the point spread function. We experimentally validated the technique and characterized both the resolvability and stability of z-scan measurements. Further, using the cellular brightness of green fluorescent protein, we were able to convert the fluorescence intensities into concentrations at the membrane and in the cytoplasm. We applied the technique to study the translocation of the pleckstrin homology domain of phospholipase C-delta1 labeled with EGFP upon ionomycin treatment. Analysis of the z-scan fluorescence profiles revealed protein-specific cell height changes and allowed for comparison between the observed fluorescence changes and predictions based on the cellular surface area to volume ratio. The quantitative capability of z-scan fluorescence profile deconvolution offers opportunities for investigating peripheral membrane proteins in the living cell that were previously not accessible.

5.1 Introduction

Peripheral membrane proteins associate reversibly with cellular membranes through non-covalent interactions with lipids and integral membrane proteins. They

constitute a broad and diverse class of proteins involved in various membrane-mediated cellular processes including but not limited to cell signaling, cytoskeletal structure, lipid homeostasis, and electron transport (8, 10, 125). The ability to transition between a soluble and membrane-bound form has been recognized as an important regulation and control mechanism of cells. The interaction with the membrane provides a mechanism to induce conformational changes in the protein that modulate its activity. Vice versa, the interactions with the membrane-associated protein can also change the composition, dynamics, and shape of cellular membranes (126–129). As we mentioned in chapter 1, this complex, bidirectional interplay between peripheral membrane proteins and cellular membranes is only beginning to be unraveled through the use of model membrane systems and cellular studies.

The energetics and dynamics of the interaction process has been primarily studied with model membranes (21, 22). These experiments provide quantitative information about protein interactions with lipids, but like all *in vitro* studies cannot reproduce the environment and complex interaction network found in cells. Live-cell studies monitor peripheral membrane proteins in their natural habitat and are an essential complement to *ex situ* methods. Cellular translocation studies of fluorescent protein-tagged proteins provide a powerful and convenient approach to visualize the subcellular distribution of peripheral membrane proteins and their dynamic relocation in real time by fluorescence imaging methods, such as confocal or TIRF microscopy (29–31, 130).

Translocation studies typically report qualitative differences in the subcellular distribution of proteins, which reflects the difficulty of identifying the concentration of

the membrane-bound and soluble protein from fluorescence intensity data (29, 30). Attempts at quantifying the fluorescence signal to gain information about the relative strength of the interaction between protein and membrane have been restricted to heuristic approaches that are unable to analytically separate the fluorescence signal. The current study addresses this problem and introduces a fluorescence-based approach for measuring the time-resolved distribution of proteins at the plasma membrane and in the cytosol of a living cell.

We specifically focus on characterizing the interaction of a fluorescently labeled cytoplasmic protein with the plasma membrane. An axial scan of the two-photon PSF through the cell generates a z-scan intensity profile as illustrated in Figure 4.1. By accounting for the cell geometry and the PSF we recover the distinct cytoplasmic and membrane-bound protein fluorescence contributions from the intensity profile, a process we refer to as z-scan fluorescence profile deconvolution (FPD). The intensity profile was first introduced in the z-scan FFS studies of chapter 4 where it served as a byproduct for determining the proper weighing factors that connected the FFS data to the oligomeric state of proteins at the plasma membrane and in the cytoplasm. Here we focus exclusively on the z-scan intensity profile to demonstrate that it offers a powerful approach for studying protein binding at the plasma membrane without the need for time-consuming FFS measurements.

We first examined the resolvability limits of FPD analysis of the fluorescence intensity profile by systematically varying the cytoplasmic intensity relative to the membrane fluorescence intensity and studied the stability of z-scan measurements over a

prolonged sampling time. We applied the technique to investigate the translocation of the EGFP labeled pleckstrin homology (PH) domain of Phospholipase C-delta1 (PH-PLCδ-EGFP) in U2OS cells from the plasma membrane to the cytoplasm upon treatment with ionomycin. Quantitative analysis of the z-scan intensity profiles taken before and after treatment identified movement of the membrane position and allowed direct comparison between the fluorescence change at the membrane and in the cytoplasm.

5.2 Materials and methods

5.2.1 Experimental setup

All data were taken with a Zeiss 63x C-Apochromat water immersion objective (N.A.=1.2) on a home-built two-photon microscope as described in chapter 2. The experimental protocols for data collection and z-scanning are described in section 4.2.1. In addition to z-dependent fluorescence intensity scans, we performed independent measurements on cells expressing the fluorescent label EGFP to determine its brightness λ_{EGFP} as previously described in section 4.2.3. This brightness serves as a calibration factor for the conversion of fluorescence intensities into concentrations.

5.2.2 Sample preparation and cell measurements

The pEGFP-C1 and pEGFP-N1 plasmids were purchased from Clontech (Mountainview, CA), and the mCherry-C1 plasmid has been previous described (131). The EGFP-H-Ras plasmid was a gift from Dr. Mark Phillips (New York University School of Medicine). The PH-PLCδ-EGFP plasmid was a gift from Dr. Joseph Abanesi

(University of Texas-Southwestern). All sequences were verified by automatic sequencing. The cellular studies were performed using transiently transfected U2OS cells (HTB-96) that were obtained from ATCC (Manassas, VA) and maintained in 10% fetal bovine serum (Hycolone Laboratories, Logan, UT) and DMEM medium. Cells were subcultered in eight-well coverglass chamber slides (Nalge Nunc International, Rochester, NY) 12 hours before transfection. Transient transfections were carried out using GeneJet (Thermo Scientific, Pittsburgh, PA) according to the manufacturer's instructions, 24 hours prior to measurement. Immediately before measurement, the growth medium was replaced with 200 µL of Leibovitz's L-15 Medium, no phenol red (Gibco, Life Technologies, Grand Island, NY).

For kinetic studies, repeated z-scans were performed on individual cells. An objective heater with a thermal controller (MATS-ULH, Tokai Hit, Japan) was used to maintain a medium temperature of 32°C. Prior to scanning, 100 µL of medium was removed from the well. Pre-warmed L-15 medium (100 µL) containing Texas Red and ionomycin calcium salt (Life Technologies, Carlsbad, CA) was later added to the well, for a final concentration of 1.26 mM for Ca^{2+} and 5 or 10 µM for ionomycin. Texas Red served as a tracer to identify the time of delivery of ionomycin at the cell and was monitored in the red detection channel.

The delta layer model was created by using a layer of rhodamine fibronectin (Cytoskeleton, Inc, Denver, CO). The fibronectin layer was created by pipetting a solution of 200 µl of buffer (0.5M NaCl, 0.5M Tris, pH=7.5) mixed with 13 µg of fibronectin into a chamber of an eight-well coverglass slide. The 8-well was then placed

in an incubator for 24 hours before the remaining liquid was pipetted out and replaced with 200 µl of Dulbecco's phosphate-buffered saline (PBS) with calcium and magnesium (Biowhittaker, Walkerville, MD). For the semi-infinite model, a dilute fluorescein solution was added to a well of the chamber slide.

5.2.3 Z-scan calibration of PSF

As discussed in chapter 2, a mGL-PSF,

$$PSF\left(\rho,\zeta\right)=\left(\frac{z_0^2}{z_0^2+\zeta^2}\right)^{(1+y)}\exp\left(-\frac{4z_0^2}{w_0^2}\frac{\rho^2}{z_0^2+\zeta^2}\right), \tag{5.1}$$

first introduced by Macdonald et al. (76), provides a good approximation of the PSF of our two-photon microscope and serves as the model for this study. A z-scan calibration procedure was performed as described previously in section 4.2.4 to determine the free parameters of our model. The calibration resulted in z_0 = 1.02 ± 0.1 µm, y = 2.20 ± 0.3 µm, and w_0 =0.47 ± 0.05 µm, where w_0 and z_0 describe the radial and axial beam waist, while y adjusts the axial decay of the PSF. Z-scan analysis relies on the radially integrated point spread function RIPSF, which for the mGL-PSF is given by (76),

$$\mathrm{RIPSF}(z)=\int_0^{\infty}\mathrm{PSF}(\rho,\zeta)\,2\pi\rho\,d\rho=\frac{\pi w_0^2}{4}\left(1+(z/z_R)^2\right)^{-y}. \tag{5.2}$$

The mGL PSF volume is given by

$$V_{\infty}=\int_{-\infty}^{+\infty}\mathrm{RIPSF}(\zeta)\,d\zeta=1/4\,(\pi w_0^2 z_R)\sqrt{\pi}\;\Gamma\left(y-\tfrac{1}{2}\right)/\Gamma(y),$$

and the cross-sectional area at the center of the mGL PSF is determined by $A_0 = \frac{\pi w_0^2}{4}$ (76).

5.2.4 Z-scan data analysis

The experimental protocol used for rebinning and fitting z-scan photon counts is described in section 4.2.6. To explore the resolvability of z-scan fitting, simulations were performed as follows. A z-scan intensity profile $F_{\text{model}}(z)$ for a membrane-cytoplasmic-membrane geometry was calculated from Eq. 5.6 using the calibrated PSF parameters and experimental step size Δz. The calculated intensity profile was converted into simulated data $F_{sim}(z)$ using a Poissonian random number generator $P_{Poisson}(\lambda)$ to account for shot noise, $F_{sim}(z) = \frac{P_{Poisson}\left(F_{\text{model}}(z) \cdot T_z\right)}{T_z}$.

5.3 Results

5.3.1 z-scan intensity profile of single layers

A scan of the TPE spot along the z-axis of a cell generates a fluorescence intensity profile $F(z)$. This intensity profile results from the convolution of the PSF of the instrument with the concentration profile $c_M(z)$ of the fluorescently labeled protein along the scan axis. We assume in this study that the concentration only varies along the z-direction, which reflects a geometry based on stratified layers. For a single layer a scan along the z-direction results in a fluorescence intensity function (76)

$$F(z) = \lambda c \int_{-\infty}^{\infty} S(\varsigma + z)\,\text{RIPSF}(\varsigma)\,d\varsigma\,, \tag{5.3}$$

where λ is the monomeric brightness of the labeled protein, c represents the concentration of the labeled protein expressed as monomers, and RIPSF is the radially integrated point spread function (76). The function $S(z)$ describes the geometric shape of the single layer (76) and will be discussed in more detail later. We define the concentration profile as the product of the protein concentration and the geometric shape function, $c_M(z) = c\,S(z)$.

We consider three basic geometries and their associated intensity profiles: the delta-layer, the slab, and the semi-infinite layer. The concentration profile of the slab layer $c_M(z) = c\,\Pi(z; z_B, z_T)$ is constant between z_B and z_T (Figure 5.1A), which corresponds to a geometric shape function $\Pi(z; z_B, z_T)$ that equals 1 for $z_B \le z \le z_T$ and 0 everywhere else. The fluorescence intensity profile for the slab layer is obtained from Eq. 5.3,

$$F(z) = F_\infty\,\alpha_V(z; z_B, z_T), \tag{5.4}$$

which introduces the fractional PSF volume $\alpha_V(z; a, b) = \int_{a-z}^{b-z} \mathrm{RIPSF}(\varsigma)\,d\zeta \Big/ V_\infty$ to describe the incomplete overlap of the PSF with the sample (51). This description differs from conventional FFS, where we assume a PSF that is completely embedded within the sample. In essence, conventional FFS corresponds to a shape function $S(z) = 1$ and a constant concentration profile $c_M(z) = c$. In this case Eq. 5.3 reduces to a z-independent fluorescence intensity, $F_\infty = \lambda c V_\infty$. Conversely for a thinner cell section, the PSF only achieves partial overlap with the sample, which is accounted for by a fractional PSF

volume $V(z) = V_\infty \alpha_V(z)$. The z-scan intensity profile through a cell expressing a fluorescently labeled cytoplasmic protein is well approximated by a fit to the slab model (Figure 5.1B). The maximum intensity $F_{\max}$ of the z-scan occurred at the midsection between the bottom and top layer, $z_{mid} = \frac{1}{2}(z_B + z_T)$, and is less than the limiting value of F_∞, because the cell thickness at the scan location is not sufficiently thick to completely embed the PSF ($\alpha_V(z_{mid}; z_B, z_T) < 1$).

The concentration profile of the semi-infinite layer (Figure 5.1C) is similar to the slab layer, but with $z_T \to \infty$, which leads to an intensity profile $F(z) = F_\infty \alpha_V(z; z_B, \infty)$. A good example of such an intensity profile is given by a z-scan through the microscope coverslip into a fluorescent solution as shown in Figure 5.1D together with a fit to the model. The intensity increases as the PSF moves deeper into the solution and reaches a maximum of F_∞ once it is completely embedded in the solution.

The delta-layer describes a very thin section, such as the plasma membrane, with a thickness which is much less than the axial size of the PSF. Its concentration profile is given by $c_M(z) = \sigma\,\delta(z - z_M)$, where $\delta(z)$ is the delta-function, σ represents the surface concentration of the layer, and z_M is the axial position of the thin layer (Figure 5.1E). The intensity profile for a delta-layer located at z_M is obtained from Eq. 5.3,

$$F(z) = \lambda\sigma\,\mathrm{RIPSF}(z_M - z) = F_{\max}\,\alpha_A(z_M - z). \tag{5.5}$$

The RIPSF value at a specific location *z* may be interpreted as an area determined by the cross section of the PSF with the delta layer, $A(z) = \mathrm{RIPSF}(z)$. The maximum of the

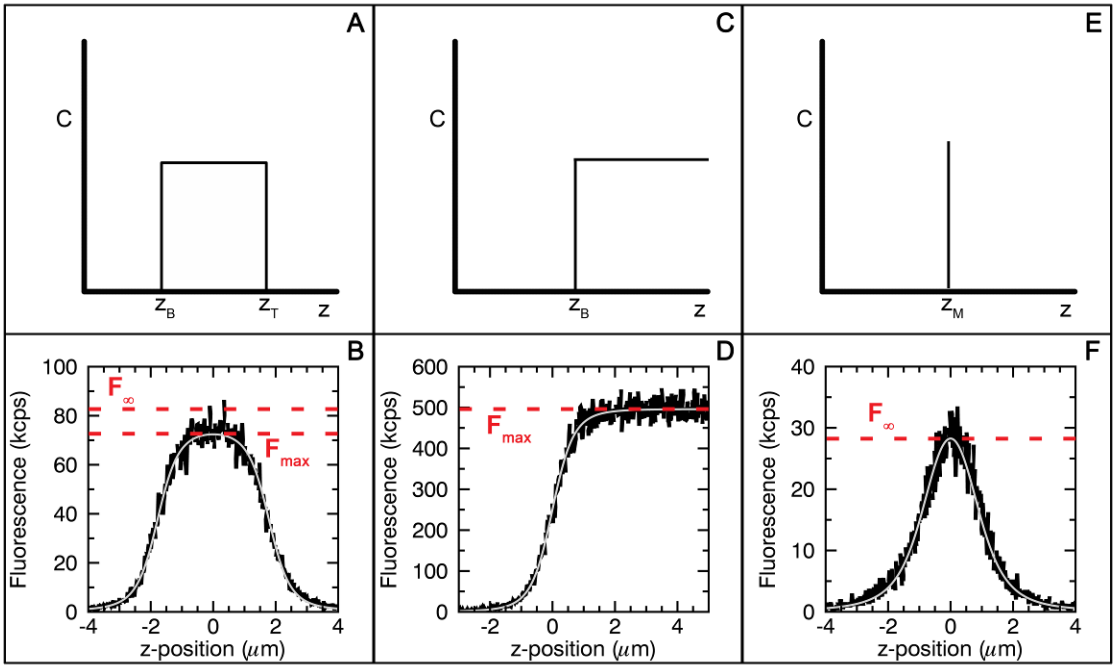

Figure 5.1 z-Dependent concentration and intensity profiles.

Z-dependent concentration function for a slab (*A*), semi-infinite (*C*), and delta (*E*) layer. The lower panels show an experimental intensity profile $F_{\exp}(z)$ (*solid line*) and fit to a model intensity profile $F_{\mathrm{mod}}(z)$ (*shaded line*) for each concentration function. (*B*) The intensity profile $F_{\exp}(z)$ of a fluorescent cell is described by the slab model (χ_r^2=1.2). The maximum intensity $F_{\max}$ is less than the intensity F_∞ for the infinite sample. (*D*) Intensity profile of a fluorescent solution matches the semi-infinite model (χ_r^2=1.1). (*F*) Intensity profile of thin fibronectin layer is in good agreement with $F_{\mathrm{mod}}(z)$ for a delta layer (χ_r^2=1.0).

intensity $F_{\max}$ is reached when the PSF is centered on the membrane ($z = z_M$), which corresponds to $F_{\max} = \lambda \sigma_0 A_0$ with $A_0 = A(0)$. We define a fractional PSF area by $\alpha_A(z_M - z) = A(z_M - z)/A_0$ to describe the intensity profile of Eq. 5.5 in compact form. A coverslip covered with a thin layer of fluorescently labeled fibronectin served as a model system for a delta-layer. A fluorescence intensity z-scan through the sample and its fit to Eq. 5.5 is shown in Figure 5.1F.

5.3.2 z-scan intensity profile of multiple layers

A peripheral membrane protein found at the plasma membrane and in the cytoplasm is described by a delta-slab-delta concentration profile $c_{dsd}(z)$ consisting of a delta layer for the bottom membrane located at z_B, followed by a slab layer and another delta layer representing the top plasma membrane located at z_T. This concentration profile (Figure 5.2A) can be written as

$$c_{dsd}(z) = \sigma_B \delta(z - z_B) + c_{Cyto} \Pi(z; z_B, z_T) + \sigma_T \delta(z - z_T),$$

where σ_B and σ_T denote the surface concentrations of the fluorescently-labeled protein at the bottom and top membrane, while c_{Cyto} is the cytoplasmic protein concentration. As we first introduced in chapter 4, the corresponding fluorescence intensity profile is the sum of the intensity profiles from each layer (51),

$$F_{dsd}(z) = F_B \alpha_A(z - z_B) + F_{Cyto,\infty} \alpha_V(z; z_B, z_T) + F_T \alpha_A(z - z_T) \qquad (5.6)$$

with F_B and F_T being the maximum fluorescence intensity at the membrane layers and $F_{Cyto,\infty}$ represents the limiting cytoplasmic intensity of a thick layer. We introduce the membrane intensity fraction f_M as a measure for the relative amount of fluorescence intensity coming from the membrane,

$$f_M = \frac{F_M}{F_M + F_{Cyto,\infty}}, \tag{5.7}$$

distinguishes between the bottom and top membrane, we further introduce the intensity fraction f_B of the bottom membrane and the intensity fraction f_T of the top membrane, which are defined by replacing F_M with F_B and F_T in Eq. 5.7, respectively. High membrane intensity fractions are easy to resolve, because the z-scan intensity profile displays two prominent peaks, as illustrated by the EGFP-H-Ras data (Figure 5.2B; f_B = 0.96 and f_T = 0.97). Conversely, we expect a larger uncertainty in determining f_M from data with lower membrane intensity fractions.

We transfected cells with EGFP-H-Ras and mCherry to experimentally determine the limits of resolvability of f_M. H-Ras is predominantly membrane-bound, while mCherry is entirely cytoplasmic. The presence of two differently colored fluorescent proteins provided a straightforward method to select cells expressing each protein at the desired intensity ratio. This approach allowed us to systematically vary the membrane intensity fraction over a wide range. Because the fluorescence was split into a green and red detection channel, we combined the photon counts of both channels in software to

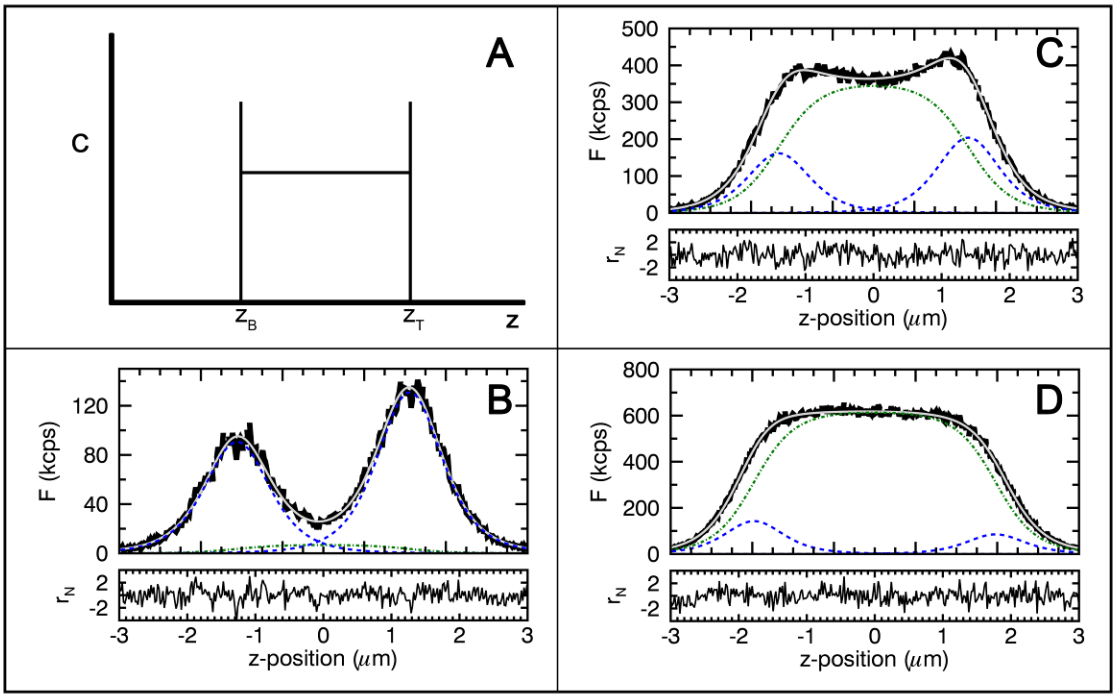

Figure 5.2 Delta-slab-delta model.

(*A*) Concentration profile. (*B*) Z-scan intensity profile for EGFP-H-Ras (*solid line*) and fit (*shaded line*) to Eq. 5.6 (f_B = 0.92, f_T = 0.95, χ_r^2 = 1.2) with normalized residuals in lower panel. (*Dotted-dashed line*) Contribution from the cytoplasmic layer; (*dotted lines*) contribution from the membrane layers. (*C*) and (*D*) Intensity profile of cells expressing EGFP-H-Ras and mCherry fit to delta-slab-delta model (χ_r^2 of 1.3 and 1.1).

mimic the fluorescence signal of a single-colored fluorescent protein found in the cytoplasm and at the membrane.

We selected two cells that illustrate z-scan intensity traces with low membrane intensity fractions. The intensity profile of Figure 5.2C retains a slight double peak, and the fit to the three layer model returns membrane intensity fractions of $f_B = 0.32$ and $f_T = 0.36$. The next intensity profile (Figure 5.2D) lacks the double peak, which is consistent with a fit returning lower membrane intensity fractions than in the previous case ($f_B = 0.19$, $f_T = 0.12$). We performed a systematic study by selecting cells based on the relative membrane intensity fraction and performed 10 consecutive z-scans at a thick section of each cell. After fitting the intensity profile of each scan the average and standard deviation of the 10 membrane intensity fractions was calculated and is plotted as stars in Figure 5.3A. The experiments were performed on cells with cytoplasmic intensities $F_{Cyto,\infty}$ ranging from 100 to 1000 kcps and scans were taken at cell heights ranging from 2.2 µm to 4.1 µm (mean of 3.1 µm).

We further performed simulations to compare the experimental uncertainties with predictions based on our model. Intensity traces were calculated according to Eq. 5.6 with shot noise added to account for the photon detection noise. Parameters were chosen that mimic the experimental conditions as explained in section 5.2.4. The cell height was 3 µm for all simulations. The membrane intensity fraction was varied between 0.05 and 0.9 for cytoplasmic intensities of $F_{Cyto,\infty}$ of 10 kcps, 100 kcps, and 1000 kcps. Multiple traces (n = 1000) were simulated for each choice of parameters and analyzed analogous to the

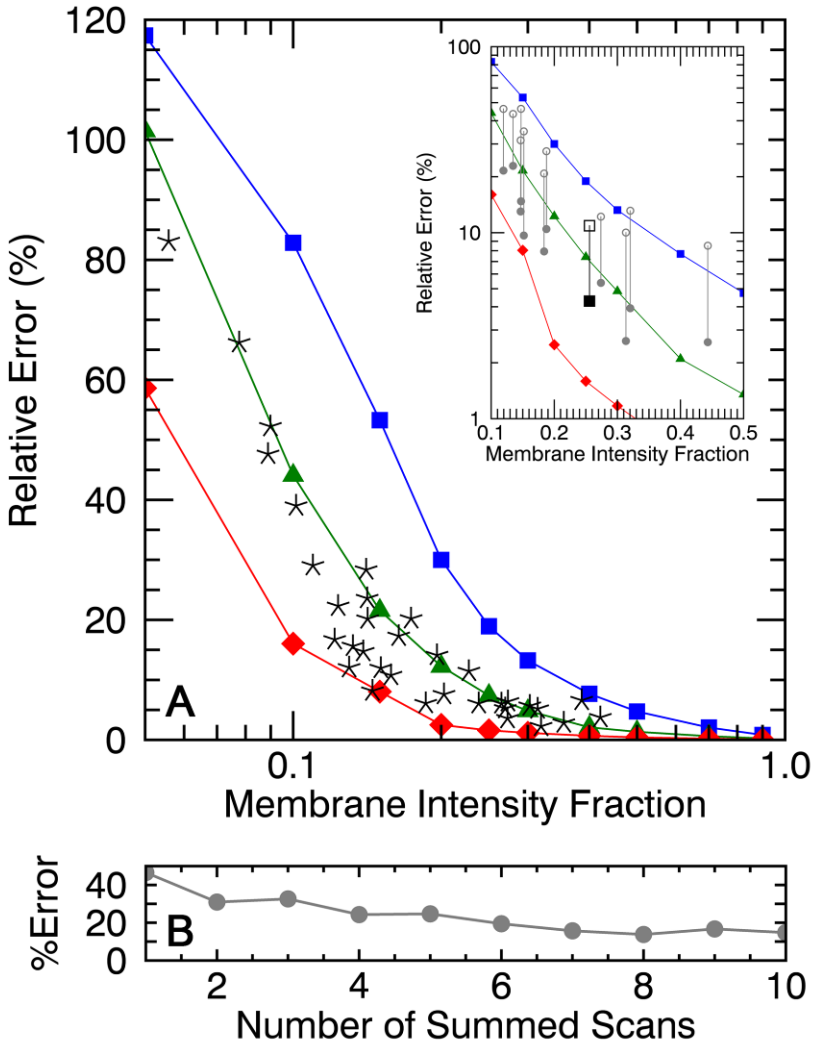

Figure 5.3 Resolvability of membrane intensity fractions.

(*A*) Relative error (*stars*) versus the membrane intensity fraction f_M. Each data point was determined from fits of 10 consecutive scans. All intensity profiles were taken from cells with cytoplasmic intensities $F_{cyto,\infty}$ between 100 and 1000 kcps. Relative error in f_M from simulated intensity profiles (n=1000) for $F_{cyto,\infty}$ = 10 kcps (*squares*), 100 kcps (*triangles*), 1000 kcps (*diamonds*). (*Inset*) Relative error versus mean of z-scan intensity profiles from cells with $F_{cyto,\infty}$ between 11 and 16 kcps. Relative error from individual scans (open circles) is reduced by summing groups of 10 scan profiles (*solid circles*). (*B*) Relative error in f_M as a function of the number of summed intensity profiles for one cell (*squares*) from the inset.

experimental data described above to determine the standard deviation of the membrane intensity fraction. The result of the simulations, plotted as lines with filled symbols in Figure 5.3A, demonstrate that higher intensities and higher membrane intensity fraction reduce the uncertainty. Our experimental results closely match the simulation results in that the experimental data are scattered between the simulation results for cytoplasmic intensities of $F_{Cyto,\infty}$ of 100 kcps and F_{Cyto} of 1000 kcps. This suggests that shot noise is the dominant factor shaping the experimental uncertainty. At lower membrane intensity fractions ($f_M \leq 0.1$) the uncertainty increases rapidly, which imposes a practical limit for resolving very small signal contributions from the membrane. Since the experimental and simulated results demonstrate the feasibility of resolving membrane intensity fractions ≥ 0.1 from z-scan intensity profiles, we limited our study to cells with $f_M \geq 0.1$.

5.3.3 Stability of cellular z-scan intensity profiles

The study of time-dependent changes in the membrane-bound population of cellular proteins requires a series of z-scans over a prolonged period of time. Any process that alters the binding conditions of the peripheral membrane protein will be reflected in a time-dependent evolution of the membrane intensity profile. The changes in the cytoplasmic and membrane-bound populations of the protein can be identified from analysis of the z-scan profiles provided that the instrument is stable and introduces no artifacts. We investigate the stability of our setup by performing a series of repeated z-scans through the same x-y position in a cell. By fitting the intensity profiles from the

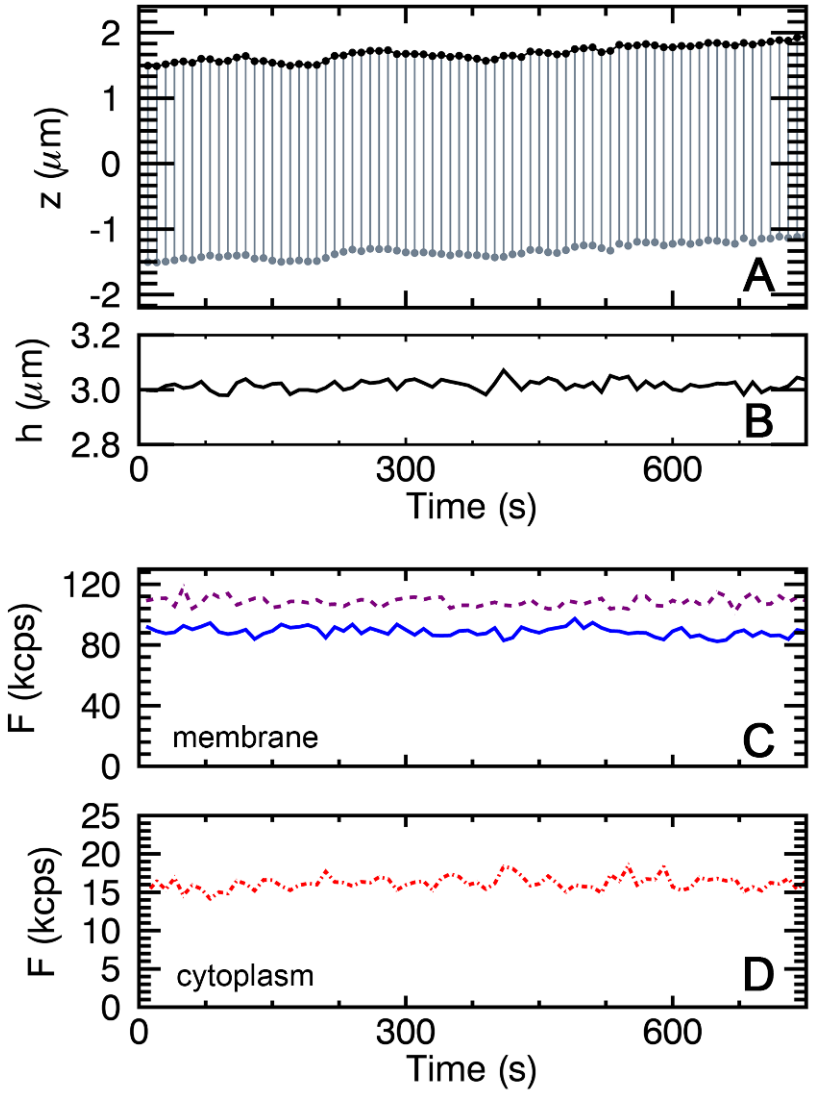

Figure 5.4 Repeated z-scans: EGFP-H-Ras.

Repeated z-scans performed at the same x-y position in an U2OS cell expressing EGFP-H-Ras are fit by Eq 5.6. (*A*) Top (*black circles*) and bottom (*shaded circles*) membrane position as a function of time show parallel movement with ~0.5 μm of z-drift over a period of 12 minutes. (*B*) Cell thickness (*solid line*) stays approximately constant. (*C*) Top (*dashed line*) and bottom (*solid line*) membrane intensity as a function of time is constant (F_{BM}=88.8 ± 3.1 kcps, F_{TM}=108.4 ± 3.1 kcps). (*D*) Cytoplasmic intensity (*dot-dashed line*) remains stable (F_{cyto}=16.2 ± 0.9 kcps).

repeated scans to Eq. 5.6, membrane movement, cell height changes, and instrument z-drift can be studied over time. Figure 5.4A shows the top and bottom membrane position of a U2OS cell expressing EGFP-H-Ras over a 750 s period. An offset was added to the data to place the midpoint of the cell initially at zero. The position of the top membrane, drifts by approximately 0.5 μm (standard deviation of 0.12 μm) in parallel with the position of the bottom membrane during the repeated scans. This parallel motion of the two cellular surfaces is indicative of focal drift in the instrument, while the cell height (Figure 5.4B), $h = z_T - z_B$, stays approximately fixed (standard deviation of 0.02 μm). The fastest drift rate estimated from Figure 5.4A is 10 nm/s, which is small enough to have a negligible influence on the shape of the intensity profile, because the PSF only has significant overlap with the cell for ~1s during the scan.

Despite drift and occasional changes in cell height, the fluorescence intensities determined from fits to Eq. 5.6 remain remarkably constant as demonstrated by Figure 5.4 C & D. The average membrane intensity fractions for the top and bottom membrane are $f_T = 0.87$ and $f_B = 0.85$ with a standard error of 1%. The experimental uncertainty agrees well with the simulations from Figure 5.3A, which predict an uncertainty of 1% for $F_{Cyto,\infty}$ =10 kcps for a membrane fraction of 0.9. Because we also collected intensity fluctuations, our experiments were capable of converting fluorescence intensities to concentrations. The relation $F_{Cyto,\infty} = \lambda c_{Cyto} V_\infty$ connects the cytoplasmic concentration and intensity. The PSF volume was calculated as explained in section 5.2.3and the brightness of the monomeric protein was determined as described in chapter 4 (51). Similarly, the surface concentration of the protein at the top and bottom membrane are

given by $F_T = \lambda \sigma_T A_0$ and $F_B = \lambda \sigma_B A_0$. Applying these relations we obtained σ_B = 1260 μm^{-2}, σ_T = 1530 μm^{-2} for Figure 5.4C and c_{Cyto} = 340 μm^{-3} for Figure 5.4D. The intensity variations over the measurement period of 750 s lead to a relative uncertainty of less than 5% for all concentrations.

The data and simulations illustrate that the uncertainty of determining membrane intensity fraction strongly depend on the fluorescence intensity (Figure 5.3A). Thus, quantifying small intensity fractions when the cellular protein concentration is low will be hampered by large uncertainties. Since shot noise appears to be the dominant noise limiting the resolvability of membrane intensity fractions, collecting more photons in the z-scan profile should reduce the uncertainty. Because cell height stays fixed over prolonged periods of time, this suggests the possibility of taking consecutive z-scans and aligning the individual z-scan intensity profiles by software to correct for offsets introduced by focal drift. The photon count signal of the aligned intensity profiles are then added up to create a summed profile with a larger signal, which is expected to result in a reduction in the uncertainty of the fit parameters. To test this procedure and facilitate the early detection of small membrane intensity fractions in cells with low cytoplasmic proteins concentrations, we selected cells with cytoplasmic intensities ranging from 11 to 16 kcps. We collected 100 z-scan intensity profiles from each cell and divided the scans into groups of *N*, which were aligned and summed. Each of the summed profile was fit to Eq. 5.6 and the average and standard deviation of the fitted membrane intensity fraction f_M were determined. The inset in Figure 5.3A shows the relative uncertainty in f_M of individual scans (*open circles*, N = 1) together with the uncertainty of the summed

intensity profiles (*solid circles*, $N = 10$). Summing 10 intensity profiles lead to an average reduction in the relative uncertainty of 2.8 with a standard deviation of 0.6. The decrease of the relative error with N is illustrated in Figure 5.3B for one of the data sets. The results are consistent with the expected $1/\sqrt{N}$ behavior and demonstrate the feasibility to improve the signal-to-noise ratio of dim samples by combining the signal from several fast z-scan intensity profiles.

5.3.4 Kinetic studies of peripheral membrane protein partitioning

Time-dependent changes in the distribution of a membrane-bound protein can be quantitatively characterized through a series of repeated z-scans. Here we study the PH domain of PLCδ which binds with high affinity to phosphatidylinositol 4,5-bisphosphate ($PI(4,5)P_2$) lipids at the plasma membrane (132). When fluorescently labeled, PH-PLCδ-EGFP maps the distribution of $PI(4,5)P_2$ within a cell and exhibits a z-dependent intensity profile with a prominent double peak. Ionomycin induces depletion of internal Ca^{2+} stores and stimulates store-operated Ca^{2+} entry, which raises the Ca^{2+} concentration in the cytoplasm (133). The increased Ca^{2+} concentration in turn activates PLC-mediated hydrolysis of $PI(4,5)P_2$ into diacylglycerol (DAG) and inositol triphosphate (IP_3) (134). This process leads to the displacement of PH-PLCδ-EGFP from the plasma membrane to the cytosol, because the hydrolysis depletes the membrane binding site of the protein (135).

We investigate the time-resolved distribution of PH-PLCδ-EGFP by performing a series of repeated z-scans through the same x-y position in a cell and fitting the intensity

profiles from the repeated scans to Eq. 5.6. Figure 5.5A shows the fluorescent intensities from the top membrane, bottom membrane, and cytoplasm over a period of 210 s within the cell. Ionomycin containing solution was added at the 60 s time point, and a dramatic redistribution of fluorescent intensities from the membrane to the cytosol was observed ~60 s after ionomycin treatment. In the cytoplasm the pre-treatment signal was ~100 kcps and post treatment the signal was ~700 kcps. At the membrane both signals decreased; for the top membrane the signal dropped from ~200 kcps to ~0 while the bottom membrane signal dropped from ~200 kcps to ~100 kcps. The fit of the z-scan profile to Eq. 5.6 also recovered the cell's height which destabilized upon treatment with ionomycin. This was particularly evident in cells expressing PH-PLCδ-EGFP where the time trace (Figure 5.5B) identified a reduction in cell height of 0.33 μm after ionomycin treatment. The change in height was calculated by comparing the average height from the interval between 0-60s to the average height in the interval from ~140-200 s. This loss of height was typical for PH-PLCδ-EGFP cells following addition of ionomycin and will be discussed in more detail later. The data further show that the delay between adding ionomycin and fluorescence response cannot be explained by slow mixing of the ionomycin solution with cell medium as demonstrated by the fluorescence intensity trace (Figure 5.5C) of Texas Red that was included with the ionomycin solution.

As a control, ionomycin solution was also added to cells expressing EGFP and cells expressing EGFP-H-Ras. The z-scans were fit to a slab model for EGFP and a delta-slab-delta model for EGFP-H-Ras. The fluorescence intensities of EGFP in the cytoplasm

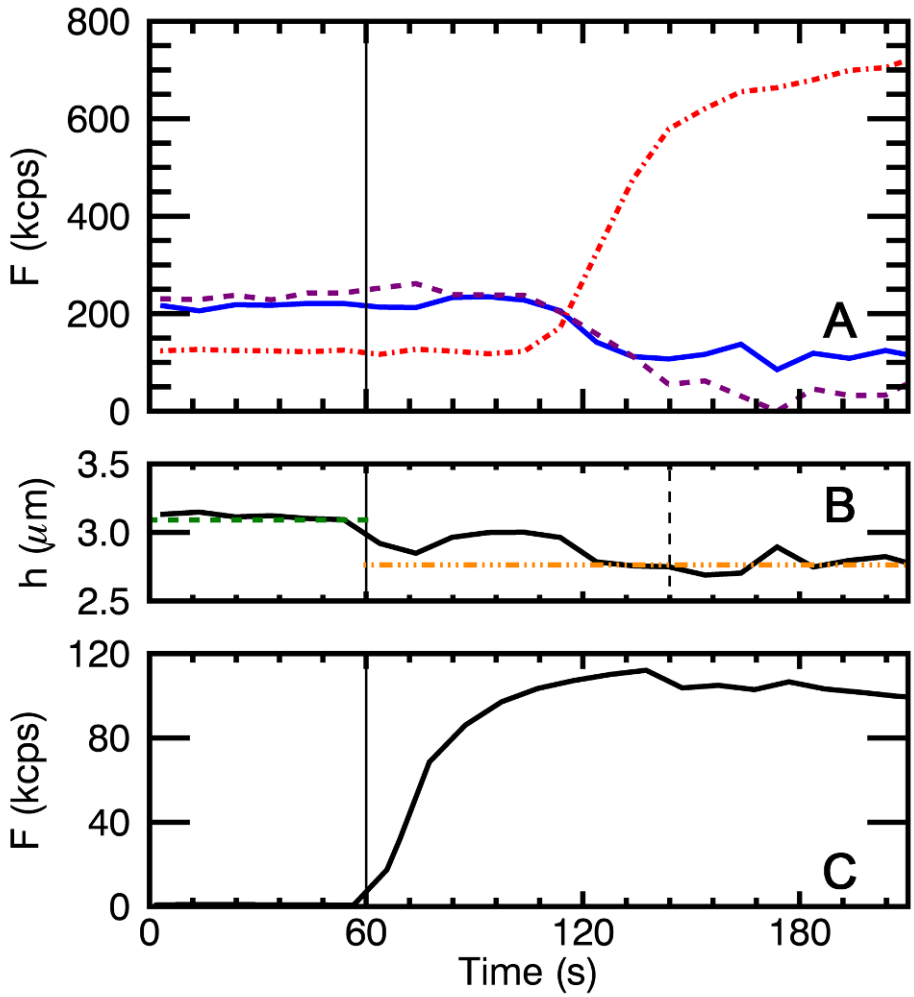

Figure 5.5 Time-resolved study of PH-PLCδ-EGFP.

Kinetics from repeated z-scans of an U2OS cell expressing PH-PLCδ-EGFP. (*A*) Top membrane (*dashed line*), bottom membrane (*solid line*), and cytoplasmic (*dotted-dashed line*) intensity as a function of time. Ionomycin solution was added at 60 s. (*B*) Cell height (*solid line*) as a function of time. Average height from 0-60 s (*dotted line*) and from 140-200 s (dotted-dashed line) shows a reduction of 0.34 μm. (*C*) Intensity time trace of Texas Red from the ionomycin solution.

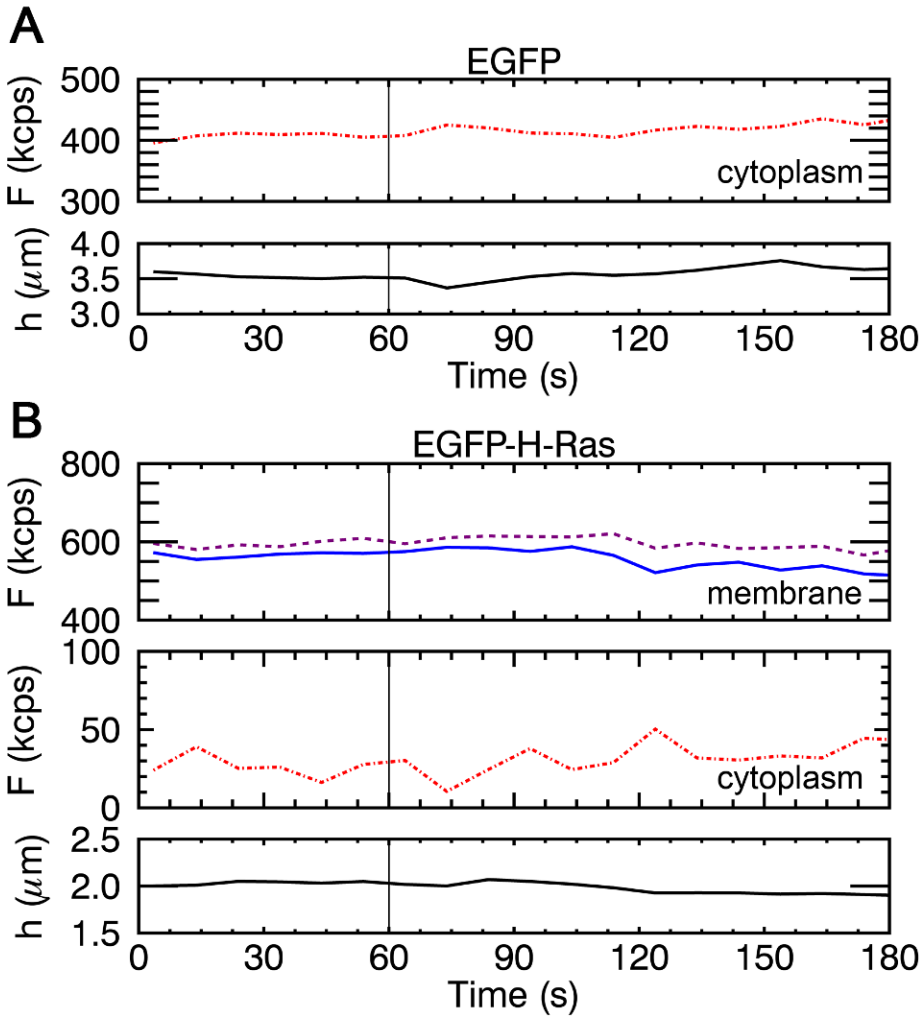

Figure 5.6 Time-resolved studies of EGFP and EGFP-H-Ras.

Kinetics from repeated z-scans of U2OS cells with ionomycin solution added at 60 s. (*A*) EGFP expressing cell with cytoplasmic intensity (*top panel*) and cell height (*bottom panel*) as a function of time. (*B*) EGFP-H-Ras expressing cell with intensity from top membrane (*top panel, dashed line*), bottom membrane (*top panel, solid line*), and cytoplasm (*middle panel, dotted-dashed line*). (*Bottom panel)* cell height.

as well as the cell height remained approximately constant before and after addition of ionomycin at t = 60 s (Figure 5.6A). Similarly for EGFP-H-Ras, we observed no significant change in cell height, the fluorescence at the membrane, and the fluorescence in the cytoplasm upon adding ionomycin (Figure 5.6B).

We used box and whisker plots to characterize the changes in cell height, cytoplasmic intensity and membrane intensity before and after treatment with ionomycin for all cells measured. The "pre" period represents 60 seconds before the addition of ionomycin. For PH-PLCδ-EGFP, the "post" period was defined to start when the redistribution of the intensity approached its final point and lasted for 60 seconds. PH-PLCδ-EGFP (10 cells) showed the largest change in cell height ($\Delta h = h_{post} - h_{pre}$), with a mean loss of -0.37 μm after ionomycin treatment (Figure 5.7A). Conversely, both EGFP (10 cells) and EGFP-H-Ras (8 cells) only changed their average cell height slightly (Figure 5.7A). The distributions of both are scattered around zero with average values of -0.14 μm for EGFP-H-Ras and -0.10 μm for EGFP. Figure 5.7B displays the cytosolic intensity ratio of post- to pre-treatment with ionomycin. Both EGPF and EGFP-H-Ras have ratios close to unity (mean of 1.04 for EGFP and 1.07 for EGFP-H-Ras), which demonstrates the absence of a strong ionomycin-specific effect, in agreement with the data of Figure 5.6. The cytosolic intensity ratio of PH-PLCδ-EGFP has a mean value of 5.13 which corresponds to a five-fold increase in the cytosolic intensity following the addition of ionomycin. The membrane intensity ratio of post-ionomycin to pre-ionomycin values is shown in Figure 5.7C. Because EGFP-H-Ras has an intensity ratio of ~1 (mean

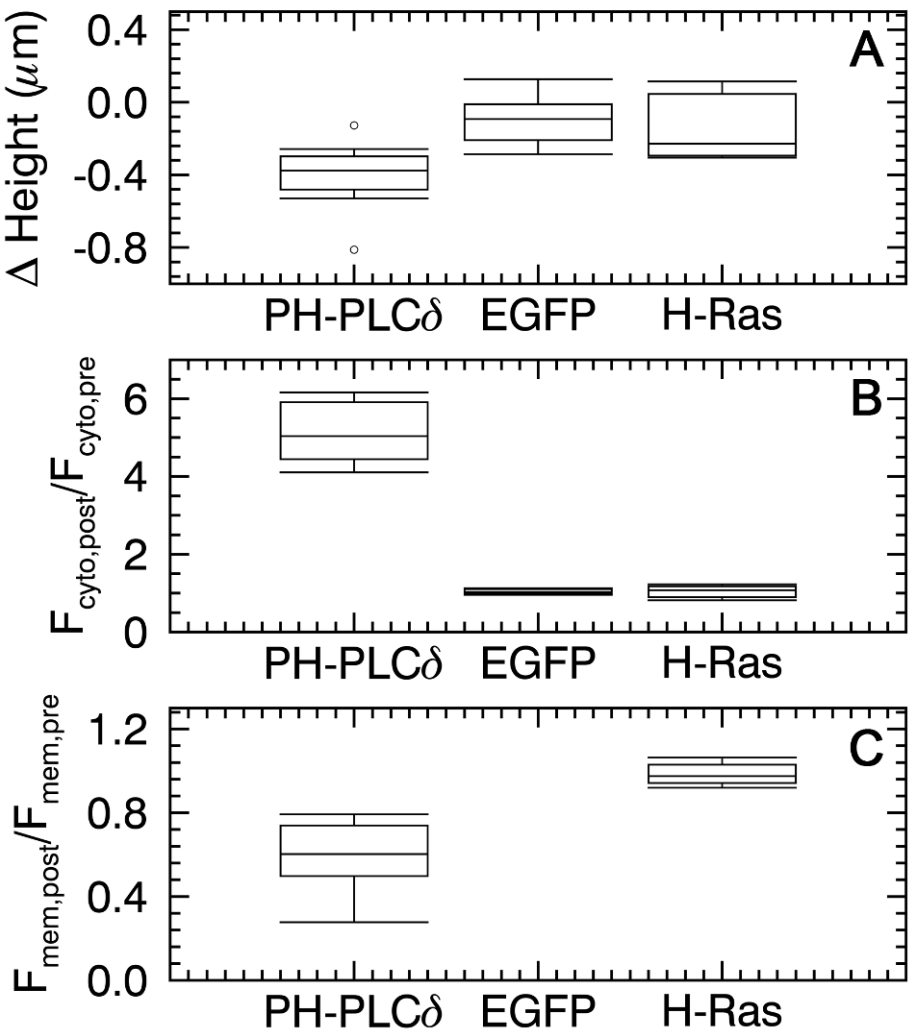

Figure 5.7 Summary of time-resolved studies.

Box plots of changes in cell height and intensity between pre- and post-ionomycin treatment of U2OS cells expressing PH-PLCδ-EGFP (n = 10), EGFP (n = 10), or EGFP-H-Ras (n =8). (*A*) Difference in cell height $\Delta h = h_{pre} - h_{post}$. (mean of –0.37 μm for PH-PLCδ-EGFP, –0.10 μm for EGFP, –0.14 μm for EGFP-H-Ras). (*B*) Cytoplasmic intensity ratio (F_{post} / F_{pre}) with a mean values of 5.13 for PH-PLCδ-EGFP, 1.04 for EGFP, 1.07 for EGFP-H-Ras. (*C*) Membrane intensity ratio (F_{post} / F_{pre}) with mean values of 0.60 for PH-PLCδ-EGFP and 0.98 for EGFP-H-Ras.

of 0.98), the distribution of proteins at the membrane is essentially not affected by the ionomycin treatment. PH-PLCδ-EGFP has a membrane intensity ratio centered at 0.60 reflecting the redistribution of PH-PLCδ-EGFP proteins from the membrane to the cytoplasm.

Although changes in the EGFP-H-Ras signal with ionomycin treatment were relatively small, we observed a measurable difference in the cytoplasmic ($\Delta F_{cyto} = F_{cyto,post} - F_{cyto,pre}$) and membrane-bound ($\Delta F_{mem} = F_{mem,pre} - F_{mem,post}$) intensity for each treated cell. The difference ΔF_{mem} was calculated using the average of both membranes. We next compared the changes in the observed cytoplasmic and membrane-associated intensity by graphing the ratio $\Delta F_{cyto} / \Delta F_{mem}$ for all of the HRas-EGFP cells studied (Figure 5.8). The median of the ratio is close to one for the majority of cells (median of 0.58 and mean of 0.89) and is relatively stable considering the small observed signal.

In contrast to HRas-EGFP the redistribution of PH-PLCδ-EGFP from the membrane to the cytoplasm resulted in a large change in the cytoplasmic intensity coupled with a smaller change in the intensity at the membrane (Figure 5.5). The ratio of the cytoplasmic to membrane-associated intensity difference ($\Delta F_{cyto} / \Delta F_{mem}$) for all of the PH-PLCδ-EGFP cells studied (Figure 5.8) varied from ~3 to 15 with a mean of 8.4, which is considerably larger than observed for HRas-EGFP.

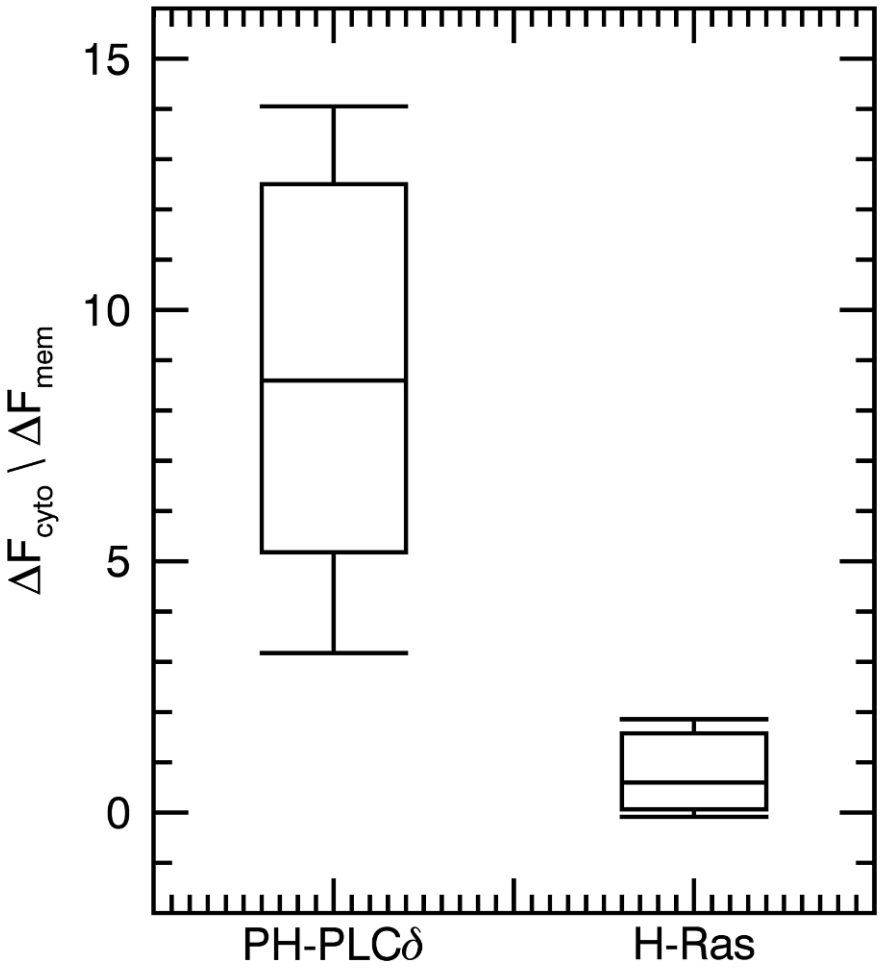

Figure 5.8 Summary of fluorescence redistribution.

Box plots of the ratio of $F_{cyto,post} - F_{cyto,pre}$ and $F_{mem,pre} - F_{mem,post}$ for ionomycin treated U2OS cells expressing PH-PLCδ-EGFP (n = 10) and EGFP-H-Ras (n =8).

As described earlier, the fluorescence intensity is connected to brightness, concentration and PSF volume or area, which leads to $\Delta F_{cyto} = \lambda \left(c_{cyto,post} - c_{cyto,pre} \right) V_{\infty}$ and $\Delta F_{mem} = \lambda \left(\sigma_{mem,pre} - \sigma_{mem,post} \right) A_0$. Thus, the ratio of the intensity difference relates to concentration changes in the cytoplasm and at the membrane along the scan path,

$$\frac{\Delta F_{cyto}}{\Delta F_{mem}} = \frac{c_{cyto,post} - c_{cyto,pre}}{\sigma_{mem,pre} - \sigma_{mem,post}} \frac{V_{\infty}}{A_0}. \tag{5.8}$$

If we assume that the protein is approximately uniformly distributed inside the cell and at the membrane, then the intensity ratio can be connected to the plasma membrane area S_{mem} and the cell volume V_{cell}. The number of PH-PLCδ-EGFP or EGFP-H-Ras molecules before and after ionomycin treatment has to be conserved, which implies

$$\sigma_{mem,post} S_{mem} + c_{cyto,post} V_{cell} = \sigma_{mem,pre} S_{mem} + c_{cyto,pre} V_{cell}. \tag{5.9}$$

Inserting Eq. 5.9 into Eq. 5.8 leads to

$$\frac{\Delta F_{cyto}}{\Delta F_{mem}} = \frac{S_{mem}}{V_{cell}} \frac{V_{\infty}}{A_0}. \tag{5.10}$$

The equation states that the intensity ratio is directly related to the ratio of the membrane surface area S_{mem} over the cell volume V_{cell} provided the protein is uniformly distributed. When accounting for the PSF volume and area of the experimental setup ($A_0 = 0.18\ \mu m^2$ and $V_{\infty} = 0.24\ \mu m^3$) the average of $\Delta F_{cyto} / \Delta F_{mem}$ predicts a surface to volume ratio (S_{mem} / V_{cell}) of 6.7 μm^{-1} for PH-PLCδ-EGFP and 0.7 μm^{-1} for EGFP-H-Ras. These two predictions differ widely, which will be discussed later in more detail.

5.4 Discussion

Distinguishing cytoplasmic and membrane-bound protein populations relies on the accurate breakdown of the z-scan intensity profile into its individual components. A prerequisite for this deconvolution is an accurate PSF model and parameterization. It is crucial to test the selected PSF model on experimental z-scan traces with well-defined geometries. The delta-layer is optimal to test the PSF model, because it directly probes the radially integrated PSF (RIPSF) profile (Figure 5.1F). A second important test model is the semi-infinite layer (Figure 5.1D). The same PSF parameters that describe the delta layer also need to model the z-scan intensity profile of the semi-infinite layer. Because the semi-infinite layer probes the PSF deeper into the solution than the delta layer, depth-changes in the PSF, such as those caused by spherical aberrations, are easily noticed. There should be no deviation between the model and the experimental intensity profile, at least to a depth that covers the size of the object to be scanned, which in the case of adherent cells is a few micrometers. A PSF model that passes the above tests is viable for z-scan FPD analysis. We previously demonstrated that the modified Gaussian-Lorentzian PSF model (51, 76) is suitable for our two-photon instruments and identified the PSF parameters.

Identifying the cytoplasmic and membrane-bound intensities is based on fitting of the z-scan intensity profile. Reliable extraction of the fit parameters requires the correct assignment of measurement uncertainties in addition to selecting an accurate PSF model. We calculated the uncertainty based on shot noise, which resulted in fits with reduced chi-squared values of ~1 for the experimental intensity traces. This result implies that

shot noise due to the photon detection process is the dominant source of noise of experimental z-scan intensity traces, which is further corroborated by the simulated z-scan intensity profiles that give rise to uncertainties in the fractional membrane intensity that closely match the experimental data (Figure 5.3A).

Extracting the intensities from the membrane and cytoplasm relies on the shape of the intensity profile. Thus, the cell at the scan location has to be sufficiently thick to generate a profile with the two membrane intensity peaks readily distinguishable. As a rule of thumb the thickness should be at least twice the axial beam waist z_0 of the PSF, which implies a minimum thickness of ~2 μm for our setup. This condition was satisfied for all cell measurements presented in this study. Furthermore, the amplitude of the membrane intensity peaks needs to be strong enough to measurably influence the shape of the intensity profile. While peaks are no longer visible when the membrane intensity fraction falls below 25%, quantitative analysis of the z-scan intensity profile extends to lower membrane intensity fractions. The experiments and simulation identify a practical lower limit for the membrane intensity fractions of ~0.1 (Figure 5.3A).

The uncertainty in the fit parameters increases rapidly at low membrane intensity fractions. Collecting more photons during the scan reduces the fit uncertainty, but increasing laser power is limited by the onset of photobleaching of the sample, which distorts the intensity profile. Slowing down the z-scan speed would collect more photons, but this approach requires a very stable instrument and may not be an option in many cases. Our instrument requires relatively fast scans to counteract the distorting influence of focal drift. Measurements over several months identified a maximum drift rate of

~10 nm/s. In this study we collected a complete intensity profile in 5 s (half a scan period), which is sufficiently fast to render the influence of drift negligible. While we observed slow changes in cell height in some cases, the cell thickness at the scan location is usually remarkably constant for prolonged periods of time. A stable cell thickness provides an alternative to improve the signal-to-noise ratio of the measurement that does not rely on a slow scan speed. We demonstrated that summing the signal from repeated, fast z-scans is feasible and results in a lower uncertainty in the fit parameters. Together, these results establish that quantitative z-scan analysis can be performed on a regular microscope without the need for specialized hardware that corrects focus drift.

FPD analysis of the z-scan intensity determines the intensity from each fluorescent layer and the separation between layers. The scanning rate used to collect fluorescence intensity profiles is fast enough that the layer intensity and separation can be applied to time-resolved studies of protein binding to the membrane, as demonstrated by the data in Figure 5.5. Furthermore, it is possible to relate intensities to concentration through the use of a conversion factor from an independent control experiment. In our case, we determined the brightness λ_{EGFP} of monomeric EGFP in an independent cell experiment. The protein concentration in the cytoplasm and at the membrane is calculated from the intensities and the brightness as explained in the results section. Because λ_{EGFP} corresponds to the brightness of monomeric EGFP, the calculated concentration is expressed in terms of monomer. In contrast to the z-scan intensity profile, z-scan FFS is a slow technique which is not suited for time-resolved studies because the additional FFS measurements lead to data acquisition times approaching

100 s. Thus, z-scan FFS measurements only have an advantage over z-scan FPD, if the oligomeric state of proteins at the plasma membrane and in the cytoplasm needs to be identified.

In this chapter we applied z-scan FPD with a time resolution of 5 s to quantify the redistribution of PH-PLCδ-EGFP from the plasma membrane to the cytoplasm upon ionomycin treatment. Since the time scale of the cellular response to signaling events typically is longer than a minute (136), a resolution of 5 s should be sufficient in most cases. We monitored the appearance of Texas Red fluorescence to account for the variability in the mixing time upon adding ionomycin solution (Figure 5.5C), which served to identify the exact time point of ionomycin delivery to the cell. The experiment recorded a time delay between ionomycin delivery and the onset of the fluorescence intensity redistribution (Figure 5.5). The delay of ~30s is consistent with studies of Ca^{2+} cell signaling which showed that Ca^{2+} reached maximum levels 30 - 60s after ionomycin treatment (133, 137, 138).

The membrane translocation kinetics of peripheral membrane proteins like PH-PLCδ-EGFP have been studied by fluorescence imaging methods. Initial studies used confocal imaging to show the redistribution of PH-PLCδ-EGFP from the membrane to the cytoplasm after ionomycin treatment or PFA receptor stimulation (29, 30). Both studies used the intensity profile from a line segment of the image to quantify the relative change in fluorescence around the membrane region over time. While this captured the kinetics of the process, the profile itself provides no direct measure for separating cytoplasmic and membrane-bound components. Loew and colleagues noted another

problem with intensity profiles linked to membrane movement. They imaged PH-PLCδ-EGFP and observed bradykinin stimulation-induced cell shape changes and membrane movement (31). To address this issue, a region of interest including membrane and cytoplasm was selected, followed by a thresholding step to segment the membrane region. The average intensity above the threshold was used to estimate the intensity at the membrane (31). While this approach was judged to avoid issues associated with membrane movement, the local cell geometry within the region of interest and a precise PSF model were not taken into account, which prevented a truly quantitative separation of membrane-associated and cytoplasmic fluorescence. Z-scan FPD overcomes these shortcomings and achieves quantitative separation of the intensity profile by analytically accounting for cell geometry and PSF shape.

The inherent quantitative nature of z-scan FPD analysis allowed us to measure membrane movement that had been mentioned as a concern but was not quantified (31). PH-PLCδ-EGFP showed a significant reduction in cell height upon ionomycin treatment (Figure 5.7A). Control experiments on cells expressing EGFP and EGFP-H-Ras revealed a negligible effect of ionomycin on cell height. Because PH-PLCδ-EGFP lacks enzymatic activity of its own, the results imply that the observed change in cell height was specific to the dissociation of PH-PLCδ-EGFP from the plasma membrane and that the interaction of the peripheral membrane protein with the lipid had an influence on the plasma membrane and the cell shape. This observation agrees with other studies that have pointed out that protein-membrane interactions can change properties of the membrane itself (126–129), as well as, modulate the adhesion strength between the cytoskeleton and

membrane lipids (139). For example, PH-PLCδ-EGFP has been shown to induce positive membrane curvature in model membranes when it binds to $PI(4,5)P_2$ lipids (140). While the previous study was performed *ex situ*, our results demonstrate that PH-PLCδ-EGFP binding also affects the membrane inside a living cell. In addition, we observed a slight asymmetry in the response of the top and bottom membrane upon ionomycin treatment. While the fluorescence intensity from PH-PLCδ-EGFP associated with either membrane was approximately identical before treatment, the top membrane showed consistently a more pronounced decrease in fluorescent intensity than the bottom membrane following ionomycin treatment (Figure 5.5A). The cause for this difference is currently not known and will require further study. However, since the rigidity of the glass substrate can alter the bottom membrane's properties (141, 142), the membrane-glass attachment might contribute to the observed effect. Z-scan FPD provides the means to quantitatively study differences at the top and bottom membrane, which is not readily accessible by other fluorescence techniques. The influence of substrate rigidity can be explored in future experiments by coating the glass coverslips in order to change the substrate stiffness.

An estimate of the surface area to volume (SA/V) ratio of U2OS cells based on a simple model of the cell as a cylinder with a cross-sectional area of ~400 μm^2 and a volume of ~1pl (143) leads to a value on the order of 1 μm^{-1}. This estimate predicts that changes in fluorescence at the plasma membrane and in the cytoplasm due to translocation results in a ratio $\Delta F_{cyto} / \Delta F_{mem}$ of ~1 (Eq.5.10) provided that the concentration at the membrane and in the cytoplasm are uniform. As mentioned above, the SA/V ratio for EGFP-H-Ras is 0.7 μm^{-1} which is in good agreement with the above

estimate, but for PH-PLCδ-EGFP we arrived at a ratio (SA/V=6.7 μm^{-1}) that is inconsistent with the model. The ratio is significantly larger than the expected value which indicates the appearance of more protein in the cytoplasm than is expected from the loss at the plasma membrane. This outcome could be achieved by the additional release of PH-PLCδ-EGFP from internal membranes like the golgi, but studies have found very little association of PH-PLCδ-EGFP with internal membranes (144, 145). Another source that could account for the large ratio is the presence of plasma membrane areas outside the z-scan location that carry a higher protein concentration. It has been shown that $PI(4,5)P_2$ and PH-PLCδ-EGFP are more highly concentrated in membrane ruffles (144, 146–149) compared to other regions of the membrane. The ruffles of U2OS cells are located closer to the periphery of the cell, a region that was not sampled in our study, because it is too thin for z-scan FPD analysis. Thus, a likely explanation for the high ratio is the release of additional PH-PLCδ-EGFP located at membrane ruffles.

In summary, z-scan FPD analysis introduces a method to decompose the fluorescence contributions from the cytoplasm and membrane of a peripheral membrane protein in the living cell. Only three elements are required, the fluorescent intensity profile along the axial dimension of the cell, a well characterized point spread function, and a model of the cell geometry. Intensities both at the membrane and in the cytoplasm are readily converted into concentrations by including a brightness calibration measurement taken in EGFP expressing cells. The quantitative nature of z-scan FPD, as demonstrated by our results, opens new opportunities for investigating peripheral membrane proteins in cells. It will be interesting to explore combining this method with

lateral scanning in future development work. Such an extension of the technique would allow probing lateral heterogeneity of protein density at the membrane, such as the presence of punctate structures, while still retaining the ability to quantitatively distinguish fluorescent intensities contributions from cytoplasmic and membrane layers.

6. In situ quantification of protein binding to the plasma membrane

This chapter presents a fluorescence-based assay that allows for direct measurement of protein binding to the plasma membrane inside living cells. An axial scan through the cell generates a fluorescence intensity profile that is analyzed to determine the membrane-bound and cytoplasmic concentrations of a peripheral membrane protein labeled by EGFP. The membrane binding curve is constructed by mapping those concentrations for a population of cells with a wide range of protein expression levels, and a fit of the binding curve determines the number of binding sites and the dissociation coefficient. We experimentally verified the technique, using myosin-1C-EGFP as a model system and fit its binding curve. Furthermore, we studied the protein-lipid interactions of the membrane binding domains from lactadherin and phospholipase C-delta 1 to evaluate the feasibility of using competition binding experiments to identify specific lipid-protein interactions in living cells. Finally, we applied the technique to determine the lipid specificity, the number of binding sites, and the dissociation coefficient of membrane binding for the Gag matrix domain of Human T-lymphotropic virus Type 1, which provides insight into early assembly steps of the retrovirus.

6.1 Introduction

The attachment of peripheral membrane proteins to lipid bilayers plays a critical role in many cellular functions, such as lipid metabolism, cytoskeletal structure, vesicle

trafficking, signal transduction, cell differentiation, growth, and apoptosis (8–10). Since membrane binding is crucial for the cellular function of these proteins, characterization of the membrane binding curve is a prerequisite for understanding the function and regulation of peripheral membrane proteins. As we noted in chapter 1, most studies of protein–lipid interactions are based on in vitro assays with membranes in the form of lipid vesicles, supported lipid bilayers, or lipid monolayers (21–23). In some cases isolated membranes have been used to go beyond simple lipid membranes (150, 151). However, these traditional assays study the protein and membrane ex situ, and are unable to reproduce the native conditions that give rise to the complex organization and dynamic behavior of cellular membranes. Thus, a technique that directly studies the membrane binding curve of proteins in living cells is highly desirable, not only to validate previous ex situ results, but also to explore the binding process in its natural environment.

This chapter describes a method for measuring the binding of a fluorescently labeled protein with the plasma membrane of a living cell. The technique utilizes an axial scan through the cell to generate a z-scan fluorescence intensity profile. The intensity profile is deconvolved into its cytoplasmic and membrane-bound fluorescence contributions by accounting for the local cell height and the PSF of the instrument. The membrane binding curve is generated from the deconvolved cytoplasmic and membrane intensity contributions for a population of cells covering a sufficiently wide range of protein expression levels. We further converted fluorescence intensities into concentrations in the cytoplasm and at the membrane by applying the brightness of the fluorescent label EGFP. Information about the binding affinity and the number of binding

sites was recovered from a fit of the experimental data with a Langmuir isotherm. Moreover, competition binding experiments with different peripheral membrane proteins provided information about specific protein-lipid interactions at the plasma membrane.

Our z-scan FPD approach, which we introduced in chapter 5, is related to z-scan FFS and earlier work by Hof and coworkers (46). However, unlike z-scan FFS (51, 76) of chapter 4, which characterizes the axial dependence of intensity fluctuations, z-scan FPD focuses specifically on information contained within the axial fluorescence intensity profile to generate the experimental binding curve. We applied z-scan FPD to investigate the interaction of myosin-1C with the plasma membrane, generated the experimental membrane binding curves, and determined its binding parameters. We also performed binding experiments with a variety of peripheral membrane proteins with known lipid targets to demonstrate the feasibility of competitive binding assays in the cell. Finally we applied our technique to study the membrane interactions of the matrix domain of HTLV-1 Gag. We previously observed that the Gag polyprotein and matrix (MA), its membrane-binding domain, of HTLV-1 interact with the plasma membrane at low cytoplasmic concentrations, which is in stark contrast with the corresponding proteins of HIV-1 (51, 107, 108). Here we expand our investigation of HTLV-1 virus assembly by characterizing the membrane binding curve for the MA domain of HTLV-1 Gag and the lipid-specificity of the interaction.

6.2 Materials and methods

6.2.1 Experimental setup

Experiments were carried out on a modified two-photon microscope, as described in chapter 2. The experimental protocols for data collection and z-scanning are described in section 4.2.1 of chapter 4.

6.2.2 Sample preparation and plasmid construction

The pEGFP-C1 and pEGFP-N1 plasmids were purchased from Clontech (Mountainview, CA) and the mCherry-C1 plasmid has been previous described (131). The EGFP-H-Ras plasmid was a gift from Dr. Phillips (New York University School of Medicine). The Myosin1C-EGFP (Myo1C-EGFP) plasmid and the EGFP labeled PH domain of Phospholipase C-delta (EGFP-PLCδ-PH) plasmid were gifts from Dr. Albanesi (University of Texas-Southwestern). The EGFP labeled C2 domain of lactadherin (Lact-C2-EGFP) plasmid was purchased from addgene (Plasmid 22852). The Lact-C2-mCh plasmid was sub-cloned from the Lact-C2-EGFP plasmid into an mCherry-c1 backbone. The miniGAP-EGFP plasmid (the first 10AA of GAP43) was a gift from Dr. Digman (UC-Irvine). The miniGAP-mCh plasmid was cloned from miniGAP-EGFP and amplified by PCR with a 5' primer that encodes an *XhoI* restriction site and a 3' primer that encodes an *EcoRI* site. The HTLV-1 MA-EGFP plasmid has been previously described (51). All sequences were verified by automatic sequencing.

All cellular studies were performed using transiently transfected U2OS cells that were obtained from ATCC (Manassas, VA) and maintained in 10% fetal bovine serum

(Hycolone Laboratories, Logan, UT) and DMEM medium. Cells were subcultered in eight-well coverglass chamber slides (Nalge Nunc International, Rochester, NY) 12 hours before transfection. Transient transfections were carried out 24 hours prior to measurement using GeneJet (Thermo Scientific, Pittsburgh, PA) according to the manufacturer's instructions. Immediately before measurement, the growth medium was replaced with Dulbecco's phosphate-buffered saline (PBS) with calcium and magnesium (Biowhittaker, Walkerville, MD). For binding competition studies, cotransfections were performed with the two plasmid types mixed together at a given mole ratio prior to adding GeneJet. Specifically, pLact-C2-EGFP: pLact-C2-mCh was mixed at a 1:3 ratio, while for all other competition experiments plasmids were mixed at a 1:6 (EGFP labeled : mCh labeled) ratio. During measurement, the fluorescence intensity ratio of the green and red detection channel was used to select cells that express both proteins at a concentration ratio that matched or exceeded the plasmid ratio (50, 131). This selection ensured that each measured cell contains a sufficient excess of the competitor over the probed protein.

6.2.3 z-scan calibration of PSF

As discussed in chapter 2, the point spread function (PSF) for our two-photon microscope is well-approximated by the mGL-PSF,

$$PSF\left(\rho,\zeta\right)=\left(\frac{z_0^2}{z_R^2+\zeta^2}\right)^{(1+y)}\exp\left(-\frac{4z_R^2}{w_0^2}\frac{\rho^2}{z_R^2+\zeta^2}\right) \tag{6.1}$$

as originally described by Macdonald et al. (76). The radial and axial beam waist are characterized by w_0 and z_R. The *y* parameter adjusts the axial decay of the PSF while

maintaining a Gaussian cross section. The PSF parameters were determined by a z-scan calibration procedure as previously reported in section 4.2.4, which provided values of z_R = 1.02 ± 0.1 μm, y = 2.20 ± 0.3, and w_0 =0.47 ± 0.05 μm. The mGL-PSF volume is determined by e$V_\infty = \left(\frac{1}{4}\pi w_0^2 z_R\right)\frac{\sqrt{\pi}\,\Gamma\left(y-\frac{1}{2}\right)}{\Gamma(y)}$ and the cross-sectional area at the center of the PSF is given by $A_0 = \frac{\pi w_0^2}{4}$ (76).

6.2.4 z-scan intensity profile

As noted in chapter 5, the modeling of the z-scan intensity profile is based on the radially integrated PSF given by $\mathrm{RIPSF}(\zeta) = \int_0^\infty \mathrm{PSF}(\rho,\zeta)\,2\pi\rho\,d\rho$. It is convenient to use the radially integrated PSF to define a scaled volume function $\tilde{v}_V(z; z_B, z_T) = \frac{1}{V_\infty}\int_{z_B - z}^{z_T - z} \mathrm{RIPSF}(\zeta)\,d\zeta$ and a scaled area function $\tilde{v}_A(z; z_M) = \frac{1}{A_0}\mathrm{RIPSF}(z_M - z)$ (76). The z-scan fluorescence intensity profile $F(z)$ can be represented using the scaled volume and scaled area functions. For a cytoplasmic protein with the top and bottom membrane located at z_B and z_T the intensity profile is given by $F(z) = F_0\,\tilde{v}_V(z; z_B, z_T)$, while the intensity profile of a protein bound to a membrane located at z_M is given by $F(z) = F_0\,\tilde{v}_A(z; z_M)$ (51, 76).

Calculating the RIPSF function for the mGL-PSF described by Eq. 6.1 yields $\mathrm{RIPSF}(z) = \frac{\pi w_0^2}{4}\left(1 + (z/z_R)^2\right)^{-y}$. Evaluating the scaled volume function for the mGL-PSF leads to (76)

$$\tilde{v}_V(z; z_B, z_T) = \frac{\Gamma(y)}{\sqrt{\pi}\,\Gamma\left(y - \frac{1}{2}\right)}\left(\Psi\left(y, \frac{z_T - z}{z_R}\right) - \Psi\left(y, \frac{z_B - z}{z_R}\right)\right), \tag{6.2}$$

with $\Psi(y, x) = {}_2F_1\left(1/2, y, 3/2; -x^2\right)x$ and ${}_2F_1(a, b, c; x)$ represents the hypergeometric function. The scaled area function is given by

$$\tilde{v}_A(z, z_M) = \left(1 + \left(\frac{z_M - z}{z_R}\right)^2\right)^{-y}. \tag{6.3}$$

The scaled volume and area function were implemented in IDL 8.3 (Research Systems, Boulder, CO) for data analysis.

6.2.5 z-scan data analysis

The experimental protocol used for rebinning and fitting z-scan photon counts is described in Section 4.2.6. In addition, traditional brightness measurements were carried out in the thick cytoplasmic sections of 10-20 cells expressing EGFP as previously described in chapter 4 (51, 76). The average brightness λ from this calibration experiment was computed (70, 117) and served as the monomeric brightness value to convert intensities into concentrations.

6.3 Results

6.3.1 z-scan intensity profile of peripheral membrane proteins

A scan of the excitation spot along the z-axis of a cell records the fluorescence intensity profile $F(z)$ of the labeled protein. The intensity profile of a protein found at the plasma membrane and in the cytoplasm contains the signal contributions from three distinct cellular layers. The first layer is given by the bottom plasma membrane located at z_B, followed by a cytoplasmic layer and the top plasma membrane located at z_T. Once again, we introduce the delta-slab-delta fluorescence intensity profile of this geometry,

$$F_{dsd}(z) = F_B\,\tilde{\nu}_A(z; z_B) + F_{Cyto,\infty}\tilde{\nu}_V(z; z_B, z_T) + F_T\,\tilde{\nu}_A(z; z_T), \tag{6.4}$$

with F_B and F_T being the maximum fluorescence intensity at the membrane layers and $F_{Cyto,\infty}$ representing the limiting intensity of a thick cytoplasmic layer. The scaled volume $\tilde{\nu}_V$ and area $\tilde{\nu}_A$ function are defined by Eqs. 6.2 and 6.3.

We measured z-scan intensity profiles from U2OS cells expressing Myo1C-EGFP. The panels of Figure 6.1 display intensity profiles taken from two cells that differ in their protein expression level. Each experimental intensity profile (*solid line*) was fit to Eq. 6.4 to isolate the fluorescence contributions from each membrane (*dotted line*) and from the cytoplasm (*dotted-dashed line*), which are represented by the three terms of Eq. 6.4. The sum of these three terms determines the fitted z-scan intensity profile (*shaded line*). The relative contributions to the intensity profile from membrane-bound and cytosolic protein differ significantly for the two cells. Deconvolving the intensity

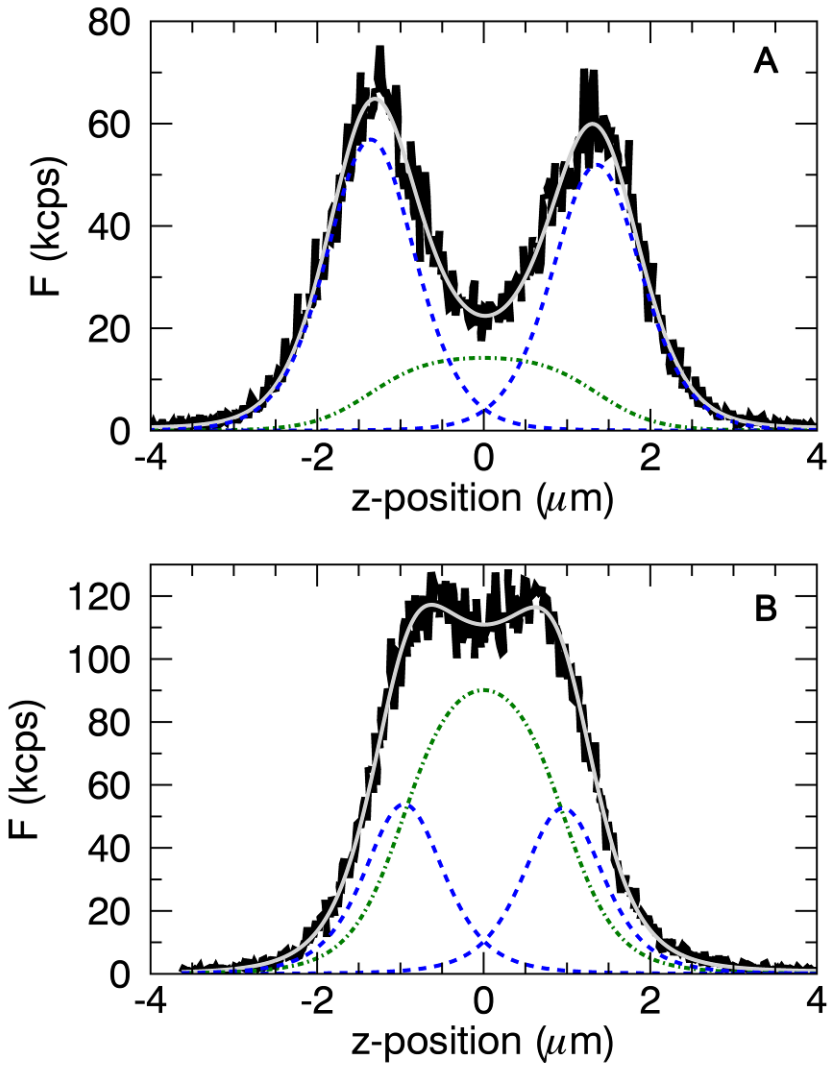

Figure 6.1 Myo1C-EGFP z-scan fluorescence profiles.

Z-scan intensity profile (*solid line*) for Myo1C-EGFP in two U2OS cells. The fit (*shaded line*) to Eq. 6.4 together with the membrane intensity components (dashed lines) and cytoplasmic component (*dotted-dashed line*). (*A*) Profile from a cell with a low cytoplasmic intensity and fit (χ^2_{red} =1.4, $F_{Cyto,\infty}$ =14.8 kcps, F_T =51.9 kcps, F_B =56.9 kcps). (*B*) Profile from a cell with a high cytoplasmic intensity and fit (χ^2_{red} =1.5, $F_{Cyto,\infty}$ = 103 kcps, F_T = 52.6 kcps, F_B = 53.9 kcps).

profile into its components allowed us to quantify these differences. We will follow this approach in the rest of the chapter to generate a membrane binding curve by analyzing intensity profiles from a population cells with different protein expression levels.

We expect the fluorescence intensity values to stay constant if the binding process of the peripheral membrane protein is at equilibrium. As a control we performed repeated z-scans on cells expressing H-Ras-EGFP over extended time periods. Each z-scan is fit by Eq. 6.4 to identify the cell height and the fluorescence intensities in each of the three layers as illustrated in Figure 6.2. The top (Figure 6.2A, *dashed line*) and bottom (*solid line*) membrane intensity, as well as the cytosolic intensity (Figure 6.2B, *dotted-dashed* line), remained remarkably stable even when the cell height (Figure 6.2C, *solid line*) changed during the experiment. The fluorescence intensities at the top and bottom membrane were matched, which suggests that the affinity of binding to either membrane was the same. The concentration c_{Cyto} of cytoplasmic H-Ras-EGFP is determined from the cytosolic fluorescence intensity by $F_{Cyto,\infty} = c_{Cyto}\lambda V_\infty$, where V_∞ is the PSF volume and λ represents the brightness of the EGFP protein that was measured by an independent control experiment. The protein concentration σ_M at the membrane is determined from the intensity F_M at the membrane by a similar relation, $F_M = \sigma_M \lambda A_0$, where V_∞ is replaced by the PSF area A_0. Applying these relations to the data of Figure 6.2 yielded surface concentrations of σ_B = 900 μm^{-2} and σ_T = 920 μm^{-2} for the bottom and top membranes and a cytoplasmic concentration c_{Cyto} = 71 μm^{-3}.

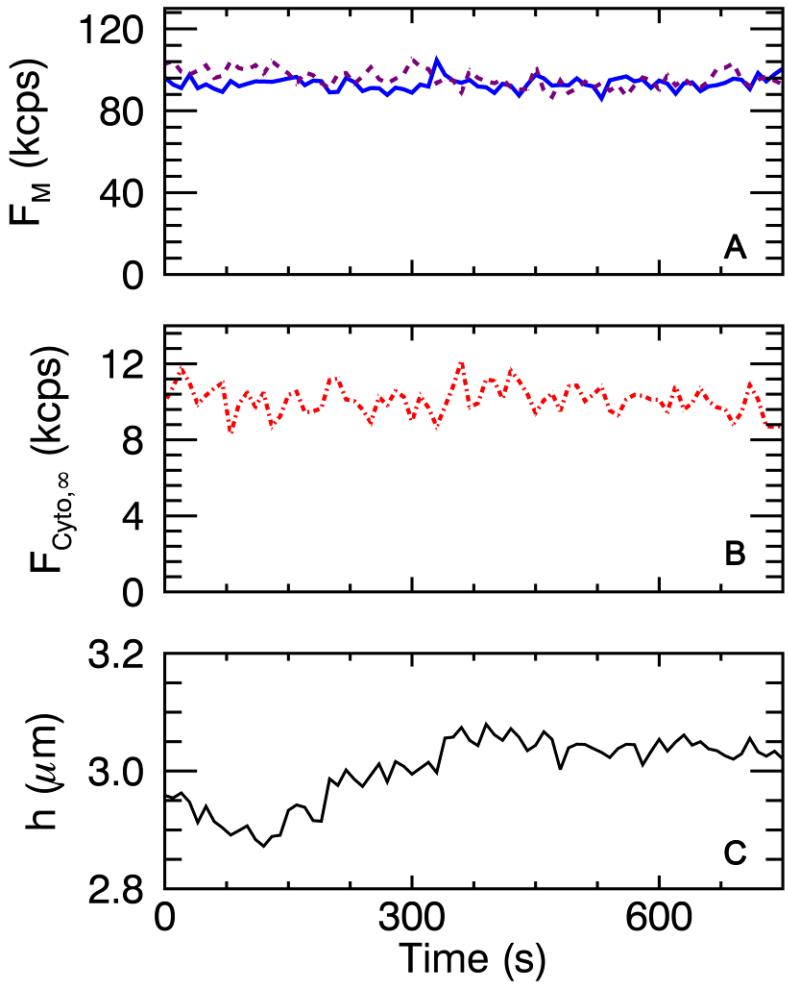

Figure 6.2 Repeated z-scans: EGFP-H-Ras.

Fit parameters of consecutive z-scan intensity profiles taken in an U2OS cell expressing EGFP-H-Ras. (*A*) Fluorescence intensities at the top (*dashed line*) and bottom (*solid line*) membrane remain stable (F_B =93.7 ± 3.2 kcps, F_T =95.6 ± 4.3 kcps,). (*B*) Cytoplasmic intensity (*dot-dashed line*) is constant ($F_{Cyto,\infty}$ =10.0 ± 0.8 kcps). (*C*) The cell thickness (*solid line*) changed within the first few minutes and then remained approximately constant.

6.3.2 Membrane binding curve

Cells transiently transfected with EGFP labeled Myo1C were selected and their z-scan intensity profile measured. The membrane and cytoplasmic intensity were determined by a fit of the intensity profile and are plotted in Figure 6.3A. The uncertainty in the fitted membrane and cytoplasmic intensities was on the order of or smaller than the symbol size and therefore was not plotted. The same condition applied to all membrane binding plots shown in this work. The membrane fluorescence intensity versus cytoplasmic fluorescence intensity displays a concentration dependent response, which saturates at high cytoplasmic intensities. Fluorescence intensities from the bottom membrane (*open triangles*) and the top membrane (*solid triangles*) are in close agreement. The data represent the binding curve $F_M\left(F_{Cyto,\infty}\right)$ of the peripheral membrane protein to the plasma membrane. To model the experimental data consider a cytoplasmic protein P that binds a free membrane binding site M with dissociation coefficient K to become a membrane-associated protein MP, $\mathrm{M} + \mathrm{P} \underset{\longleftarrow}{\overset{K}{\longrightarrow}} \mathrm{MP}$. The fractional saturation θ of the membrane binding sites is described by the Langmuir isotherm,

$$\theta = \frac{\sigma_M}{\sigma_0} = \frac{c_{Cyto}}{K + c_{Cyto}}, \tag{6.5}$$

where c_{Cyto} and σ_M are the cytoplasmic and membrane-bound protein concentrations, while σ_0 represents the concentration of the total number of membrane binding sites $\mathrm{M}_0 = \mathrm{M} + \mathrm{MP}$.

We relate the Langmuir-isotherm to fluorescence intensities to facilitate the analysis of the data in Figure 6.3A. The cytoplasmic and membrane-bound protein

concentrations are connected to the fluorescence intensities as described earlier, $F_{Cyto,\infty} = c_{Cyto}\lambda V_\infty$ and $F_M = \sigma_M \lambda A_0$. We further introduce the saturating fluorescence intensity at the membrane, $F_0 = \sigma_0 \lambda A_0$, and $F_K = K\lambda V_\infty$ to relate both the maximum binding site concentration and the dissociation coefficient to an intensity. Inserting these relations into Eq. 6.5 provides an alternate formulation of the Langmuir isotherm in terms of fluorescence intensities,

$$F_M = \theta F_0 = \frac{F_0 F_{Cyto,\infty}}{F_K + F_{Cyto,\infty}}. \tag{6.6}$$

A fit of the intensity data in Figure 6.3A to Eq. 6.6 with F_0 and F_K as free parameters is shown as solid line with $F_K = 24 \pm 5$ kcps and $F_0 = 83 \pm 10$ kcps. We use the EGFP brightness λ, the PSF volume V_∞ and the area A_0 to convert these values into the dissociation coefficient $K = 160 \pm 30\,\mu\text{m}^{-3} = 270 \pm 50\,\text{nM}$ and saturation concentration $\sigma_0 = 750 \pm 90\,\mu\text{m}^{-2}$.

An alternate way to represent membrane binding is to graph the membrane intensity fraction

$$f_M = \frac{F_M}{F_M + F_{Cyto,\infty}} \tag{6.7}$$

versus the cytoplasmic intensity $F_{Cyto,\infty}$. Because the z-scan intensity profile distinguishes between the bottom and top membrane, we further introduce the intensity fraction f_B of the bottom membrane and the intensity fraction f_T of the top membrane, which are defined by replacing F_M with F_B and F_T in Eq. 6.7, respectively. The membrane

intensity fraction of the Myo1C data as a function of cytoplasmic intensity is shown in Figure 6.3B. The dashed line represents the Langmuir isotherm model,

$$f_M = \frac{F_0}{F_K + F_{Cyto,\infty} + F_0}, \tag{6.8}$$

with values for F_0 and F_K as determined above. The membrane intensity fraction decays monotonically with cytoplasmic concentration, because an increase in protein concentration leads to a further depletion of the available membrane binding sites. Evaluating Eq. 6.8 for a cytoplasmic concentration $F_{Cyto,\infty} = 0$ determines the maximum limiting value $\overline{f}_M = \frac{F_0}{F_K + F_0}$ for the membrane intensity fraction, which for the Myo1C data is 0.78. Thus, the saturation concentration σ_0 and the dissociation coefficient *K* are not independent variables, but linked by $\overline{f}_M$. If the data of the fluorescence membrane binding curve $F_M\left(F_{Cyto,\infty}\right)$ are insufficient to identify σ_0 and *K* unambiguously, an extrapolation of the measured fractional membrane intensity f_M can be used to identify the ratio of both parameters, which for intensity-based notation is given by $F_K / F_0 = \left(1 - \overline{f}_M\right) \Big/ \overline{f}_M$.

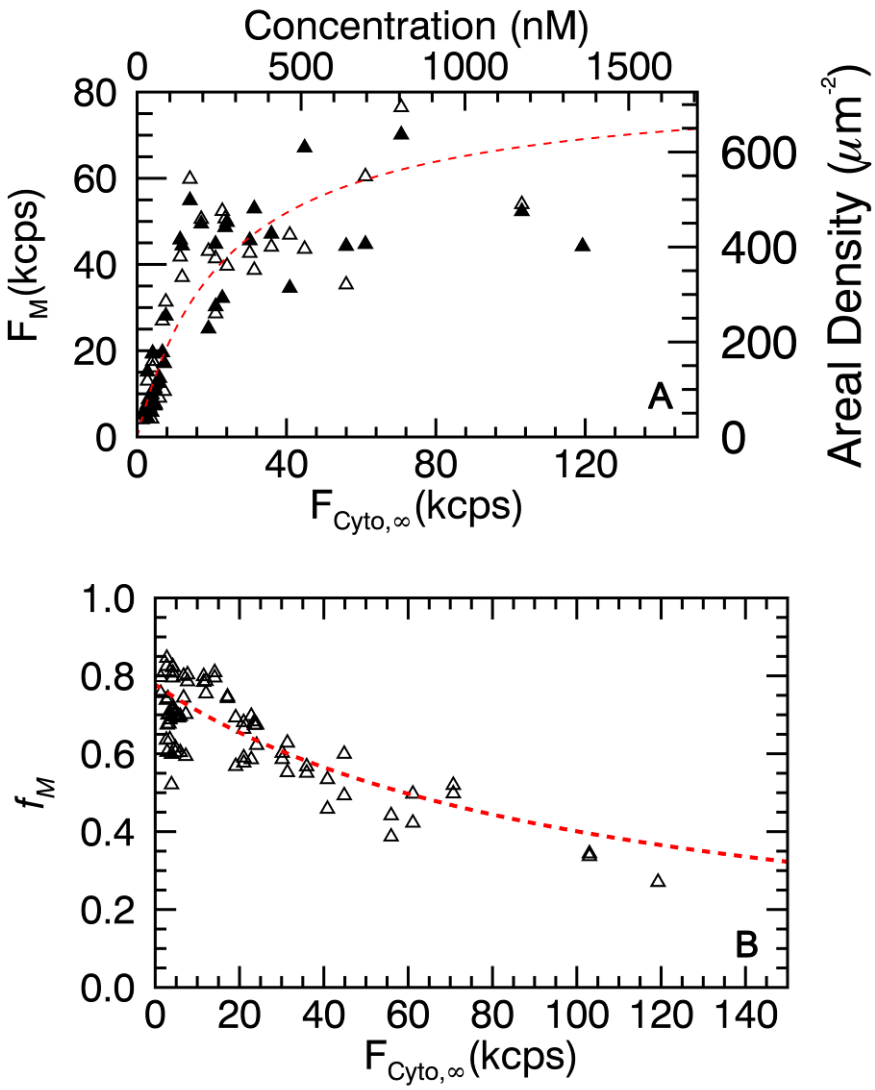

Figure 6.3 Fluorescence membrane binding curve of Myo1C-EGFP.

(*A*) Fluorescence intensity at the bottom (*open triangles*) and top (*solid triangles*) membrane versus fluorescence intensity in the cytoplasm. The fit (*dotted line*) to Eq. 6.6 recovers F_0 =83 kcps and F_K =24 kcps. The top and right axes specify the cytoplasmic and membrane-bound protein concentrations. (*B*) Membrane intensity fraction versus fluorescence intensity in the cytoplasm (*open triangles*) is well approximated by Eq. 6.8 (*dotted line*) with the same F_0 and F_K as determined in A.

6.3.3 Lipid binding protein domains

Lactadherin is a peripheral membrane protein shown to interact with phosphatidylserine (PS) lipids through its C2 domain (152, 153). We measured U2OS cells transiently transfected with an EGFP-labeled Lact-C2 fragment (Lact-C2-EGFP) and determined the experimental membrane-binding curve (see Figure 6.4, *open triangles*). A fit (*solid line*) to the Langmuir-isotherm binding model leads to a saturation concentration $\sigma_0 = 4100 \pm 1100\,\mu\text{m}^{-2}$ and a dissociation coefficient $K = 700 \pm 310$ nM. In a follow-up experiment we cotransfected Lact-C2-EGFP and Lact-C2-mCh using a plasmid ratio of 1:3. We selected cells that express both proteins and measured the membrane-binding curve (*open squares*) of Lact-C2-EGFP from the fluorescence intensity traces in the green detection channel. The membrane saturation intensity F_0 is much lower than in the previous experiment, reflecting the presence of Lact-C2-mCh that competes with the green-labeled protein. We divided the amplitude of the Lact-C2-EGFP Langmuir-isotherm curve (*solid line*) by four to account for the binding site competition provided by Lact-C2-mCh. The binding curve (*dashed line*) with the rescaled amplitude is in good agreement with the experimental data and illustrates the feasibility of binding competition assays.

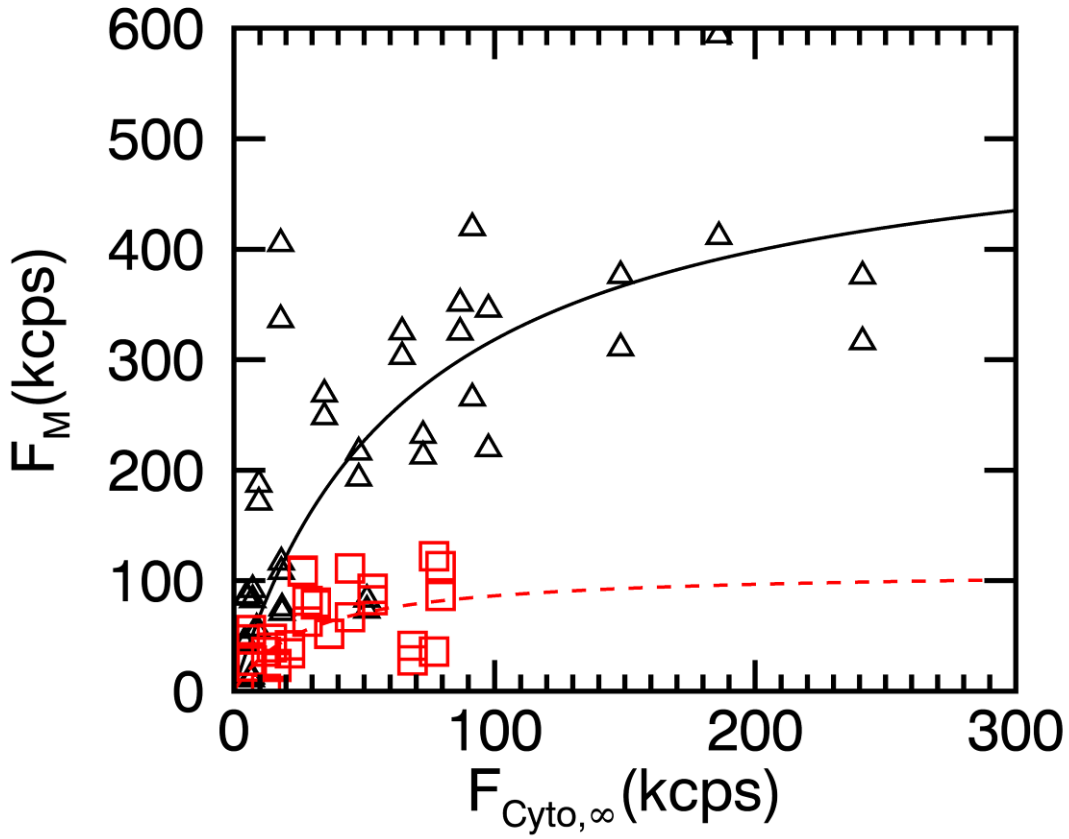

Figure 6.4 LactC2-EGFP fluorescence membrane binding curves.

Fluorescence membrane binding curve (*open triangles*) for LactC2-EGFP in U2OS cells with fit (*solid line*) to Eq. 6.6 (F_0 =530 kcps, F_K = 68 kcps). Competitive binding curve for LactC2-EGFP coexpressed with LactC2-mCh at a 1:3 ratio (*open squares*) agrees with predicted binding curve (*dashed line*).

We also examined the plasma-membrane binding curve of the PH domain of PLCδ, which is known to interact with $PI(4,5)P_2$ lipids (132). The experimental membrane-binding data (Figure 6.5A, *open circles*) of EGFP-labeled PH-PLCδ were determined in U2OS cells and fit to a Langmuir isotherm model (*solid line*) with $\sigma_0 = 6200 \pm 1300\ \mu m^{-2}$ and $K = 5.3 \pm 1.4\ \mu M$. Next, we coexpressed PH-PLCδ-EGFP with miniGAP-mCh. We selected cells that express both proteins and determined the membrane-binding curve (Figure 6.5A, *solid stars*) of the PH-PLCδ-EGFP from the intensity signal of green detection channel. The presence of miniGAP led to a drastic change in the binding curve for PH-PLCδ, which was also reflected by the fit of the binding data to a Langmuir isotherm model (*dashed line*). Plotting the same data with a reduced scale allowed the behavior at low intensities to be more clearly visualized (See Appendix B). The marked decrease in the amplitude of the binding curve implied that miniGAP and PH-PLCδ compete for the same binding sites at the membrane. This observation is consistent with the fact that both proteins are known to interact with $PI(4,5)P_2$ (154, 155).

For a control experiment, we coexpressed PH-PLCδ-EGFP and Lact-C2-mCh in U2OS cells. The data in Figure 6.5B revealed that the experimental membrane-binding data of PH-PLCδ-EGFP in the presence (*asterisks*) or absence (*open circles*) of Lact-C2 closely track one another. In vitro studies reported that PH-PLCδ interacts with $PI(4,5)P_2$, while Lact-C2 interacts with PS (152, 153). Thus, both proteins are expected to target different binding sites at the membrane, which is corroborated by our experimental binding data.

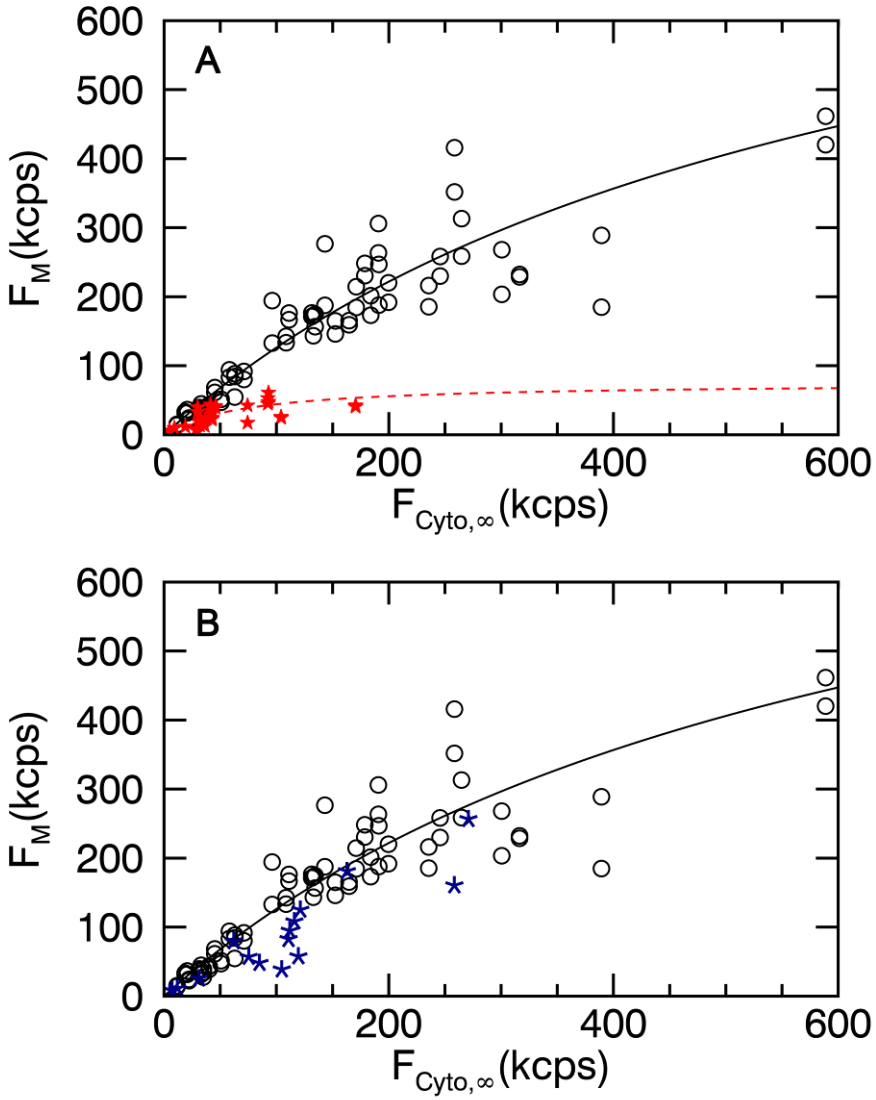

Figure 6.5 Membrane binding competition experiments of LactC2-EGFP.

(*A*) Binding curve for PH-PLCδ-EGFP (*open circles*) and fit (*solid line*) by Eq. 6.6 (F_0 =909 kcps, F_K = 620 kcps). Competitive binding curve for EGFP-PLCδ-PH coexpressed with MiniGAP-mCh (*solid stars*) and fit (*dotted line*) by Eq. 6.6 (F_0 =76kcps, F_K = 71 kcps). (*B*) Binding curve for PH-PLCδ-EGFP (*open circles*) and fit (*solid line*) as shown in A. Competitive binding curve for PH-PLCδ-EGFP coexpressed with LactC2-mCh (*asterisks*) closely tracks the binding curve for PH-PLCδ-EGFP alone.

6.3.4 HTLV-1 matrix

In chapter 4, we investigated the MA domain of Gag in an effort to uncover the initial assembly steps of the retrovirus HTLV-1 Gag. MA was chosen as a simplified test system for initial studies of the assembly process, because it is the primary driver of Gag association with the inner leaflet of the plasma membrane, but lacks the ability to associate into large multimers (114, 116). Previous work has shown that HTLV-1 MA Gag forms homo-complexes at the plasma membrane, but is monomeric in the cytoplasm (51, 107, 108, 156). Since the membrane binding mechanism of HTLV-1 MA is not well understood, we decided to investigate the lipid specificity, binding affinity, and saturation concentration of the process. We transiently transfected U2OS cells with EGFP-labeled MA and determined the cytoplasmic and membrane-bound fluorescence intensities from multiple cells. The data (Figure 6.6A, open triangles) show a concentration-dependent increase in the fluorescence signal at the membrane. A fit (*solid line*) of the data to a Langmuir-isotherm resulted in a dissociation coefficient of $K = 230 \pm 130$ nM and a membrane saturation concentration of $\sigma_0 = 2800 \pm 700$ μm^{-2}.

Further, we performed competition studies to probe the lipid specificity of HTLV-1 MA binding to the plasma membrane. We first coexpressed HTLV-1 MA-EGFP with miniGAP-mCh to probe binding to PI(4,5)P_2. In Figure 6.6B, the binding curve (*solid squares*) of HTLV-1 MA-EGFP in the presence of miniGAP-mCh overlaps with the binding data (*open triangles*) taken for HTLV-1 MA-EGFP alone. This observation suggests that PI(4,5)P_2 is not the main lipid target of HTLV-1 MA. We next coexpressed

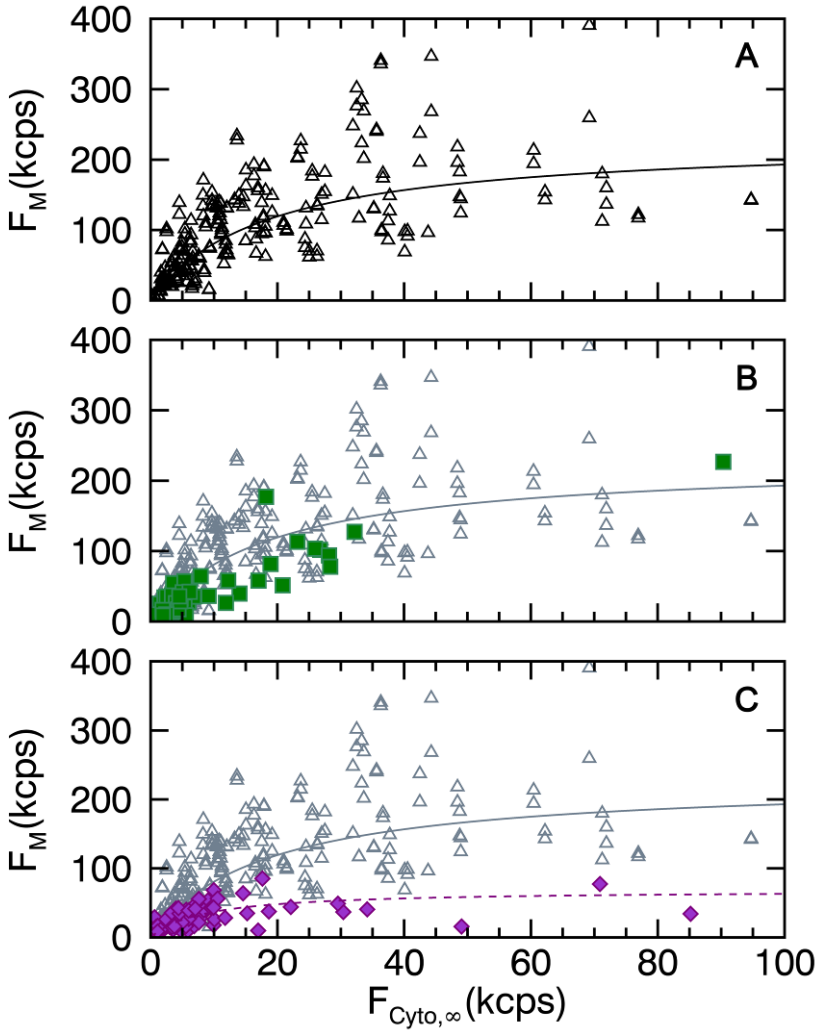

Figure 6.6 HTLV-1 MA-EGFP membrane binding curves.

(*A*) Fluorescence membrane binding curve (*triangles*) for HTLV-1 MA-EGFP expressed in U2OS cells. The same data are shown in B and C as gray symbols. The fit (*solid line*) to Eq. 6.6 leads to F_0 =18 kcps and F_K =288 kcps. (*B*) Competitive binding curve (*solid squares*) of MA-EGFP coexpressed with miniGAP-mCh. (*C*) Competitive binding curve (*solid diamonds*) of MA-EGFP coexpressed with LactC2-mCh and fit (*dashed line*) to Eq. 6.6 (F_0 =8 kcps, F_K = 68 kcps).

HTLV-1 MA-EGFP with Lact-C2-mCh to probe PS binding. The presence of Lact-C2-mCh led to a strong change in the binding curve of HTLV-1 MA-EGFP (see Figure 6.6C, *solid diamonds*) as compared to HTLV-1 MA-EGFP alone (*open triangles*). This result indicates that PS lipids are an important binding target of HTLV-1 MA. The dashed line represents the fit curve to a Langmuir-isotherm with a dissociation coefficient of $K = 130 \pm 16$ nM and a membrane saturation concentration of $\sigma_0 = 840 \pm 110$ μm^{-2}.

6.4 Discussion

Our data demonstrate that it is feasible to measure the membrane binding curve of fluorescently-labeled proteins inside living cells with z-scan FPD analysis. The technique relies on the deconvolution of the intensity profile with the help of an accurately parameterized PSF. We have found that the modified Gaussian-Lorentzian model provides a very faithful representation of the PSF for the two-photon instruments in our lab (51, 76). An additional consideration is the cell height at the scan position, which must be sufficiently large to distinguish membrane and cytoplasmic contributions by the deconvolution process. In our experience, the cell thickness should be at least twice the axial beam waist z_R of the PSF, which implies a minimum thickness of ~2 μm for our setup, a condition that was satisfied for all cell measurements presented in this study. Thus, while our study focused on U2OS cells, z-scan FPD has the potential to be expanded to other cell types as long as their minimum height is ~2 μm.

Analysis of z-dependent intensity distributions of fluorescently labeled cells is not a novel concept in itself. For example, z-stack image analysis has been widely used in the

fluorescence field to determine protein localization which includes work from Scarlatta and coworkers where they segment the z-dependent intensity distribution of $G\alpha_q$ and Phospholipase Cβ into membrane and cytoplasmic regions (27, 28). However, segmentation does not result in a quantitative separation of fluorescence signals from different compartments, because the PSF blurs the signal contributions. Modeling approaches have been used to account for the effect of the PSF, including recent work which used a 3D Gaussian PSF to identify the membrane-bound and free intensities of tBid in an *in vitro* environment (157). However, an accurate and quantitative analysis requires a parameterized PSF to avoid systemic biases. Z-scan FPD achieves this goal and partitions the intensity profile into its membrane and cytoplasmic components. While the current study was performed on a two-photon microscope, we expect that the same types of experiments are feasible on a one-photon confocal instrument. Extension of the z-scan method only requires a proper parameterization of the one-photon observation volume O (120), which replaces the PSF of two-photon excitation.

In this work we focused on the binding of a number of different protein domains to $PI(4,5)P_2$ and PS lipids. It has been estimated that the surface density of $PI(4,5)P_2$ lipid on the cell membrane is between 3000-5000 molecules/μm^2 (31) and that PH-PLCδ binds to $PI(4,5)P_2$ with a dissociation coefficient ranging from 2 to 3 μM in vitro (132, 158). Fitting the binding curve of PH-PLCδ-EGFP (see Figure 6.5B) determined a surface concentration of 6200±1300 molecules/μm^2 and a binding dissociation coefficient of K=5.3±1.4 μM in situ, which are close to the previously reported in vitro values. The binding curve of miniGAP-EGFP to the plasma membrane can be found in Appendix C.

We also applied our technique to study the binding of Lact-C2-EGFP to PS lipids. Estimates of the lipid composition at the plasma membrane indicate that PS is more abundant than $PI(4,5)P_2$ (31). Thus, we expected to measure a higher surface density than for PH-PLCδ-EGFP, but experimentally observed a surface density of 4100 molecules/μm^2 for Lact-C2-EGFP (see Figure 6.5A), which is less than what we measured for PH-PLCδ-EGFP. However, the z-scan binding assay does not measure the lipid concentration, but the protein concentration at the membrane. Thus, accessibility to the targeted lipid as well as competition for binding sites from other cellular protein will modulate the saturation concentration at the membrane. The binding affinity of LactC2 for PS on lipid vesicles has been measured by FRET experiments with reported in vitro dissociation coefficients of K=290 – 350 nM (159, 160) which agrees within a factor of two with our result.

Myo1C, a member of the myosin I superfamily, is known to associate with plasma membrane lipids ($PI(4,5)P_2$ and PS) through electrostatic interactions involving the tail domain (161, 162). Hokanson and Ostap studied the binding of the Myo1C tail fragment to LUVs containing 2% $PI(4,5)P_2$ and reported K_D values that depended on labeling and ranged from 230 to 530 nM (163, 164). We determined a K=270 nM for full length Myo1C-EGFP in U2OS cells, which is in close agreement with the in vitro results from the Myo1C fragments. Finding the same affinity for the fragment and the full-length protein suggests that the tail domain of Myo1C is the main determinant for the membrane binding energy. This property has also been found in other proteins. For example, PLCδ and its PH domain bind with a very similar affinity (147). Further results for Myo1C can

be found in the appendices. We characterized the protein's oligomeric state at the membrane and its lipid specificity in Appendices D and E.

We used the matrix domain of HTLV-1 Gag to probe the early assembly steps of this retrovirus. The MA domain of Gag contains a myristoyl moiety and a highly basic region, which are both important for membrane binding (reviewed (165)). For HIV-1 the MA domain and full length Gag only associate with the plasma membrane at high protein concentrations, where protein-protein interactions trigger the exposure of the sequestered myristoyl moiety (108, 165). In contrast, the MA domain and full length Gag of HTLV-1 have been found to associate with the plasma membrane even at the lowest measurable fluorescence intensities (108). While this observation seems to imply a very high binding affinity, the data in Figure 6.6 indicate a dissociation constant of several hundred nanomolar, which is a lower affinity than originally expected. This apparent inconsistency can be resolved by considering the limiting value $\bar{f}_M$ of the membrane fraction as the cytoplasmic protein concentration approaches zero, which depends on the surface concentration of binding sites and the affinity. The fit parameters of the binding curve for MA result in $\bar{f}_M = 0.92$, which reflects the large ratio of F_0 to F_K. In other words, a sufficient high number of binding sites compensates for a lower binding affinity and results in a significant population of membrane-bound proteins even at the lowest expression levels. In the case of MA over 90% of the protein is at the plasma membrane at very low cytoplasmic protein concentrations.

The membrane binding partner of HTLV-1 Gag is still an open question. It has been shown that HIV-1 Gag binding with $PI(4,5)P_2$ is essential for function (114).

However, when Inlora et al. recently studied the interaction between $PI(4,5)P_2$ and the MA domain of HTLV-1, they concluded that $PI(4,5)P_2$ was not essential for particle assembly (166). This finding is corroborated by our in situ competitive binding assay (see Figure 6.6B) which demonstrates that $PI(4,5)P_2$ is not an essential binding partner of MA. Instead we found that HTLV-1 MA-EGFP binds to PS lipid at the plasma membrane (Figure 6.6C). This observation agrees with in vitro work reporting that HTLV-1 Gag binds to liposomes containing PS (166).

The same study argued that HTLV-1 MA interacts with lipids primarily through electrostatic and not lipid-specific interactions. If electrostatic interactions are the main driver for membrane association, we would expect to observe competition for the $PI(4,5)P_2$ binding site, because the net charges of $PI(4,5)P_2$ at neutral pH is expected to be −3 or −4 (147), while for PS it is −1. However, the data in Figure 6.6B show no or at best only weak interaction between HTLV-1 MA and $PI(4,5)P_2$, since the competitive binding curve (*solid squares*) is only slightly lower than the binding curve for MA alone (*open triangles*). A potential explanation for the stronger interaction with PS lipids might be found in the distribution of basic residues in the matrix protein. Unlike HIV-1 MA, the basic residues of HTLV-1 MA are distributed throughout the sequence (167). The higher abundance of PS over $PI(4,5)P_2$ at the inner leaflet of the plasma membrane might lead to a larger number of local interactions with the distributed basic residues of the protein, which would result in an increased binding energy. Thus, our data suggest that interaction with PS lipids at the membrane plays an important role in the early assembly step of the HTLV-1 virus.

We briefly note that it is important to choose a suitable scan location within the cell. If the protein of interest is excluded from certain cellular compartments, then the presence of such a compartment along the scan trajectory will lead to a dip in the intensity profile, provided the compartment is comparable in size to the PSF. We use a brightfield image of the cell to find a position that avoids large structures such as the nucleus and the surrounding endomembrane system. We further perform at least two successive z-scans at each scan location, because movement of vesicles or other compartments between two successive scans introduces changes in the intensity profile. We only accept data where the intensity profile remains unchanged between scans. While these methods have proven sufficient for studying protein binding to the plasma membrane, a more sophisticated approach will be needed for proteins that interact with internal membranes to account for their complex spatial distribution inside the cell.

FPD analysis of the z-scan intensity profile separates membrane-bound and cytoplasmic protein components in terms of intensity. To translate these intensities into absolute concentrations requires an additional conversion factor from an independent experiment. In this work, we used the brightness of monomeric EGFP (determine from an independent control experiment) as our conversion factor to identify concentrations. However, even in the absence of a conversion factor, it is still possible to quantitatively compare intensity-based binding curves because the concentration and intensity are linearly related. This point is illustrated by the competition experiments depicted in Figures. 6.4, 6.5, and 6.6.

The heterogeneity of the cytoplasm introduces uncertainty in brightness experiments and therefore in the determination of protein concentration, an issue that has been studied early on (1). We have found that the uncertainty of brightness measurements in cells is ~10% (76), which implies a ~10% uncertainty in determining the concentration. Similarly, we also observed a brightness uncertainty of ~10% at the plasma membrane (51). Our current study generated membrane binding curves through single point z-scan measurements taken over a sample of cells. However, the scatter in the data points of the measured binding curves appears much larger than the measurement uncertainty. This spread of intensities at the membrane for a given cytoplasmic concentration might reflect cell to cell variations or be caused by spatial heterogeneity at the cell membrane. To address this issue we plan to expand the z-scan technique by combining it with x-y scans to explore small regions of the plasma membrane. This approach should allow us to investigate the origin of the scatter in the binding curve and potentially expand the reach of the technique to study binding of proteins with a non-uniform spatial distribution at the plasma membrane. While these developments will strengthen the technique, the results obtained from simple z-scans are already impressive. Single point z-scans have proven to be sufficient for quantitative analysis of the binding and competition experiments shown here.

In summary, z-scan FPD offers a new method for characterizing binding curves of peripheral membrane proteins within their native environment. The technique not only offers a way to test the binding results from ex situ studies within a cellular system, but also promises to reveal novel features. For example, competition assays can be performed

to identify specific lipid-protein binding partners. We anticipate that the ability to quantitatively monitor membrane binding in situ should prove useful for functional studies of membrane-binding proteins.

7. Summary

Quantitative analysis of protein-protein interactions at the plasma membrane is important for addressing fundamental biological and physical questions of cellular systems. In addition, information about protein-protein interactions is a prerequisite for developing a molecular-level picture of disease models. While FFS brightness analysis offers a way to determine the oligomeric state of a protein within a live cell environment, traditional FFS analysis breaks down when different compartments and their boundaries, such as the plasma membrane, are present in the observation volume.

In this thesis we addressed this challenge by developing z-scan FFS to simultaneous determine brightness at the membrane and in the cytoplasm. The technique requires only four inputs to connect the experimental raw brightness to the underlying physical brightness of each fluorescent layer of the sample: (1) a well characterize PSF, (2) a geometric model for the cell layers, (3) the z-scan fluorescence intensity profile, and (4) point FFS measurements taken at the top and bottom plasma membrane and in the cytoplasm. We demonstrated the feasibility of the technique by using H-Ras-EGFP as a model system and showed that in U2OS cells it exists as monomer both in cytoplasm and at the plasma membrane.

A byproduct of z-scan FFS is the z-scan intensity profile. We realized that deconvolution of the intensity profile into the cytoplasmic and membrane-associated components provides an excellent opportunity for quantitative membrane binding of proteins in a living cell. The deconvolution, which we refer to as z-scan FPD analysis, requires an accurate PSF model together with a geometric model of the cell layers. The

intensities recovered by FDP analysis can be translated into concentrations through use of an independently determined conversion factor, like the brightness of EGFP.

We experimentally validated z-FPD and characterized both the resolvability and stability of z-scan fitting and applied the technique in two distinct ways. First, we made time-resolved measurements of the reversible association of peripheral membrane proteins to the plasma membrane, quantified the translocation of the protein, and measured protein-specific cell height changes. Second, we generated membrane binding curves by performing FPD analysis over a population of cells. By fitting the membrane binding curves, we determined the number of binding sites and the dissociation coefficient of the protein. Finally, we combined the dual-color work from chapter 3 with z-scan FPD analysis to examine the protein-lipid interactions of selected protein domains and demonstrated that competition binding experiments can be used to identify specific lipid-protein interactions in living cells.

We applied z-scan FFS and z-scan FPD to provide insight into the early assembly steps of the HTLV-1 retrovirus. We focused on the matrix (MA) domain of HTLV-1 Gag because it is the primary driver of Gag association with the plasma membrane's inner leaflet. Figure 7.1 summarizes our results. HTLV-1 MA-EGFP binds to the plasma membrane with a lower affinity than we initially predicted based on earlier work, which demonstrated association of MA and full length Gag with the plasma membrane at very low intensities (108). We resolved this inconsistency by examining the limiting value of the membrane intensity fraction, which suggested that an abundant number of

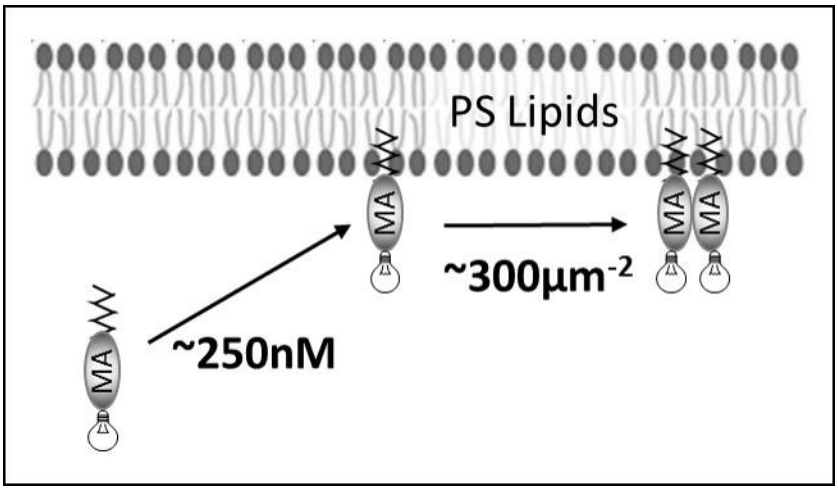

Figure 7.1 Summary of HTLV-1 MA-EGFP results.

HTLV-1 MA-EGFP binds to the plasma membrane as a monomer with an affinity of *K~250 nM* and undergoes a monomer to dimer transition at the membrane with a dissociation coefficient of ~300 μm^{-2}.

binding sites compensates for a lower binding affinity. The z-scan brightness data showed that HTLV-1 MA-EGFP is monomeric in the cytoplasm and undergoes a monomer to dimer transition at the plasma membrane. Competition studies further showed that PS lipids are an important target for the MA domain of HTLV-1 Gag. These results provide the foundation for future z-scan studies on the full-length Gag protein.

Z-scan FFS and z-scan FPD appear to be very promising techniques with many potential applications. At this point there are at least three future developments that would significantly broaden the range of applications: (1) apply the z-scan techniques to internal membranes, (2) perform dual-color z-scan studies to probe hetero-species interactions, and (3) combine z-scanning with x-y imaging. We already applied z-scan FFS to an internal membrane in collaboration with researchers in the department of Molecular, Cellular, Developmental Biology and Genetics. More specifically we completed preliminary feasibility studies (see Appendix F) and have taken z-scan brightness data on Torsin-1A (TA) within the perinuclear space (see Appendix G).

Dual-color z-scans were only used in a rudimentary way within this thesis and dual-color brightness measurements were never performed. In future work, dual-color z-scan FFS in combination with TIFCA analysis could have an important role in quantifying protein interactions at the plasma membrane where many intracellular signaling and trafficking processes are accompanied by hetero-species interactions. While the z-scan theory put forth within the thesis will be the platform of the technique, the cotransfection modeling work within chapter 3 will also be important. The cotransfection model allows us to predict the average and distribution of the protein expression ratios for

different pDNA mixing ratios, which will be useful for choosing expression ratios that maximize the presence of hetero-protein complexes.

Finally, the combination of x-y scanning with z-scanning will allow us to probe spatial heterogeneities at the plasma membrane, while retaining the geometric and intensity information from the z-scan analysis. While the single point measurement per cell was sufficient for quantitative analysis of the binding curve (chapter 6), we observed significant scatter in the measured data points. This result might reflect the presence of significant spatial heterogeneity of membrane binding at the plasma membrane. A combined x-y and z-scan technique should be able to address this open question.

In conclusion, this work describes a pair of z-scan fluorescence techniques that characterize proteins at the cytoplasm / plasma membrane interface of living cells. Our experimental results are testimony to the unique strength of our approach. The techniques described in this thesis add new powerful tools to our arsenal for studying and quantifying the behavior of proteins that interact with the plasma membrane.

References

1. Chen, Y., J.D. Müller, Q. Ruan, and E. Gratton. 2002. Molecular brightness characterization of EGFP in vivo by fluorescence fluctuation spectroscopy. Biophys. J. 82: 133–144.

2. Chen, Y., L.-N. Wei, and J.D. Mueller. 2003. Probing protein oligomerization in living cells with fluorescence fluctuation spectroscopy. Proc. Natl. Acad. Sci. U. S. A. 100: 15492–15497.

3. Chen, Y., L.-N. Wei, and J.D. Mueller. 2005. Unraveling Protein-Protein Interactions in Living Cells with Fluorescence Fluctuation Brightness Analysis. Biophys. J. 88: 4366–4377.

4. Ruan, Q., Y. Chen, E. Gratton, M. Glaser, and W.W. Mantulin. 2002. Cellular characterization of adenylate kinase and its isoform: two-photon excitation fluorescence imaging and fluorescence correlation spectroscopy. Biophys. J. 83: 3177–3187.

5. Saffarian, S., Y. Li, E.L. Elson, and L.J. Pike. 2007. Oligomerization of the EGF receptor investigated by live cell fluorescence intensity distribution analysis. Biophys. J. 93: 1021–1031.

6. Malengo, G., A. Andolfo, N. Sidenius, E. Gratton, M. Zamai, and V.R. Caiolfa. 2008. Fluorescence correlation spectroscopy and photon counting histogram on membrane proteins: functional dynamics of the glycosylphosphatidylinositol-anchored urokinase plasminogen activator receptor. J. Biomed. Opt. 13: 031215.

7. Godin, A.G., S. Costantino, L.-E. Lorenzo, J.L. Swift, M. Sergeev, A. Ribeiro-da-Silva, Y. De Koninck, and P.W. Wiseman. 2011. Revealing protein oligomerization and densities in situ using spatial intensity distribution analysis. Proc. Natl. Acad. Sci. U. S. A. 108: 7010–7015.

8. Cho, W., and R.V. Stahelin. 2005. Membrane-protein interactions in cell signaling and membrane trafficking. Annu. Rev. Biophys. Biomol. Struct. 34: 119–151.

9. Glomset, J.A. 1999. Protein-lipid interactions on the surfaces of cell membranes. Curr. Opin. Struct. Biol. 9: 425–427.

10. Goñi, F.M. 2002. Non-permanent proteins in membranes: when proteins come as visitors (Review). Mol. Membr. Biol. 19: 237–245.

11. Eisenberg, S., A.J. Laude, A.J. Beckett, C.J. Mageean, V. Aran, M. Hernandez-Valladares, Y.I. Henis, and I.A. Prior. 2013. The role of palmitoylation in regulating Ras localization and function. Biochem. Soc. Trans. 41: 79–83.

12. Eisenberg, S., and Y.I. Henis. 2008. Interactions of Ras proteins with the plasma membrane and their roles in signaling. Cell. Signal. 20: 31–39.

13. Vögler, O., J.M. Barceló, C. Ribas, and P.V. Escribá. 2008. Membrane interactions of G proteins and other related proteins. Biochim. Biophys. Acta. 1778: 1640–1652.

14. Escribá, P.V., P.B. Wedegaertner, F.M. Goñi, and O. Vögler. 2007. Lipid-protein interactions in GPCR-associated signaling. Biochim. Biophys. Acta. 1768: 836–852.

15. Insel, P.A., C.-M. Tang, I. Hahntow, and M.C. Michel. 2007. Impact of GPCRs in clinical medicine: genetic variants and drug targets. Biochim. Biophys. Acta. 1768: 994–1005.

16. Marinissen, M.J., and J.S. Gutkind. 2001. G-protein-coupled receptors and signaling networks: emerging paradigms. Trends Pharmacol. Sci. 22: 368–376.

17. Giguere, P.M., W.K. Kroeze, and B.L. Roth. 2014. Tuning up the right signal: chemical and genetic approaches to study GPCR functions. Curr. Opin. Cell Biol. 27: 51–55.

18. Urs, N.M., P.J. Nicholls, and M.G. Caron. 2014. Integrated approaches to understanding antipsychotic drug action at GPCRs. Curr. Opin. Cell Biol. 27: 56–62.

19. Unal, H., and S.S. Karnik. 2012. Domain coupling in GPCRs: the engine for induced conformational changes. Trends Pharmacol. Sci. 33: 79–88.

20. Dorsam, R.T., and J.S. Gutkind. 2007. G-protein-coupled receptors and cancer. Nat. Rev. Cancer. 7: 79–94.

21. Cho, W., L. Bittova, and R.V. Stahelin. 2001. Membrane binding assays for peripheral proteins. Anal. Biochem. 296: 153–161.

22. Zhao, H., and P. Lappalainen. 2012. A simple guide to biochemical approaches for analyzing protein-lipid interactions. Mol. Biol. Cell. 23: 2823–2830.

23. Chan, Y.-H.M., and S.G. Boxer. 2007. Model membrane systems and their applications. Curr. Opin. Chem. Biol. 11: 581–587.

24. Carpenter, E.P., K. Beis, A.D. Cameron, and S. Iwata. 2008. Overcoming the challenges of membrane protein crystallography. Curr. Opin. Struct. Biol. 18: 581–586.

25. Devaux, P.F., and M. Seigneuret. 1985. Specificity of lipid-protein interactions as determined by spectroscopic techniques. Biochim. Biophys. Acta. 822: 63–125.

26. Selvin, P.R. 1995. Fluorescence resonance energy transfer. Methods Enzymol. 246: 300–334.

27. Aisiku, O., L. Dowal, and S. Scarlata. 2011. Protein kinase C phosphorylation of PLCβ1 regulates its cellular localization. Arch. Biochem. Biophys. 509: 186–190.

28. Dowal, L., P. Provitera, and S. Scarlata. 2006. Stable association between G alpha(q) and phospholipase C beta 1 in living cells. J. Biol. Chem. 281: 23999–24014.

29. Várnai, P., and T. Balla. 1998. Visualization of phosphoinositides that bind pleckstrin homology domains: calcium- and agonist-induced dynamic changes and relationship to myo-[3H]inositol-labeled phosphoinositide pools. J. Cell Biol. 143: 501–510.

30. Stauffer, T.P., S. Ahn, and T. Meyer. 1998. Receptor-induced transient reduction in plasma membrane PtdIns(4,5)P2 concentration monitored in living cells. Curr. Biol. CB. 8: 343–346.

31. Xu, C., J. Watras, and L.M. Loew. 2003. Kinetic analysis of receptor-activated phosphoinositide turnover. J. Cell Biol. 161: 779–791.

32. Axelrod, D. 1989. Total internal reflection fluorescence microscopy. Methods Cell Biol. 30: 245–270.

33. Axelrod, D. 2001. Total internal reflection fluorescence microscopy in cell biology. Traffic Cph. Den. 2: 764–774.

34. Mattheyses, A.L., S.M. Simon, and J.Z. Rappoport. 2010. Imaging with total internal reflection fluorescence microscopy for the cell biologist. J. Cell Sci. 123: 3621–3628.

35. Digman, M.A., R. Dalal, A.F. Horwitz, and E. Gratton. 2008. Mapping the number of molecules and brightness in the laser scanning microscope. Biophys. J. 94: 2320–2332.

36. Digman, M.A., P.W. Wiseman, C. Choi, A.R. Horwitz, and E. Gratton. 2009. Stoichiometry of molecular complexes at adhesions in living cells. Proc. Natl. Acad. Sci. U. S. A. 106: 2170–2175.

37. Ross, J.A., M.A. Digman, L. Wang, E. Gratton, J.P. Albanesi, and D.M. Jameson. 2011. Oligomerization state of dynamin 2 in cell membranes using TIRF and number and brightness analysis. Biophys. J. 100: L15–17.

38. James, N.G., M.A. Digman, E. Gratton, B. Barylko, X. Ding, J.P. Albanesi, M.S. Goldberg, and D.M. Jameson. 2012. Number and brightness analysis of LRRK2 oligomerization in live cells. Biophys. J. 102: L41–43.

39. Schwille, P., J. Korlach, and W.W. Webb. 1999. Fluorescence correlation spectroscopy with single-molecule sensitivity on cell and model membranes. Cytometry. 36: 176–182.

40. Korlach, J., P. Schwille, W.W. Webb, and G.W. Feigenson. 1999. Characterization of lipid bilayer phases by confocal microscopy and fluorescence correlation spectroscopy. Proc. Natl. Acad. Sci. U. S. A. 96: 8461–8466.

41. García-Sáez, A.J., and P. Schwille. 2008. Fluorescence correlation spectroscopy for the study of membrane dynamics and protein/lipid interactions. Methods San Diego Calif. 46: 116–122.

42. Kahya, N., D. Scherfeld, K. Bacia, B. Poolman, and P. Schwille. 2003. Probing lipid mobility of raft-exhibiting model membranes by fluorescence correlation spectroscopy. J. Biol. Chem. 278: 28109–28115.

43. Ruan, Q., M.A. Cheng, M. Levi, E. Gratton, and W.W. Mantulin. 2004. Spatial-temporal studies of membrane dynamics: scanning fluorescence correlation spectroscopy (SFCS). Biophys. J. 87: 1260–1267.

44. Ries, J., S. Chiantia, and P. Schwille. 2009. Accurate determination of membrane dynamics with line-scan FCS. Biophys. J. 96: 1999–2008.

45. Ries, J., S.R. Yu, M. Burkhardt, M. Brand, and P. Schwille. 2009. Modular scanning FCS quantifies receptor-ligand interactions in living multicellular organisms. Nat. Methods. 6: 643–645.

46. Benda, A., M. Beneš, V. Mareček, A. Lhotský, W.T. Hermens, and M. Hof. 2003. How To Determine Diffusion Coefficients in Planar Phospholipid Systems by Confocal Fluorescence Correlation Spectroscopy. Langmuir. 19: 4120–4126.

47. Humpolickova, J., E. Gielen, A. Benda, V. Fagulova, J. Vercammen, M. vandeVen, M. Hof, M. Ameloot, and Y. Engelborghs. 2006. Probing Diffusion Laws within Cellular Membranes by Z-Scan Fluorescence Correlation Spectroscopy. Biophys. J. 91: L23–L25.

48. Stahelin, R.V. 2013. Surface plasmon resonance: a useful technique for cell biologists to characterize biomolecular interactions. Mol. Biol. Cell. 24: 883–886.

49. Wang, W., Y. Yang, S. Wang, V.J. Nagaraj, Q. Liu, J. Wu, and N. Tao. 2012. Label-free measuring and mapping of binding kinetics of membrane proteins in single living cells. Nat. Chem. 4: 846–853.

50. Smith, E.M., and J.D. Mueller. 2012. The statistics of protein expression ratios for cellular fluorescence studies. Eur. Biophys. J. EBJ. 41: 341–352.

51. Smith, E.M., P.J. Macdonald, Y. Chen, and J.D. Mueller. 2014. Quantifying protein-protein interactions of peripheral membrane proteins by fluorescence brightness analysis. Biophys. J. 107: 66–75.

52. Smith, E.M., J. Hennen, Y. Chen, and J.D. Mueller. 2015. Z-scan fluorescence profile deconvolution of cytosolic and membrane-associated protein populations. Anal. Biochem. 480: 11–20.

53. Chen, Y., J.D. Müller, K.M. Berland, and E. Gratton. 1999. Fluorescence fluctuation spectroscopy. Methods San Diego Calif. 19: 234–252.

54. Van Orden, A., K. Fogarty, and J. Jung. 2004. Fluorescence fluctuation spectroscopy: a coming of age story. Appl. Spectrosc. 58: 122A–137A.

55. Jameson, D.M., J.A. Ross, and J.P. Albanesi. 2009. Fluorescence fluctuation spectroscopy: ushering in a new age of enlightenment for cellular dynamics. Biophys. Rev. 1: 105–118.

56. Elson, E.L., and D. Magde. 1974. Fluorescence correlation spectroscopy. I. Conceptual basis and theory. Biopolymers. 13: 1–27.

57. Magde, D., E.L. Elson, and W.W. Webb. 1974. Fluorescence correlation spectroscopy. II. An experimental realization. Biopolymers. 13: 29–61.

58. Elson, E.L. 2011. Fluorescence correlation spectroscopy: past, present, future. Biophys. J. 101: 2855–2870.

59. Macháň, R., and T. Wohland. 2014. Recent applications of fluorescence correlation spectroscopy in live systems. FEBS Lett. 588: 3571–3584.

60. Chen, Y., J.D. Mueller, P.T. So, and E. Gratton. 1999. The photon counting histogram in fluorescence fluctuation spectroscopy. Biophys. J. 77: 553–567.

61. Qian, H., and E.L. Elson. 1990. On the analysis of high order moments of fluorescence fluctuations. Biophys. J. 57: 375–380.

62. Mueller, J.D. 2004. Cumulant analysis in fluorescence fluctuation spectroscopy. Biophys. J. 86: 3981–3992.

63. Wu, B., and J.D. Mueller. 2005. Time-integrated fluorescence cumulant analysis in fluorescence fluctuation spectroscopy. Biophys. J. 89: 2721–2735.

64. Denk, W., J.H. Strickler, and W.W. Webb. 1990. Two-photon laser scanning fluorescence microscopy. Science. 248: 73–76.

65. Berland, K.M., P.T. So, and E. Gratton. 1995. Two-photon fluorescence correlation spectroscopy: method and application to the intracellular environment. Biophys. J. 68: 694–701.

66. Macdonald, P., J. Johnson, E. Smith, Y. Chen, and J.D. Mueller. 2013. Brightness analysis. Methods Enzymol. 518: 71–98.

67. Thompson, N. 1991. Fluorescence correlation spectroscopy. In: Lakowicz J, editor. Topics in fluorescense spectroscopy. New York: Plenum Press. pp. 337–378.

68. Qian, H., and E.L. Elson. 1990. Distribution of molecular aggregation by analysis of fluctuation moments. Proc. Natl. Acad. Sci. U. S. A. 87: 5479–5483.

69. Qian, H. 1990. On the statistics of fluorescence correlation spectroscopy. Biophys. Chem. 38: 49–57.

70. Sanchez-Andres, A., Y. Chen, and J.D. Müller. 2005. Molecular brightness determined from a generalized form of Mandel's Q-parameter. Biophys. J. 89: 3531–3547.

71. Mandel, L. 1979. Sub-Poissonian photon statistics in resonance fluorescence. Opt. Lett. 4: 205–207.

72. Chen, Y., B. Wu, K. Musier-Forsyth, L.M. Mansky, and J.D. Mueller. 2009. Fluorescence Fluctuation Spectroscopy on Viral-Like Particles Reveals Variable Gag Stoichiometry. Biophys. J. 96: 1961–1969.

73. Johnson, J., Y. Chen, and J.D. Mueller. 2010. Characterization of brightness and stoichiometry of bright particles by flow-fluorescence fluctuation spectroscopy. Biophys. J. 99: 3084–3092.

74. Grigsby, I.F., W. Zhang, J.L. Johnson, K.H. Fogarty, Y. Chen, J.M. Rawson, A.J. Crosby, J.D. Mueller, and L.M. Mansky. 2010. Biophysical analysis of HTLV-1 particles reveals novel insights into particle morphology and Gag stochiometry. Retrovirology. 7: 75.

75. Chen, Y., J. Johnson, P. Macdonald, B. Wu, and J.D. Mueller. 2010. Observing protein interactions and their stoichiometry in living cells by brightness analysis of fluorescence fluctuation experiments. Methods Enzymol. 472: 345–363.

76. Macdonald, P.J., Y. Chen, X. Wang, Y. Chen, and J.D. Mueller. 2010. Brightness analysis by z-scan fluorescence fluctuation spectroscopy for the study of protein interactions within living cells. Biophys. J. 99: 979–988.

77. Day, R.N., and M.W. Davidson. 2009. The fluorescent protein palette: tools for cellular imaging. Chem. Soc. Rev. 38: 2887–2921.

78. Snapp, E.L. 2009. Fluorescent proteins: a cell biologist's user guide. Trends Cell Biol. 19: 649–655.

79. Day, R.N., and F. Schaufele. 2008. Fluorescent protein tools for studying protein dynamics in living cells: a review. J. Biomed. Opt. 13: 031202.

80. Ciruela, F. 2008. Fluorescence-based methods in the study of protein-protein interactions in living cells. Curr. Opin. Biotechnol. 19: 338–343.

81. Berland, K.M. 2004. Fluorescence correlation spectroscopy: a new tool for quantification of molecular interactions. Methods Mol. Biol. Clifton NJ. 261: 383–398.

82. Gambin, Y., and A.A. Deniz. 2010. Multicolor single-molecule FRET to explore protein folding and binding. Mol. Biosyst. 6: 1540–1547.

83. Haustein, E., and P. Schwille. 2007. Fluorescence correlation spectroscopy: novel variations of an established technique. Annu. Rev. Biophys. Biomol. Struct. 36: 151–169.

84. Felgner, P.L., T.R. Gadek, M. Holm, R. Roman, H.W. Chan, M. Wenz, J.P. Northrop, G.M. Ringold, and M. Danielsen. 1987. Lipofection: a highly efficient, lipid-mediated DNA-transfection procedure. Proc. Natl. Acad. Sci. U. S. A. 84: 7413–7417.

85. Ma, Z.-L., M. Werner, C. Körber, I. Joshi, M. Hamad, P. Wahle, and M. Hollmann. 2007. Quantitative analysis of cotransfection efficiencies in studies of ionotropic glutamate receptor complexes. J. Neurosci. Res. 85: 99–115.

86. Voges, D., M. Watzele, C. Nemetz, S. Wizemann, and B. Buchberger. 2004. Analyzing and enhancing mRNA translational efficiency in an Escherichia coli in vitro expression system. Biochem. Biophys. Res. Commun. 318: 601–614.

87. Hama, S., H. Akita, S. Iida, H. Mizuguchi, and H. Harashima. 2007. Quantitative and mechanism-based investigation of post-nuclear delivery events between adenovirus and lipoplex. Nucleic Acids Res. 35: 1533 –1543.

88. Hama, S., H. Akita, R. Ito, H. Mizuguchi, T. Hayakawa, and H. Harashima. 2006. Quantitative comparison of intracellular trafficking and nuclear transcription between adenoviral and lipoplex systems. Mol. Ther. 13: 786–794.

89. Hillesheim, L.N., Y. Chen, and J.D. Mueller. 2006. Dual-color photon counting histogram analysis of mRFP1 and EGFP in living cells. Biophys. J. 91: 4273–4284.

90. Ross, J.A., Y. Chen, J. Muller, B. Barylko, L. Wang, H.B. Banks, J.P. Albanesi, and D.M. Jameson. 2011. Dimeric Endophilin A2 Stimulates Assembly and GTPase Activity of Dynamin 2. Biophys. J. 100: 729–737.

91. Chen, Y., and J.D. Mueller. 2007. Determining the stoichiometry of protein heterocomplexes in living cells with fluorescence fluctuation spectroscopy. Proc. Natl. Acad. Sci. 104: 3147 –3152.

92. Zhou, X., and L. Huang. 1994. DNA transfection mediated by cationic liposomes containing lipopolylysine: characterization and mechanism of action. Biochim. Biophys. Acta BBA-Biomembr. 1189: 195–203.

93. Friend, D.S., D. Papahadjopoulos, and R.J. Debs. 1996. Endocytosis and intracellular processing accompanying transfection mediated by cationic liposomes. Biochim. Biophys. Acta BBA-Biomembr. 1278: 41–50.

94. El Ouahabi, A., M. Thiry, V. Pector, R. Fuks, J.M. Ruysschaert, and M. Vandenbranden. 1997. The role of endosome destabilizing activity in the gene transfer process mediated by cationic lipids. FEBS Lett. 414: 187–192.

95. Zuhorn, I.S., R. Kalicharan, and D. Hoekstra. 2002. Lipoplex-mediated transfection of mammalian cells occurs through the cholesterol-dependent clathrin-mediated pathway of endocytosis. J. Biol. Chem. 277: 18021–10828.

96. Xu, Y., and F.C. Szoka Jr. 1996. Mechanism of DNA release from cationic liposome/DNA complexes used in cell transfection. Biochemistry (Mosc.). 35: 5616–5623.

97. Ouahabi, A.E., M. Thiry, S. Schiffmann, R. Fuks, H. Nguyen-Tran, J.-M. Ruysschaert, and M. Vandenbranden. 1999. Intracellular Visualization of BrdU-labeled Plasmid DNA/Cationic Liposome Complexes. J. Histochem. Cytochem. 47: 1159 –1166.

98. Merkle, D., S.P. Lees-Miller, and D.T. Cramb. 2004. Structure and dynamics of lipoplex formation examined using two-photon fluorescence cross-correlation spectroscopy. Biochemistry (Mosc.). 43: 7263–7272.

99. Caracciolo, G., R. Caminiti, M.A. Digman, E. Gratton, and S. Sanchez. 2009. Efficient escape from endosomes determines the superior efficiency of multicomponent lipoplexes. J. Phys. Chem. B. 113: 4995–4997.

100. Kreiss, P., B. Cameron, R. Rangara, P. Mailhe, O. Aguerre-Charriol, M. Airiau, D. Scherman, J. Crouzet, and B. Pitard. 1999. Plasmid DNA size does not affect the physicochemical properties of lipoplexes but modulates gene transfer efficiency. Nucleic Acids Res. 27: 3792–3798.

101. Bengali, Z., J.C. Rea, R.F. Gibly, and L.D. Shea. 2009. Efficacy of Immobilized Polyplexes and Lipoplexes for Substrate-Mediated Gene Delivery. Biotechnol. Bioeng. 102: 1679–1691.

102. Johnson, J.E., and R.B. Cornell. 1999. Amphitropic proteins: regulation by reversible membrane interactions (review). Mol. Membr. Biol. 16: 217–235.

103. Smotrys, J.E., and M.E. Linder. 2004. Palmitoylation of intracellular signaling proteins: regulation and function. Annu. Rev. Biochem. 73: 559–587.

104. Rigler, R., Ü. Mets, J. Widengren, and P. Kask. 1993. Fluorescence correlation spectroscopy with high count rate and low background: analysis of translational diffusion. Eur. Biophys. J. 22: 169–175.

105. Schwille, P., U. Haupts, S. Maiti, and W.W. Webb. 1999. Molecular dynamics in living cells observed by fluorescence correlation spectroscopy with one- and two-photon excitation. Biophys. J. 77: 2251–2265.

106. Wills, J.W., and R.C. Craven. 1991. Form, function, and use of retroviral gag proteins. AIDS Lond. Engl. 5: 639–654.

107. Fogarty, K.H., Y. Chen, I.F. Grigsby, P.J. Macdonald, E.M. Smith, J.L. Johnson, J.M. Rawson, L.M. Mansky, and J.D. Mueller. 2011. Characterization of cytoplasmic Gag-gag interactions by dual-color z-scan fluorescence fluctuation spectroscopy. Biophys. J. 100: 1587–1595.

108. Fogarty, K.H., S. Berk, I.F. Grigsby, Y. Chen, L.M. Mansky, and J.D. Mueller. 2014. Interrelationship between cytoplasmic retroviral Gag concentration and Gag-membrane association. J. Mol. Biol. 426: 1611–1624.

109. Lindwasser, O.W., and M.D. Resh. 2001. Multimerization of human immunodeficiency virus type 1 Gag promotes its localization to barges, raft-like membrane microdomains. J. Virol. 75: 7913–7924.

110. Sandefur, S., V. Varthakavi, and P. Spearman. 1998. The I domain is required for efficient plasma membrane binding of human immunodeficiency virus type 1 Pr55Gag. J. Virol. 72: 2723–2732.

111. Perez-Caballero, D., T. Hatziioannou, J. Martin-Serrano, and P.D. Bieniasz. 2004. Human immunodeficiency virus type 1 matrix inhibits and confers cooperativity on gag precursor-membrane interactions. J. Virol. 78: 9560–9563.

112. Hamard-Peron, E., and D. Muriaux. 2011. Retroviral matrix and lipids, the intimate interaction. Retrovirology. 8: 15.

113. Ono, A., D. Demirov, and E.O. Freed. 2000. Relationship between human immunodeficiency virus type 1 Gag multimerization and membrane binding. J. Virol. 74: 5142–5150.

114. Ono, A., S.D. Ablan, S.J. Lockett, K. Nagashima, and E.O. Freed. 2004. Phosphatidylinositol (4,5) bisphosphate regulates HIV-1 Gag targeting to the plasma membrane. Proc. Natl. Acad. Sci. U. S. A. 101: 14889–14894.

115. Saad, J.S., J. Miller, J. Tai, A. Kim, R.H. Ghanam, and M.F. Summers. 2006. Structural basis for targeting HIV-1 Gag proteins to the plasma membrane for virus assembly. Proc. Natl. Acad. Sci. U. S. A. 103: 11364–11369.

116. Bryant, M., and L. Ratner. 1990. Myristoylation-dependent replication and assembly of human immunodeficiency virus 1. Proc. Natl. Acad. Sci. U. S. A. 87: 523–527.

117. Chen, Y., J.D. Müller, S.Y. Tetin, J.D. Tyner, and E. Gratton. 2000. Probing ligand protein binding equilibria with fluorescence fluctuation spectroscopy. Biophys. J. 79: 1074–1084.

118. Burniston, M.T., A. Cimarelli, J. Colgan, S.P. Curtis, and J. Luban. 1999. Human immunodeficiency virus type 1 Gag polyprotein multimerization requires the nucleocapsid domain and RNA and is promoted by the capsid-dimer interface and the basic region of matrix protein. J. Virol. 73: 8527–8540.

119. Dalton, A.K., D. Ako-Adjei, P.S. Murray, D. Murray, and V.M. Vogt. 2007. Electrostatic interactions drive membrane association of the human immunodeficiency virus type 1 Gag MA domain. J. Virol. 81: 6434–6445.

120. Hess, S.T., and W.W. Webb. 2002. Focal volume optics and experimental artifacts in confocal fluorescence correlation spectroscopy. Biophys. J. 83: 2300–2317.

121. Vetri, V., G. Ossato, V. Militello, M.A. Digman, M. Leone, and E. Gratton. 2011. Fluctuation methods to study protein aggregation in live cells: concanavalin A oligomers formation. Biophys. J. 100: 774–783.

122. Plowman, S.J., C. Muncke, R.G. Parton, and J.F. Hancock. 2005. H-ras, K-ras, and inner plasma membrane raft proteins operate in nanoclusters with differential dependence on the actin cytoskeleton. Proc. Natl. Acad. Sci. U. S. A. 102: 15500–15505.

123. Mazurov, D., G. Heidecker, and D. Derse. 2006. HTLV-1 Gag protein associates with CD82 tetraspanin microdomains at the plasma membrane. Virology. 346: 194–204.

124. Ako-Adjei, D., M.C. Johnson, and V.M. Vogt. 2005. The retroviral capsid domain dictates virion size, morphology, and coassembly of gag into virus-like particles. J. Virol. 79: 13463–13472.

125. Sudhahar, C.G., R.M. Haney, Y. Xue, and R.V. Stahelin. 2008. Cellular membranes and lipid-binding domains as attractive targets for drug development. Curr. Drug Targets. 9: 603–613.

126. McMahon, H.T., and J.L. Gallop. 2005. Membrane curvature and mechanisms of dynamic cell membrane remodelling. Nature. 438: 590–596.

127. Zimmerberg, J., and M.M. Kozlov. 2006. How proteins produce cellular membrane curvature. Nat. Rev. Mol. Cell Biol. 7: 9–19.

128. Lemmon, M.A. 2008. Membrane recognition by phospholipid-binding domains. Nat. Rev. Mol. Cell Biol. 9: 99–111.

129. Graham, T.R., and M.M. Kozlov. 2010. Interplay of proteins and lipids in generating membrane curvature. Curr. Opin. Cell Biol. 22: 430–436.

130. Wuttke, A., J. Sågetorp, and A. Tengholm. 2010. Distinct plasma-membrane PtdIns(4)P and PtdIns(4,5)P2 dynamics in secretagogue-stimulated beta-cells. J. Cell Sci. 123: 1492–1502.

131. Wu, B., Y. Chen, and J.D. Müller. 2009. Fluorescence fluctuation spectroscopy of mCherry in living cells. Biophys. J. 96: 2391–2404.

132. Lemmon, M.A., K.M. Ferguson, R. O'Brien, P.B. Sigler, and J. Schlessinger. 1995. Specific and high-affinity binding of inositol phosphates to an isolated pleckstrin homology domain. Proc. Natl. Acad. Sci. U. S. A. 92: 10472–10476.

133. Morgan, A.J., and R. Jacob. 1994. Ionomycin enhances Ca2+ influx by stimulating store-regulated cation entry and not by a direct action at the plasma membrane. Biochem. J. 300: 665–672.

134. Rhee, S.G., and Y.S. Bae. 1997. Regulation of Phosphoinositide-specific Phospholipase C Isozymes. J. Biol. Chem. 272: 15045–15048.

135. Várnai, P., and T. Balla. 2006. Live cell imaging of phosphoinositide dynamics with fluorescent protein domains. Biochim. Biophys. Acta. 1761: 957–967.

136. Brent, R. 2009. Cell signaling: what is the signal and what information does it carry? FEBS Lett. 583: 4019–4024.

137. Dolmetsch, R.E., and R.S. Lewis. 1994. Signaling between intracellular Ca2+ stores and depletion-activated Ca2+ channels generates [Ca2+]i oscillations in T lymphocytes. J. Gen. Physiol. 103: 365–388.

138. Tombes, R.M., C. Simerly, G.G. Borisy, and G. Schatten. 1992. Meiosis, egg activation, and nuclear envelope breakdown are differentially reliant on Ca2+, whereas germinal vesicle breakdown is Ca2+ independent in the mouse oocyte. J. Cell Biol. 117: 799–811.

139. Raucher, D., T. Stauffer, W. Chen, K. Shen, S. Guo, J.D. York, M.P. Sheetz, and T. Meyer. 2000. Phosphatidylinositol 4,5-bisphosphate functions as a second messenger that regulates cytoskeleton-plasma membrane adhesion. Cell. 100: 221–228.

140. Temmerman, K., and W. Nickel. 2009. A novel flow cytometric assay to quantify interactions between proteins and membrane lipids. J. Lipid Res. 50: 1245–1254.

141. Pelham, R.J., and Y. l Wang. 1997. Cell locomotion and focal adhesions are regulated by substrate flexibility. Proc. Natl. Acad. Sci. U. S. A. 94: 13661–13665.

142. Wang, H.B., M. Dembo, S.K. Hanks, and Y. Wang. 2001. Focal adhesion kinase is involved in mechanosensing during fibroblast migration. Proc. Natl. Acad. Sci. U. S. A. 98: 11295–11300.

143. Tzur, A., R. Kafri, V.S. LeBleu, G. Lahav, and M.W. Kirschner. 2009. Cell growth and size homeostasis in proliferating animal cells. Science. 325: 167–171.

144. Watt, S.A., G. Kular, I.N. Fleming, C.P. Downes, and J.M. Lucocq. 2002. Subcellular localization of phosphatidylinositol 4,5-bisphosphate using the pleckstrin homology domain of phospholipase C delta1. Biochem. J. 363: 657–666.

145. Hammond, G.R.V., S.K. Dove, A. Nicol, J.A. Pinxteren, D. Zicha, and G. Schiavo. 2006. Elimination of plasma membrane phosphatidylinositol (4,5)-bisphosphate is required for exocytosis from mast cells. J. Cell Sci. 119: 2084–2094.

146. Honda, A., M. Nogami, T. Yokozeki, M. Yamazaki, H. Nakamura, H. Watanabe, K. Kawamoto, K. Nakayama, A.J. Morris, M.A. Frohman, and Y. Kanaho. 1999. Phosphatidylinositol 4-phosphate 5-kinase alpha is a downstream effector of the small G protein ARF6 in membrane ruffle formation. Cell. 99: 521–532.

147. McLaughlin, S., J. Wang, A. Gambhir, and D. Murray. 2002. PIP(2) and proteins: interactions, organization, and information flow. Annu. Rev. Biophys. Biomol. Struct. 31: 151–175.

148. McLaughlin, S., and D. Murray. 2005. Plasma membrane phosphoinositide organization by protein electrostatics. Nature. 438: 605–611.

149. Araki, N., Y. Egami, Y. Watanabe, and T. Hatae. 2007. Phosphoinositide metabolism during membrane ruffling and macropinosome formation in EGF-stimulated A431 cells. Exp. Cell Res. 313: 1496–1507.

150. Johnson, S.A., B.M. Stinson, M.S. Go, L.M. Carmona, J.I. Reminick, X. Fang, and T. Baumgart. 2010. Temperature-dependent phase behavior and protein partitioning in giant plasma membrane vesicles. Biochim. Biophys. Acta. 1798: 1427–1435.

151. Sezgin, E., H.-J. Kaiser, T. Baumgart, P. Schwille, K. Simons, and I. Levental. 2012. Elucidating membrane structure and protein behavior using giant plasma membrane vesicles. Nat. Protoc. 7: 1042–1051.

152. Shi, J., C.W. Heegaard, J.T. Rasmussen, and G.E. Gilbert. 2004. Lactadherin binds selectively to membranes containing phosphatidyl-L-serine and increased curvature. Biochim. Biophys. Acta. 1667: 82–90.

153. Yeung, T., G.E. Gilbert, J. Shi, J. Silvius, A. Kapus, and S. Grinstein. 2008. Membrane phosphatidylserine regulates surface charge and protein localization. Science. 319: 210–213.

154. Laux, T., K. Fukami, M. Thelen, T. Golub, D. Frey, and P. Caroni. 2000. GAP43, MARCKS, and CAP23 modulate PI(4,5)P(2) at plasmalemmal rafts, and regulate cell cortex actin dynamics through a common mechanism. J. Cell Biol. 149: 1455–1472.

155. Caroni, P. 2001. New EMBO members' review: actin cytoskeleton regulation through modulation of PI(4,5)P(2) rafts. EMBO J. 20: 4332–4336.

156. Rayne, F., A.V. Kajava, J. Lalanne, and R.Z. Mamoun. 2004. In vivo homodimerisation of HTLV-1 Gag and MA gives clues to the retroviral capsid and TM envelope protein arrangement. J. Mol. Biol. 343: 903–916.

157. Shivakumar, S., M. Kurylowicz, N. Hirmiz, Y. Manan, O. Friaa, A. Shamas-Din, P. Masoudian, B. Leber, D.W. Andrews, and C. Fradin. 2014. The proapoptotic protein tBid forms both superficially bound and membrane-inserted oligomers. Biophys. J. 106: 2085–2095.

158. Hirose, K., S. Kadowaki, M. Tanabe, H. Takeshima, and M. Iino. 1999. Spatiotemporal dynamics of inositol 1,4,5-trisphosphate that underlies complex Ca2+ mobilization patterns. Science. 284: 1527–1530.

159. Novakovic, V.A., D.B. Cullinan, H. Wakabayashi, P.J. Fay, J.D. Baleja, and G.E. Gilbert. 2011. Membrane-binding properties of the Factor VIII C2 domain. Biochem. J. 435: 187–196.

160. Kay, J.G., M. Koivusalo, X. Ma, T. Wohland, and S. Grinstein. 2012. Phosphatidylserine dynamics in cellular membranes. Mol. Biol. Cell. 23: 2198–2212.

161. Doberstein, S.K., and T.D. Pollard. 1992. Localization and specificity of the phospholipid and actin binding sites on the tail of Acanthamoeba myosin IC. J. Cell Biol. 117: 1241–1249.

162. Reizes, O., B. Barylko, C. Li, T.C. Südhof, and J.P. Albanesi. 1994. Domain structure of a mammalian myosin I beta. Proc. Natl. Acad. Sci. U. S. A. 91: 6349–6353.

163. Hokanson, D.E., and E.M. Ostap. 2006. Myo1c binds tightly and specifically to phosphatidylinositol 4,5-bisphosphate and inositol 1,4,5-trisphosphate. Proc. Natl. Acad. Sci. U. S. A. 103: 3118–3123.

164. Hokanson, D.E., J.M. Laakso, T. Lin, D. Sept, and E.M. Ostap. 2006. Myo1c binds phosphoinositides through a putative pleckstrin homology domain. Mol. Biol. Cell. 17: 4856–4865.

165. Hamard-Peron, E., and D. Muriaux. 2011. Retroviral matrix and lipids, the intimate interaction. Retrovirology. 8: 15.

166. Inlora, J., V. Chukkapalli, D. Derse, and A. Ono. 2011. Gag localization and virus-like particle release mediated by the matrix domain of human T-lymphotropic virus type 1 Gag are less dependent on phosphatidylinositol-(4,5)-bisphosphate than those mediated by the matrix domain of HIV-1 Gag. J. Virol. 85: 3802–3810.

167. Le Blanc, I., A.R. Rosenberg, and M.C. Dokhélar. 1999. Multiple functions for the basic amino acids of the human T-cell leukemia virus type 1 matrix protein in viral transmission. J. Virol. 73: 1860–1867.

Appendix A:
HRas-EGFP and HRas-EGFP$_2$ at the membrane

In this thesis, we applied z-scan FFS to characterize the brightness of both the membrane-bound and cytoplasmic populations of HRas-EGFP. Our data showed HRas-EGFP to be monomeric at both the upper and lower plasma membrane and also in the cytoplasm of U2OS cells, thus making HRas-EGFP an ideal monomeric calibration protein.

To study higher-order oligomeric proteins at the plasma membrane, it is advantageous to have a membrane-bound dimer calibration protein. We cloned such a tandem dimeric protein by adding a second EGFP sequence to our HRas-EGFP plasmid and performed z-scan FFS to measure its brightness at the membrane and cytoplasm. Further we constructed a monomer-to-dimer plot which shows that the membrane brightness of HRas-EGFP$_2$ is twice that of HRas-EGFP (Figure A1).

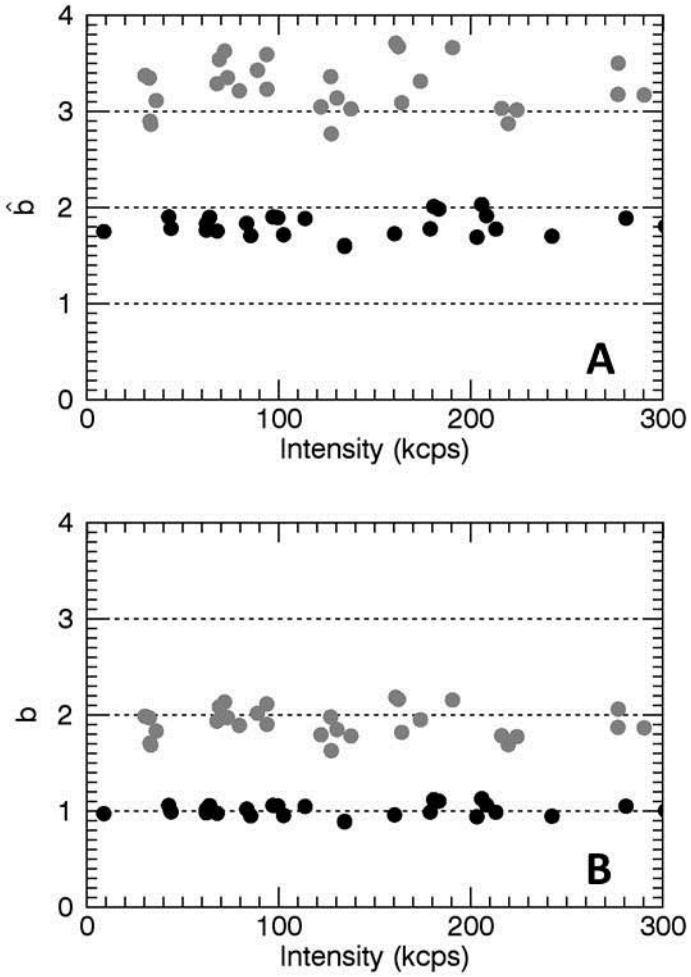

Figure A.1 Membrane brightness calibration standard

Normalized raw brightness of HRas-EGFP (*solid circles*) and of HRas-$EGFP_2$ (*shaded circles*) (A) Raw measured brightness at the membrane (B) True underlying membrane layer brightness.

Appendix B:

Binding Curve for PH-PLCδ-EGFP at Low Intensities

The presence of miniGAP-mCh led to a decrease in the binding curve for PH-PLCδ-EGFP. We plot the same data with a reduced scale so the behavior at low intensities can be more clearly visualized. The marked decrease in the amplitude of the binding curve seen in Figure B.1 implies that miniGAP and PH-PLCδ compete for the same binding sites at the membrane.

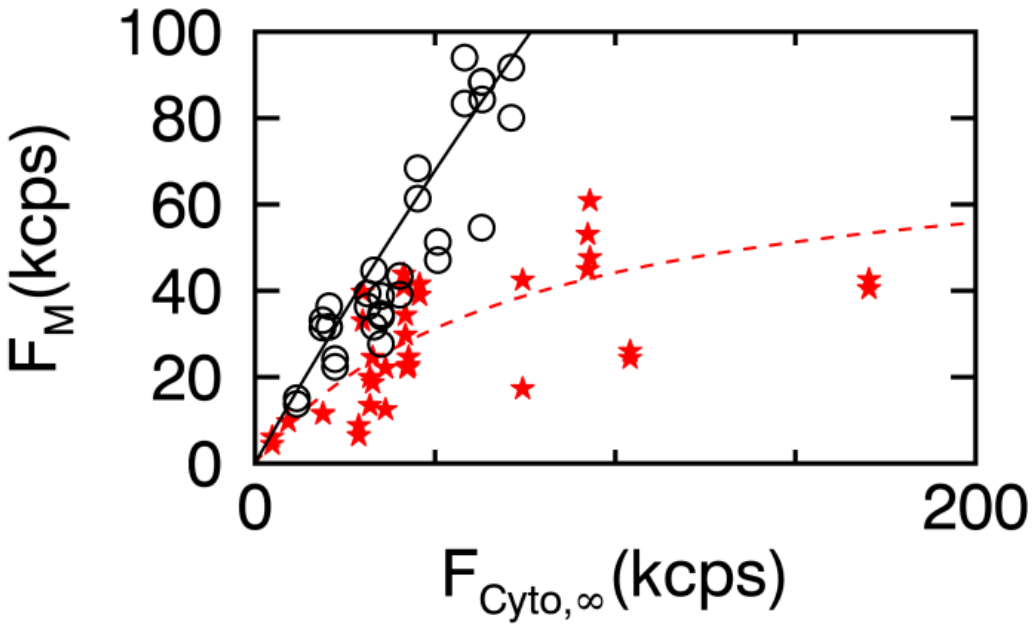

Figure B.1 Close-up view of the low cytoplasmic intensity region of Figure 5.4A.

Binding curve for PH-PCLδ-EGFP (*open circles*) and fit (*solid line*) are shown together with the competitive binding curve for PH-PCLδ-EGFP coexpressed with miniGAP-mCh (*solid stars*) and fit (*dotted line*).

Appendix C: miniGAP-EGFP Membrane Binding Curve

Gap43 is a peripheral membrane protein shown to interact with PI(4,5)P_2 lipids as a result of palmitolyation at Cys-3 and Cys-4 (154, 155). MiniGAP-EGFP is a truncated membrane binding version of Gap43 (the first 10 amino acids) with an EGFP label. We measured U2OS cells transiently transfected with miniGap-EGFP and determined the experimental membrane-binding curve (Figure C.1, *open triangles*). A fit (*shaded line*) to the Langmuir-isotherm binding model identified a saturation concentration $\sigma_0 = 6710 \pm 980\,\mu\text{m}^{-2}$ and a dissociation coefficient $K = 1280 \pm 320$ nM. The saturation concentration matches with the saturation concentration observed for EGFP-PLCδ-PH (6200±1300 molecules/μm^2), another PI(4,5)P_2 binding protein.

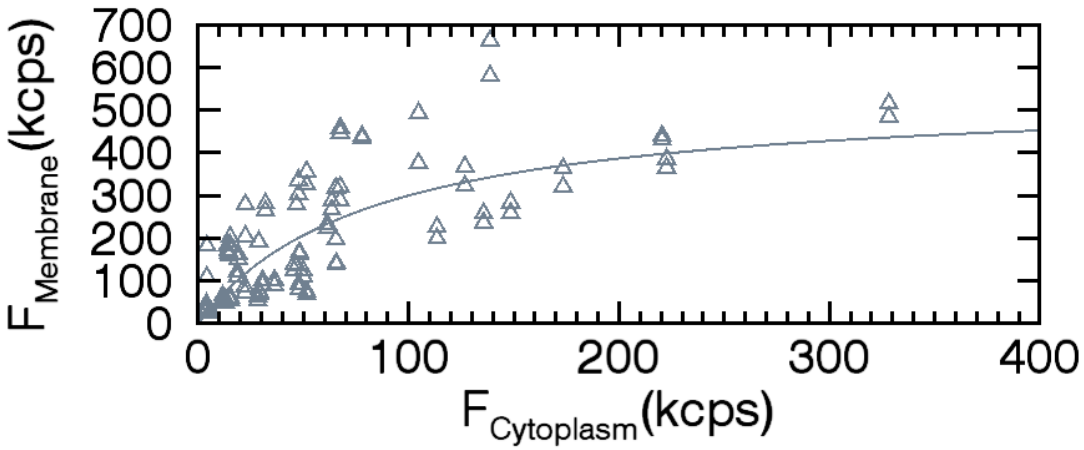

Figure C.1 miniGAP-EGFP membrane binding curve

Fluorescence membrane binding curve of miniGAP-EGFP in U2OS cells (*open triangles*). The fit (*shaded line*) to Eq. 6.6 recovers $F_0 = 550 \pm 80$ kcps and $F_k = 80 \pm 20$ kcps.

Appendix D: Oligomeric State of Myo1C-EGFP

We used Myo1C, a member of the myosin I superfamily, as a model system for fitting membrane-binding curves in chapter 6. We also performed z-scan FFS to determine the oligomeric state of Myo1C at the plasma membrane. The z-scan analysis determined that Myo1C-EGFP was monomeric at the plasma membrane over the concentration range studied (Figure D.1).

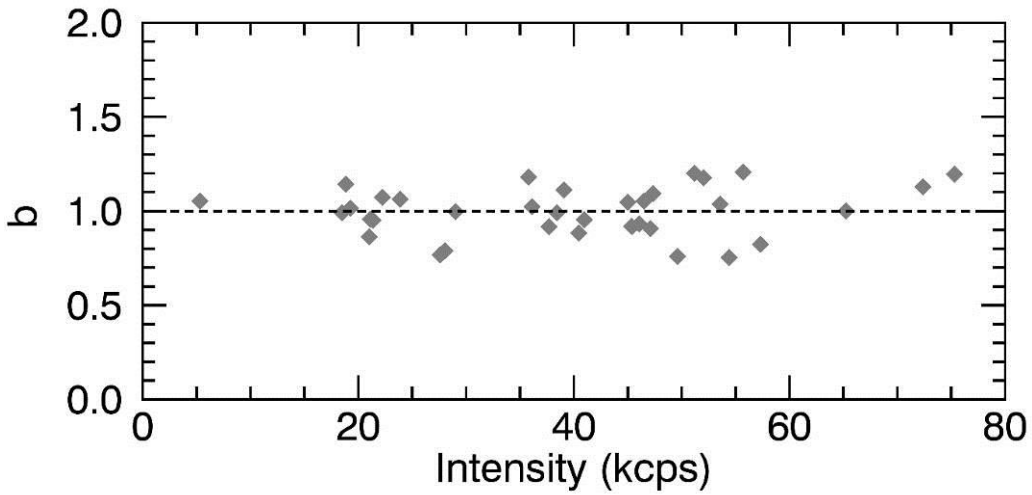

Figure D.1 Normalized membrane layer brightness of Myo1C-EGFP

Appendix E: Lipid Specificity of Myo1C-EGFP

Myo1C is known to associate with plasma membrane lipids ($PI(4,5)P_2$ and PS) through electrostatic interactions involving the tail domain (161, 162). Studies have confirmed the binding of Myo1C to $PI(4,5)P_2$ and PS lipids in an *in-vitro* model membrane environment (163, 164). We decided to apply our dual-color z-scan FPD competition technique to study the lipid-specific binding of Myo1C within a live cell environment. We first coexpressed Myo1C-EGFP with miniGAP-mCh to probe the binding to $PI(4,5)P_2$. In Figure E.1 A, the presence of miniGAP-mCh led to a decrease in the Myo1C-EGFP binding curve (*solid diamonds*) as compared to the binding data (*open triangles*) taken for Myo1C-EGFP alone. This observation suggests that $PI(4,5)P_2$ is a potential lipid target for Myo1C-EGFP. We next coexpressed Myo1C-EGFP with Lact-C2-mCh to probe PS binding. The presence of Lact-C2-mCh led to a decrease in the binding curve of Myo1C-EGFP (Figure E.2 B, *solid squares*) as compared to Myo1C-EGFP alone (*open triangles*). This result indicates that PS lipids are also an important binding target of Myo1C-EGFP.

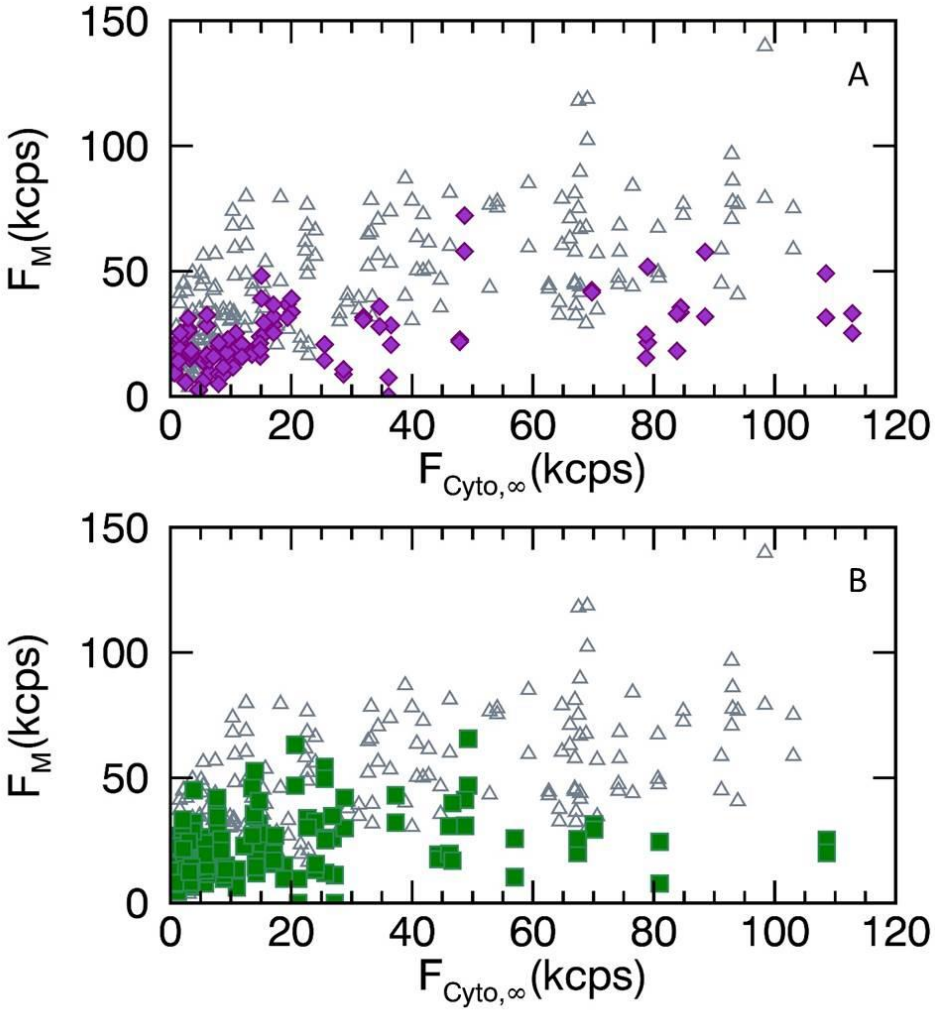

Figure E.1 Membrane binding and lipid specificity of Myo1C-EGFP

Fluorescence membrane binding for Myo1C-EGFP (*open triangles*) in U2OS cells. (*A*) The competitive binding for Myo1C-EGFP coexpressed with miniGAP-mCh (*solid diamonds*) shows a decrease as compared to Myo1C-EGFP alone. (*B*) The competitive binding for Myo1C-EGFP coexpressed with LactC2-mCh (*solid squares*) shows a decrease as compared to Myo1C-EGFP alone.

Appendix F. SS-EGFP and SS-EGFP$_2$ in the Nuclear Envelope

The development of z-scan FFS broadened the capability of brightness analysis to include proteins distributed across stratified layers, such as the cytoplasm and the plasma membrane. In this work we collaborated with Dr. G.W. Gant Luxton and his graduate student Cosmo Sanders to further extend z-scan FFS to study proteins that reside on or within the nuclear envelope.

We test the feasibility of this extension to internal membranes with a new EGFP calibration complex. Our collaborators in Genetics Cell Biology and Development placed a 20 amino acid ER signal sequence (SS) in front of EGFP. We denote this complex as SS-GFP. The complex is translated into the lumen of the endoplasmic reticulum (ER) with the signal sequence cleaved, resulting in an EGFP protein free to diffuse within the ER and nuclear envelope. The brightness of SS-EGFP is determined by performing z-scan FFS measurements where corrections are applied for both the thin layer geometry and coexcitation of adjacent layers. Additionally, our collaborators cloned and we tested a tandem dimeric EGFP protein (SS-EGPF$_2$) to establish a model for calibrating brightness and stoichiometry.

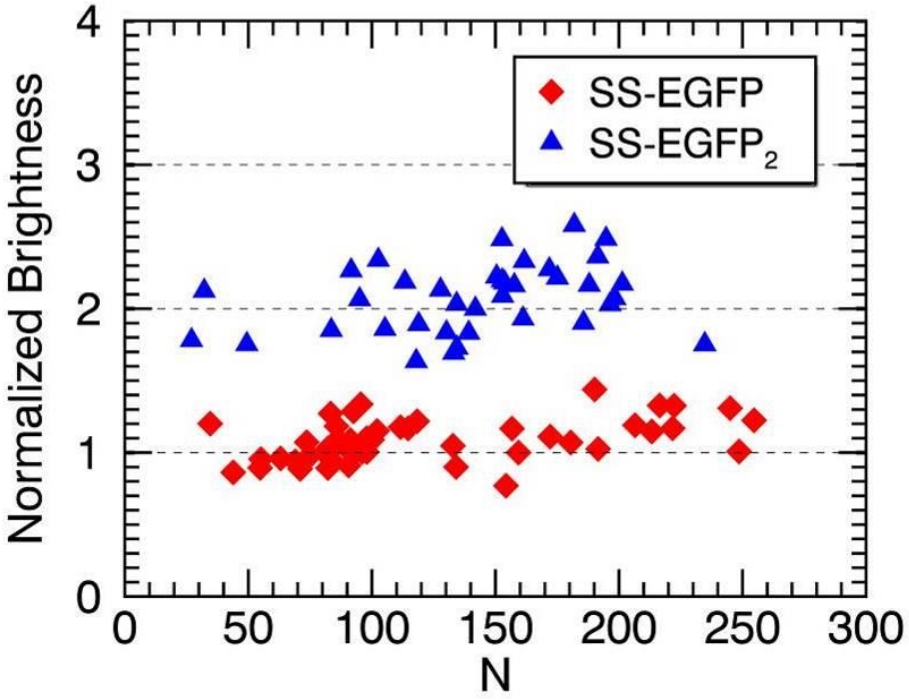

Figure F.1 Z-scan brightness analysis of SS-EGFP and SS-EGFP$_2$.

SS-EGFP brightness b (*solid diamonds)* and SS-EGFP$_2$ b *(solid triangles)* in the nuclear envelope.

Appendix G. torsinA-EGFP and torsinAΔNTD- EGFP in the Nuclear Envelope

We furthered our collaborative research efforts with the Luxton Lab and studied the oligomerization of torsin-1A (torsinA, TA) within the nuclear envelope. TA is a protein of interest because a glutamic acid deletion (ΔE) from TA causes the neurological movement disorder DYT1 dystonia, a specific type of dystonia that is frequently found in children. TorsinA is a membrane-associated AAA+ ATPase that resides within the nuclear envelope (NE) where it is required for proper NE structure and nuclear-cytoskeletal coupling through an undefined molecular mechanism. As a starting point of our investigation into the behavior of TA we used z-scan FFS to probe its oligomeric state within the NE of living cells.

Through z-scan FFS brightness measurements we determined that TA oligomerizes to form dimeric to trimeric assembly states within the NE. We further tested the oligomerization of a TA mutant that does not associate with the membrane (TA-ΔNTD). This TA mutant forms higher order oligomers on average, which suggests that TA's ability to associate with membranes negatively regulates homo-oligomerization.

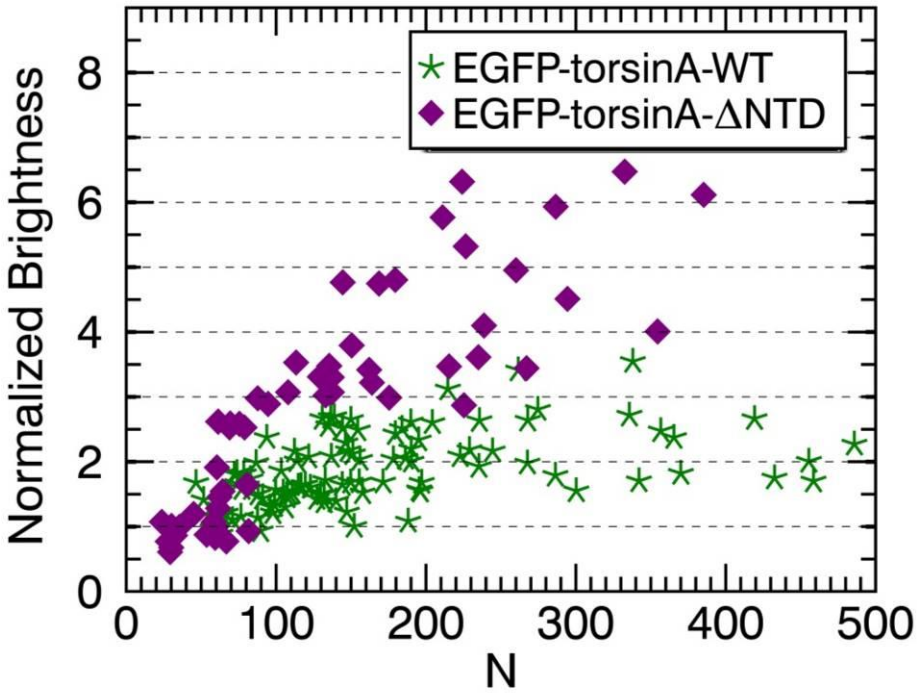

Figure G.1 Z-scan brightness analysis of EGFP-TA-WT and EGFP-TA-ΔNTD.

EGFP-TA-WT brightness b (*asterisks)* and EGFP-TA-ΔNTD b *(solid diamonds)* in the nuclear envelope.